Two-dimensional colloidal systems: grain boundaries and confinement

Thomas O. E. Skinner

Lincoln College
University of Oxford

Supervisor: Dr Roel P. A. Dullens

A thesis submitted for the degree of
Doctor of Philosophy

Hilary Term 2012

Abstract

The behaviour of colloidal particles in two-dimensional (2D) systems is addressed in real space and time using magnetic fields, optical tweezers and optical video microscopy. First, the fluctuations of a grain boundary in a 2D colloidal crystal are analysed. A real space analogue of the capillary fluctuation method is derived and successfully employed to extract the key parameters that characterise the grain boundary. Good agreement is also found with a fluctuation-dissipation based method recently suggested in simulation. Following on from analysis of the interface fluctuations, the properties of the individual grain boundary particles are analysed to investigate the long standing hypothesis that suggests that grain boundary particle dynamics are similar to those in supercooled liquids. The grain boundary particle dynamics display cage breaking at long times, highly heterogeneous particle dynamics and the formation of co-operatively moving regions along the interface, all typical behaviour of a supercooled liquid. Next, the frustration induced by confining colloidal particles inside a pentagonal environment is investigated. The state of the system is adjusted via two separate control parameters: the inter-particle interaction potential and the number density. A gradual crystalline to confined liquid-like transition is observed as the repulsive inter-particle interaction potential is decreased. In contrast, re-entrant orientational ordering and dynamical effects result as the number density of the confined colloidal particles is increased. Finally, the dynamics of colloidal particles distributed amongst a random array of fixed obstacle particles is probed as a function of both the mobile particle and fixed obstacle particle number densities. Increasing the mobile and the obstacle particle number density drives the system towards a glass transition. The dynamics of the free particles are shown to behave in a similar way to the normal glass transition at low obstacle density and more analogous to a localisation glass transition at high obstacle density.

Declaration

This thesis is submitted for the degree of Doctor of Philosophy in Physical and Theoretical Chemistry at the University of Oxford. No part of this thesis has been accepted or is currently being submitted for any degree, diploma, certificate or other qualification in this University or elsewhere. This thesis is wholly my own work, except where indicated.

Contents

Chapter 1

General Introduction

The colloidal size domain, often described as 'mesoscopic', bridges the vast gap in length-scales between the atomic and macroscopic worlds [1]. There was however, little interest or knowledge of existing colloidal systems until they became important in industry, and then biology, in the first half of the 20^{th} century. Since then, understanding and interest in colloidal systems has risen sharply, explaining many existing phenomena, and leading to the development of new products and technologies [1, 2].

The term 'colloidal' derives from the Greek for 'glue-like', coined by Thomas Graham in 1861 [3] when describing the so-called 'pseudosolutions'. As these could be filtered he deduced they must be suspensions of particles in a liquid. From their low rate of diffusion, he inferred that the particles were at least 1 nm in size and from their lack of sedimentation, at most 1 μm. In keeping with Graham's observations, today, colloidal systems are broadly defined as those containing one phase, with a length-scale on the order of nanometers to microns, dispersed in a continuous phase [2]. It is this characteristic length-scale that defines the colloidal domain, which is therefore not material specific. For instance, emulsions, gels, aerosols and sols are all examples of colloidal systems. The colloidal systems used in this work are all micron-sized polymer spheres dispersed in water and as such the dispersed phase is referred to simply as the 'colloidal particles' or just simply 'particles'.

Due to the great size range they encompass it is of little surprise that colloid science is so ubiquitous. From the naturally occurring of fog and milk, to the man-made of ice cream [4] and

paint [5], colloidal systems exist in many, seemingly unrelated, disciplines and environments. These range from lubricants and aerosols [6], to new technologies such as magneto-rheological fluids which are coming to market in the guise of improved brake design [7]. In addition, due to the ability of colloidal particles to self assemble, research is being lead into possible photonic applications [8]. All these examples, widespread in many industries, demonstrate why colloidal systems are important for study, for academic understanding and technological development.

1.1 Colloids as model systems

One property that sets colloidal particles apart from the other size regimes is that on these length scales Brownian motion is non-negligible and therefore plays a key role in colloidal particle dynamics. Brownian motion describes the random movements of colloidal particles in a medium due to the continual collisions with the solvent and was first observed by Robert Brown in plant pollen dispersed in water. A theoretical explanation was then provided by Einstein in conjunction with the experiments conducted by Jean Baptiste Perrin [9, 10]. Although a simple concept, it is the presence of Brownian motion that makes colloid science so rich. Due to Brownian motion, colloidal particles have an equilibrium behaviour that is thermodynamically equivalent to atomic systems, even though the dynamics of atoms and colloidal particles differ, showing ballistic and diffusive short time motion respectively. Increasing the concentration of colloidal particles scans through the phase diagram giving rise to rich phenomenology, including the formation of colloidal 'crystals', 'fluids' and 'gases', similar to phases observed in atomic systems. Brownian motion occurs on the time-scales of seconds and as the length-scales of colloidal systems are on the order of microns, the colloidal particles are easily followed in real time with optical microscopy [2, 11]. Hence, colloidal systems are excellent for use as model atomic systems, with both colloidal particles and atoms having well defined and analogous thermodynamic states. The existence of Brownian motion indicates that hydrodynamics can also play a crucial role in the behaviour of colloidal particles, particularly when in shear and in close proximity to walls [12, 13]. However, these effects are expected to be less prominent in the 2D systems studied here where particle movement is only Brownian in origin.

The ability of colloidal systems to act as model systems is also due to the highly tunable nature of their interactions [14, 15]. For instance, the inter-particle interactions can be tuned with addition of salts or polymers, or by modifying the surface chemistry to form interactions ranging from hard sphere like [16], to attractive [17] and to highly repulsive [18]. Magnetic nanoparticles can be incorporated into the colloidal particles to give them super-paramagnetic properties, which allows for manipulation via external magnetic fields [19, 20]. In addition, the shape of colloidal particles can be altered to, for example, rod-like, which leads to anisotropic systems including the formation of liquid crystals [21].

Colloidal systems belong to a class of materials known as 'Soft Matter', which also includes materials like polymers and micro-emulsions. The term 'soft' is used to emphasise the low Young's modulus of these systems compared to atomic systems [1]. The Young's modulus scales as an energy per unit volume, a colloidal crystal typically has an energy associated with it of k_BT, whereas in an atomic crystal the energy is on the order of 1 eV. Hence, given the vastly different length-scales present, microns and angstroms for colloidal and atomic systems respectively, the Young's modulus of colloidal systems is about a factor of 10^{12} lower than in atomic crystals. Colloidal systems therefore can shear and distort much more easily than their atomic counterparts. The softness of colloidal systems can be exploited using optical tweezers [22], a highly focused laser beam used to trap and manipulate particles, enabling great control over for instance, colloidal nucleation and coalescence [23].

1.2 Low dimensional systems

So far the behaviour described all refers to three-dimensional (3D) systems. In this thesis however, all studies are conducted in two-dimensional (2D) colloidal systems, which can contain quite different characteristics. Two-dimensional systems are common and have widespread applications and relevance including in 2D superconductors [24], thin films for corrosion resistance [25] and thin photovoltaic cells [26]. The behaviour of 2D and 3D systems contrasts in their particle packing behaviour. The most efficient way to pack spheres locally in 3D is in a tetrahedron, however as regular tetrahedra do not fill space, the most efficient packing of spheres in bulk is hexagonally close packed [27]. In contrast, in 2D there is no distinction between the most

efficient local and long range packing behaviour, spheres in a 2D plane pack most efficiently hexagonally.

The melting transition is a very notable example of how behaviour is greatly influenced by dimensionality [28]. In contrast to 3D crystals which melt via a first order phase transition, in 2D, crystals melt via a two step scenario with an intermediate hexatic phase, characterised by quasi-long range orientational and short range translational order [18]. Interfaces can also be considered to be a form of a low dimensional system, for instance the particles constituting a grain boundary, which is the interface between two crystallites. For a 1D interface in a 2D crystal the interfacial tension scales as the inverse of the particle diameter, therefore colloidal systems have a far lower interfacial tension than atomic and molecular systems [14]. Consequently, the interface fluctuations in colloidal systems due to thermal energy are more significant and more easily observed [29].

1.3 Scope of this thesis

In this thesis the behaviour of 2D colloidal systems is investigated using optical video microscopy, optical tweezing and external magnetic fields. These tools enable the study of grain boundaries and other forms of confinement in 2D colloidal systems.

The chapters are organised as follows. Firstly, in chapter 2, the colloidal model systems and the experimental techniques and background are introduced. This includes the various properties of the colloidal particles used and the set-up and design of the optical tweezer and optical microscope. The Helmholtz coils for generating magnetic fields and sample cell design and manufacture are described before the image capture and image processing are introduced.

Grain boundary fluctuations in 2D colloidal crystals are described in chapter 3. Grain boundaries define material strength, but as experimentally studying atomic grain boundaries is difficult, previous studies on grain boundary fluctuations have focused on simulations. In this experimental work, the grain boundary study utilises and builds upon the analytical techniques used in molecular dynamics computer simulations [30], not only to probe the behaviour of colloidal grain boundaries directly, but to act as an experimental test for interface fluctuation

theories. The fluctuations of a grain boundary in a 2D colloidal crystal were analysed and the grain boundary properties determined via several complimentary methods derived from capillary wave theory.

In chapter 4, the dynamics of the colloidal particles constituting a grain boundary in a 2D colloidal crystal are analysed. It has long been hypothesised that the dynamics of grain boundary particles may show dynamics similar to supercooled liquids [31]. This hypothesis was corroborated recently by molecular dynamics simulations [32]. The aim of this chapter is to test this long standing hypothesis in experiment. The dynamics of the grain boundary particles are shown to be highly heterogeneous, with non-Gaussian distributions and to contain co-operatively rearranging regions, all behaviour characteristic of supercooled systems.

The most efficient packing of spherical particles in 2D is hexagonally. In chapter 5, the packing of spherical particles into pentagonal confinement is investigated. Using an optical tweezer, colloidal particles are fixed into position creating a pentagon, within which further particles are confined. The state of the system depends on both the interaction potential and the number density. Firstly, the effect of lowering the inter-particle interactions via an external magnetic field is assessed. Secondly, the packing frustration and the consequences for the orientational and dynamical behaviour are analysed when the number of confined colloidal particles is sequentially increased. Partially melting from a crystal-like to a confined liquid-like state was observed when the particle interaction potential was deceased. In contrast, re-entrant orientational particle ordering and fluctuating levels of particle movement were observed as the number density of the confined particles was increased.

In chapter 6 the question of how the dynamics of fluids are affected in random confinement is addressed. Transport of fluids in random porous media has important consequences for fields as diverse as filtration and catalysis [33]. A 2D system is created where small colloidal particles (the fluid) are free to move within a randomly distributed array of large particles fixed in position (the matrix). The effective area fraction of the fluid and the matrix particles are controlled via the inter-particle interaction potential and the number density. State points along lines across a state diagram of the effective area fraction of the fluid to that of the matrix

are analysed. Predictions emanating from theory [34] and simulation [35], including from the Lorentz model [36], are tested in this experimental system at the corresponding regions of the state diagram. Upon increasing the effective area fraction the dynamics of the fluid particles are shown to follow a standard glass transition at low matrix density, and a more localisation dominated glass transition at high matrix density, consistent with both theory and simulation.

Chapter 2

Background and experimental methods

ABSTRACT

In this thesis colloidal particles are used as a model system for studying a range of condensed matter phenomena ranging from the dynamics of fluids in confinement to grain boundary fluctuations. As such, colloidal particles and their interactions are relevant to each chapter and will be introduced here along with the general experimental techniques. The main experimental set-up is an inverted transmission optical microscope coupled with an infrared optical tweezer and an array of electromagnets. The theory behind optical tweezing will be briefly described before the experimental set-up is explained. Lastly, the manufacture and use of sample cells, image capture and processing, and the particle tracking procedures are introduced.

2.1 Colloidal particles

2.1.1 Hard spheres

Colloidal particles, as introduced in chapter 1, are micron-sized particles dispersed in a solvent, e.g. water. The simplest form of colloidal interaction is a hard sphere interaction. The particles have zero interaction at centre to centre distances greater than the particle diameter and an infinitely repulsive interaction potential otherwise. This hard potential results in all phase changes being purely entropic. Understanding the entropy driven world colloidal hard spheres inhabit is vital to understanding many phenomena in soft matter. As only excluded volume interactions exist, the hard sphere phase diagram depends solely upon the particle volume fraction. The hard sphere volume fraction is represented by $\phi = \rho v$, where ρ is the number density and v the particle volume.

The existence of a fluid-solid phase transition in a purely repulsive system was suggested as long ago as 1914 by Bridgman [37]. However, it was not until 1957 that conclusive evidence for a phase transition was given. Computer simulations by Wood and Jacobson [38] and Alder and Wright [39] demonstrated that at sufficiently high densities hard spheres systems can crystallise. This disorder-order transition occurs at the point when the configurational entropy of the fluid state is outweighed by the free volume entropy of the ordered solid. Accurate mapping of the phase boundaries of the hard sphere phase diagram was then later achieved in 1968 by Hoover and Ree [40], with the freezing and melting transitions found to be $\phi_f = 49\%$ and $\phi_m = 54\%$ respectively. A representation of the hard sphere phase diagram, and in addition the non-equilibrium transition to the glassy state, is shown in figure 2.1. Hard sphere like colloidal particles were first realised in experiment in 1986 by Pusey and van Megen [16] and were shown to exhibit both crystallisation and a glass transition. Sterically stabilised polymethyl methacrylate (PMMA) particles were dispersed in a refractive index matching solvent, which minimised the van der Waals attractions, and resulted in nearly hard sphere interactions.

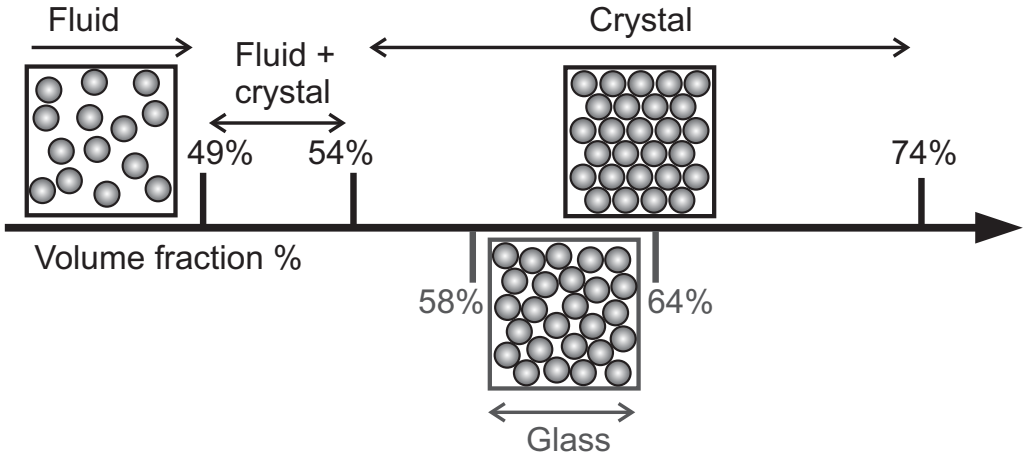

Figure 2.1: Hard sphere phase diagram displaying the regions of fluid, crystal, coexistence and the non-equilibrium glassy state. Note that the illustrations are two dimensional (2D) representations, the phase transitions are for a three dimensional (3D) system.

2.1.2 Charged spheres

In water based colloidal systems, charges emanating from dissolved ions and surface groups play a vital role in determining inter-particle interactions. Colloidal particles always experience attractive van der Waals forces at short distances when dispersed in solvents. Therefore, without a stabilising repulsive interaction, the particles will aggregate, often irreversibly. Two solutions to this problem are charge stabilisation and steric stabilisation. The latter involves adding an adsorbing or grafting polymer to the particle surface. Inter-particle steric repulsion is created due to entropic effects when polymer chains of neighbouring particles interact. Charge stabilisation involves modifying the particle surface during synthesis to add dissociating surface groups. Typically particles are stabilised with carboxyl surface groups, which dissociate in polar solvents making the colloidal particles negatively charged. Competition between entropy and charge attraction creates an electric double layer system, where each negatively charged particle is surrounded by a cloud of positively charged counter ions, see figure 2.2a. The colloidal particles interact via a repulsive short-ranged screened Coulomb potential $U(r) \propto \frac{1}{r}e^{-\kappa r}$ where r is the inter-particle distance and κ^{-1} the Debye screening length, which is a measure for the range of the repulsive interaction. As the Debye length depends on the ionic strength, the range of the interaction can be tuned by adding extra counter ions to the solution. Salt ions present in the solution screen the electrostatic interactions between the charge clouds leading to a reduced

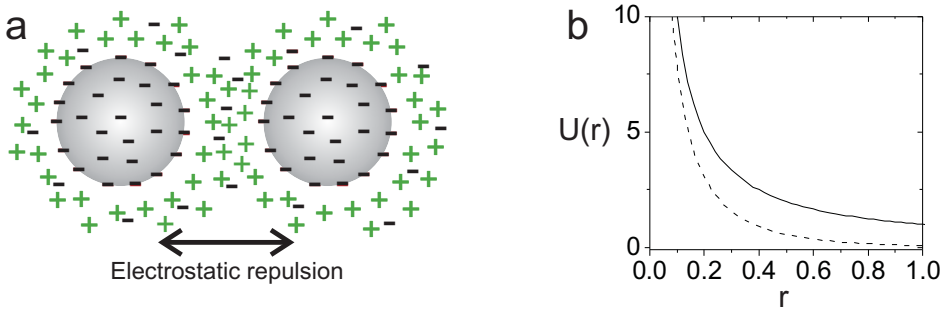

Figure 2.2: a) Illustration of the electric double layer formed when positive counter ions dissociate from surface groups, leaving the particle negatively charged. A repulsive force is felt when two colloidal particles charge clouds interact. Dispersed anions represent dissolved salt ions which screen the Coulombic repulsion. b) A Coulombic (solid line) and screened Coulombic (dashed line) repulsive potential as a function of the inter-particle distance r.

κ^{-1} and a steeply repulsive inter-particle potential. Examples of a Coulombic (solid line) and screened Coulombic (dashed line) repulsive potential are shown in figure 2.2.

2.1.3 Super-paramagnetic colloidal particles

Super-paramagnetic colloidal particles gain a magnetic dipole parallel to an applied magnetic field, but importantly they have zero magnetic dipole in its absence. This instant and reversible control over the particle magnetic dipoles enables great control over the inter-particle pair potential by manipulation of the external magnetic field. The colloidal particles contain iron oxide nanoparticles, typically γFe_2O_3 and Fe_3O_4, distributed within the polymer matrix of the colloidal particle [19]. In bulk, these iron oxides are ferrimagnetic and so have a constant magnetic dipole. However, when formed into nanoparticles, size ~ 5 nm, each nanoparticle subsequently contains only one magnetic domain [41]. These magnetic domains are sufficiently small that thermal energy can randomly cause their dipole direction to change. As such, in the absence of an external magnetic field, a colloidal particle containing a dispersion of these nanoparticles carries no net magnetic dipole. In contrast, in the presence of an external magnetic field, the magnetic domains align to give each colloidal particle a magnetic moment. Consequently, the colloidal particles are described as being super-paramagnetic: no net magnetic moment in the absence of an external field, no hysteresis and the ability to gain a magnetic moment parallel to an external magnetic field.

When in the presence of an external magnetic field, the super-paramagnetic colloidal particles can be approximated to point dipoles as the iron oxide nanoparticle density is fairly homogeneous (for a typical example see [19]). An external magnetic field, $\vec{B}$, induces in particle 1, a dipole moment $\vec{m}_1$ in the direction of $\vec{B}$. At low external magnetic fields the magnitude, m, of the induced magnetic moment, $\vec{m}_1$, is proportional to the applied field, $m = \chi B$, where χ is the magnetic susceptibility, a material specific property. The magnetic field induced, $\vec{B}_1(\vec{r})$, by the point dipole of particle 1 at the position of particle 2, a distance r away is [42]:

$$\vec{B_1}(\vec{r}) = \frac{\mu_0}{4\pi}\frac{1}{r^3}[3(\vec{m}_1 \cdot \hat{r})\hat{r} - \vec{m}_1] \tag{2.1}$$

where $\hat{r}$ is the unit vector between the two dipoles and μ_0 is the permeability of free space. The interaction energy, E, between two dipoles depends on the local magnetic field and the magnetic moment of the dipole [42]:

$$E = -\vec{m}_1\vec{B}_2 = -\vec{m}_2\vec{B}_1. \tag{2.2}$$

Substituting eq. (2.1) into eq. (2.2) gives the interaction energy between 2 dipoles in any orientation connected by vector $\vec{r}$ as:

$$E_{12}(\vec{r}) = \frac{\mu_0}{4\pi}\frac{1}{r^3}[\vec{m}_1 \cdot \vec{m}_2 - 3(\vec{m}_1 \cdot \hat{r})(\vec{m}_2 \cdot \hat{r})]. \tag{2.3}$$

The applied field is homogeneous in strength so all induced dipoles must have equal magnitude moments, m, parallel to the field. By expanding $\hat{r} = \frac{1}{r} \cdot \vec{r}$ the expression can be simplified to:

$$E_{12}(\vec{r}) = \frac{\mu_0}{4\pi}\frac{1}{r^5}[m^2r^2 - 3(\vec{m} \cdot \vec{r})^2]. \tag{2.4}$$

As all systems in this thesis are 2D, with the external magnetic field perpendicular to the plane, $\vec{m}$ and $\vec{r}$ are always orthogonal, and therefore:

$$E_{12}(r) = \frac{\mu_0}{4\pi}\frac{m^2}{r^3} = \frac{\mu_0}{4\pi}\frac{\chi^2B^2}{r^3}. \tag{2.5}$$

This expression then yields the repulsive interaction energy of two induced dipoles in a plane perpendicular to the external magnetic field.

2.1.4 Brownian motion

As alluded to in chapter 1, it is Brownian motion that is the key behind why colloidal systems are so rich in phenomenology and so useful as 'model atoms'. The constant bombardment of the colloidal particles by the solvent molecules gives the colloidal particles the thermal energy to explore phase space. Einstein, and separately Sutherland, described how Brownian motion can be related to a particle's diffusion coefficient, D [9, 43]. It should be noted that all the relations given here regarding Brownian motion relate to a system at infinite dilution. The diffusion coefficient, D, of a particle undergoing Brownian motion is given by:

$$D = \frac{k_B T}{\zeta} = \frac{k_B T}{6\pi\eta R} \tag{2.6}$$

where the latter is known as the Stokes-Einstein equation, the denominator is the Stokes relation, k_B the Boltzmann factor and T the temperature. The Stokes relation, $\zeta = 6\pi\eta R$, relates the friction factor, ζ, to the radius, R, of a spherical particle moving through a solvent of viscosity, η. To quantify the effect of Brownian motion on the colloidal particles and find an intrinsic timescale, the Brownian time is introduced and defined as the time taken for a particle to diffuse over its own diameter. The Brownian time in 2D, is derived from the mean square displacement, $\langle r^2(t)\rangle = 4Dt$. Setting the particle displacement, r, equal to the particle diameter gives the Brownian time as $\tau = \frac{R^2}{D}$. For a 1 μm particle this gives a Brownian time of ~ 1 s. The time and length-scales associated with colloidal particles allow standard optical video microscopy to be used to observe the colloidal particles in real time. Contrast this to the typical time and length-scales of atomic systems, where the atoms are ~ 0.1 nm and the 'Brownian times' ~ 1 ps, and the clear advantages of colloidal systems as a study medium for many phenomena, and as atomic models become apparent.

The basic colloidal system where polymer spheres dispersed in water are stabilised by screened Coulombic repulsions has been described. All experiments in this thesis are concerned with 2D systems where the particles are sedimented into a plane, therefore the particles must be more dense than the surrounding medium. The gravitational height, h_g, the height at which

a particle attains k_BT of gravitational energy, is given by:

$$h_g = \frac{3k_BT}{4\pi R^3 g\Delta\rho} \tag{2.7}$$

where R is the particle radius, $\Delta\rho$ the particle-solvent mass density difference and g the acceleration due to gravity. To create a 2D system and neglect gravitational effects, a gravitational height much smaller than the particle is required.

2.1.5 Experimental colloidal systems

Melamine formaldehyde colloidal particles

The melamine formaldehyde colloidal particles used in this work have a diameter of 2.7 μm and a high cross-linking density, making their structure extremely stable to temperature, acidity and solvent changes (microParticles). These colloidal particles are used in chapters 3 and 4 on colloidal grain boundaries. They are highly spherical and have good monodispersity with a coefficient of variation of $< 3\%$. The polymer spheres have a surface layer of carboxylic acid groups. This gives the particles a hydrophilic anionic surface charge when dispersed in water, leading to soft screened Coulombic repulsions and prevention of particle aggregation. The melamine particles have a mass density of 1.5 gcm^{-3} and refractive index of 1.68. This leads to good optical tweezing properties and a gravitational height of 0.08 μm, thus enabling the minimal, out of the plane thermal fluctuations to be neglected. The Brownian time of these particles at infinite dilution is 11 s, hence their dynamics are sufficiently slow that they can easily be studied in real time.

Super-paramagnetic colloidal particles

Within this work, three different sizes of super-paramagnetic colloidal particles are used. The 2.8 μm diameter Dynabeads M-270 colloidal particles are used in chapter 5. These are highly monodisperse cross-linked polystyrene spheres with a $< 3\%$ coefficient of variation. The carboxyl surface groups give the particles a slight negative charge preventing the need for stabilising surfactants. The particles contain γFe_2O_3 and Fe_3O_4 nanoparticles evenly dispersed in the polymer matrix. This homogeneous distribution allows the particles to be treated as point

dipoles when in the presence of an external magnetic field. The colloidal particles have a Brownian time of 13 s and a gravitational height of 0.07 μm.

In chapter 6, two sizes of particles are used, 3.9 μm (S2180) and 4.95 μm (S2490) in diameter (microParticles). These super-paramagnetic spheres are also cross-linked polystyrene particles containing a dispersion of iron oxide nanoparticles (γFe_2O_3 and Fe_3O_4), and are charge stabilised in water. The refractive index is 1.6 and the density ~ 1.7 gcm^{-3} and ~ 1.6 gcm^{-3} for the 3.9 μm and 4.95 μm diameter particles respectively. The gravitational heights for the small and large particles are both sufficiently small that gravitational effects can be neglected (0.02 μm and 0.01 μm respectively). The typical Brownian times for these particles are about 34 s (small) and 70 s (large) at infinite dilution.

As mentioned in section 2.1.3, at low external magnetic fields (up to ~ 20 mT) the induced magnetic moment, m, is directly proportional to the applied field B. The proportionality factor, χ, is the effective magnetic susceptibility where $m = \chi B$. The interaction energy between two super-paramagnetic particles, 1 and 2, positioned in a 2D plane, acting as induced dipoles in an orthogonally directed external magnetic field is given by eq. (2.5), $E_{12}(r) = \mu_0 \chi^2 B^2 / 4\pi r^3$. To be able to map the magnetic inter-particle interactions as a function of B, it is first important to know the magnetic susceptibility as the interaction potential scales as χ^2.

A SQUID (super conducting quantum interference device) is used to measure very weak magnetic fields and can be used to find the magnetic susceptibility χ [44]. The magnetisation curves measured by a SQUID magnetometer are shown in figure 2.3. These show the magnetic moment induced, per colloidal particle, as a function of the applied magnetic field. The probing magnetic field is taken up from 0 T via the two extremities in magnetic field and finally back up to the highest magnetic field again. The shape of the magnetic moment response is characteristic of super-paramagnetic particles. There is negligible hysteresis, a linear response regime at low applied magnetic field and a saturation at higher magnetic fields (where not shown, the plateau is at ~ 0.5 T). The full magnetisation curve, figure 2.3, can be represented by a Langevin equation:

$$\frac{m(B)}{m_0} = \coth(\alpha B) - 1/\alpha B \tag{2.8}$$

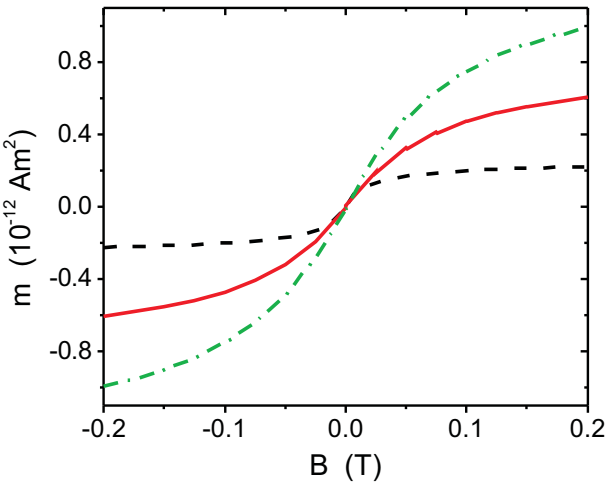

Figure 2.3: Magnetisation curve for super-paramagnetic colloidal particles of diameter 2.8 µm (dashes), 3.9 µm (solid) and 4.95 µm (dash dot), normalised per particle. All three particle sets show negligible hysteresis (probing field path 0 T → max T → - max T → max T).

where coth is the hyperbolic tangent, m_0 the saturation magnetisation and α a fitting parameter [20]. Expanding the right hand side as a first order Taylor series gives:

$$m(B) \simeq \frac{m_0 \alpha B}{3} = \chi B \tag{2.9}$$

where $\chi = m_0\alpha/3$. Using the approximation eq. (2.9) and m_0 and α found from Langevin fits to the magnetisation curves in figure 2.3, the magnetic susceptibility χ is found.

Particle type	Diameter µm	χ 10^{-12}Am^{2}T^{-1}
Dynabeads Polystyrene M-270	2.7	6.7
microParticles Polystyrene PS-MAG-S2180	3.9	6.4
microParticles Polystyrene PS-MAG-COOH-S2490	4.95	9.3

2.2 Optical tweezing and microscopy

2.2.1 Optical microscopy

Optical microscopy is used throughout this thesis to study 2D colloidal systems. The oldest known form of optical microscope is that produced around 1600 when two lenses were mounted

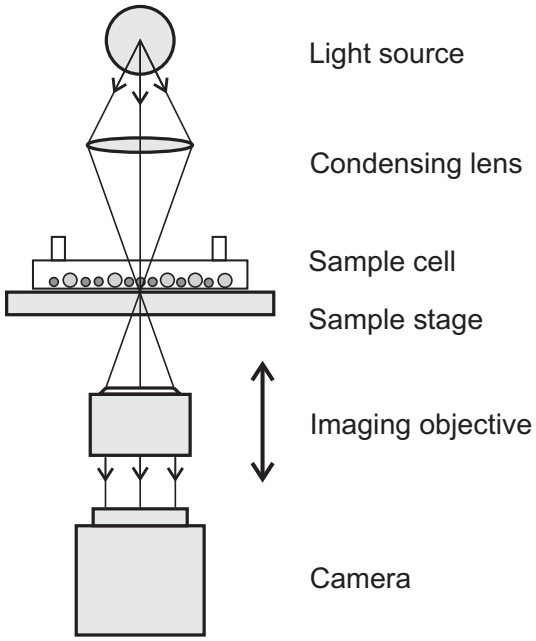

Figure 2.4: Schematic of the general construction of an optical microscope (sample cell not to relative scale). The condensing lens directs light onto the sample. The transmitted light is then focused by the movable imaging objective onto the camera.

into a tube to create the first compound microscope [45]. Since then, the basic optical microscope has changed little, mostly only with improvements in illumination and lens quality. A schematic diagram in figure 2.4, displays the general components of an optical microscope; the sample is illuminated from the top by the light source and condenser, and the transmitted light is then focused onto the camera by the movable imaging objective.

The spatial resolution of a microscope is related to the numerical aperture of the objective, NA, and the wavelength of light, λ. The smallest distance, d, that can be resolved is given by $d = \frac{\lambda}{2\mathrm{NA}}$, where the numerical aperture is equal to $n\sin(\theta)$. The refractive index of the medium between the object and lens is given by n, and θ is half the angle of the cone of light that can enter the objective. Objectives with a higher NA let in light from greater angles and improve image resolution, but at the cost of decreasing the focal length. Typically dry microscope objectives of magnification 20× to 40× and NA > 0.4 are used in this work, which results in good image quality whilst keeping a useful focal length of about 2 mm.

2.2.2 Optical tweezers: a brief history

An optical tweezer is a focused beam of light with which particles of size comparable to the wavelength of light can be manipulated. The ability of light to exert a force on micron-sized particles was first demonstrated by Arthur Ashkin in 1970 [46]. Ashkin demonstrated how a weakly focused laser beam could draw objects which had a greater refractive index than the surrounding medium, towards the beam centre. The objects were also propelled along the direction of light by the radiation pressure of the laser. Using gravity to balance the laser radiation pressure he then demonstrated how particles could be trapped and moved by the laser beam in an inverted geometry [47]. The first single beam gradient force optical trap was created by Ashkin and co-workers in 1986 [48], where a highly focused laser beam gave the ability to trap a particle in three dimensions.

The importance and usefulness of optical tweezers was first recognised in biology to trap cells and viruses [49]. Nowadays, optical tweezers are an important non-invasive technique for trapping and manipulating objects in a wide range of disciplines from biology to physics [50–53]. In colloidal science their uses range from measuring particle interactions to defect creation in 'colloidal crystal engineering' [22, 54–58].

2.2.3 Optical tweezer theory

A single beam gradient-force optical tweezer is created by focusing a laser beam through a high numerical aperture objective lens. A potential energy well is created in 3D by the strong light gradient around the focal point. A particle with a refractive index greater than the surrounding medium can be trapped in this diffraction-limited spot. If there is no difference in refractive index then the particle feels no force.

There are three regimes and theories behind the physics of optical trapping, selected according to the ratio of the particle radius, R, to the wavelength of the laser forming the optical trap, λ. The Rayleigh regime applies where $R \ll \lambda$, the Mie regime where $R \sim \lambda$ and the ray optics regime where $R \gg \lambda$. In the Rayleigh [59] and ray optics regimes, the physics behind the optical trapping can be explained by decomposition of the total force on the particle into

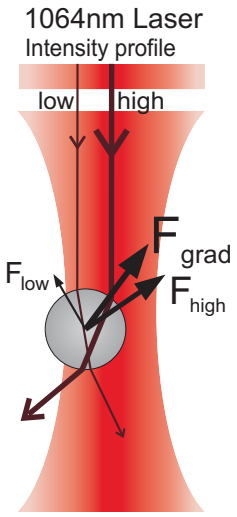

Figure 2.5: A qualitative picture of optical trapping due to the gradient force. The laser beam refracts through the sphere. The change in the momentum of light is matched by an opposite momentum change in the particle. The off-axis sphere experiences a net force F_{grad} towards the beam centre as a greater momentum change contribution is felt due to the higher intensity beams at the centre.

a 'scattering' and a 'gradient' force. Mie theory is far more complex and cannot be explained by the same force argument [60, 61]. In the Rayleigh and ray optics regimes, the scattering force always acts along the optical axis, pushing the particle out of the focus along the beam. The gradient force acts to attract the particle towards the beam centre. Most commonly, optical tweezers are used where the particle size and laser wavelength are comparable. The latter regime of ray optics will be focused upon here as it is the most intuitive of the theories, though strictly speaking the less well understood Mie regime is more applicable in the systems studied here where $\frac{R}{\lambda} \sim 3$.

The principle of ray-optics was first described by Ashkin in 1992 and is best described pictorially as in figure 2.5 [62]. The light beams incident on the particle refract and change direction on entering and leaving the particle. This corresponds to a change in momentum of the light ray. To conserve momentum, the particle gains a momentum to balance the change. The gradient force is that felt by the particle after summing over all the momentum contributions from all the refracted light rays. If a particle is centered in a trap then the gradient forces created by refraction on either side of the beam centre cancel out. If, as in figure 2.5, the particle is off axis then the gradient force seeks to re-centre the particle. Light rays nearest the optical axis

have the highest intensity and give a greater contribution, F_{high}, to the gradient force than the outer rays, F_{low}, that seek to pull the particle outwards. This results in an effective gradient force, F_{grad}, directed towards the highest light intensity gradient at the beam centre.

The scattering force is due to the reflection of light off the particle, this pushes the particle in the direction of light propagation. If the intensity gradient, and therefore the gradient force, is high enough to overcome the scattering force and any effective particle weight, then the particle can be trapped in 3D. Due to the potential energy well created by the focused laser beam, the focal point of an optical tweezer is referred to as an optical trap. Note that in this work, only optical tweezing in 2D is used, hence the scattering force is less important.

2.2.4 Beam steering

The principle of an optical trap being a highly focused laser beam has not changed since the early work by Ashkin and coworkers [48], but there have been many advances in beam control. Collimated light directed along the optical axis will result in an optical trap in the centre of the trapping plane. Several beams can then be created from a single laser source using a beam splitter, before being directed to the tweezing objective to create multiple traps. Though these methods can be used to create multiple traps in 3D, the number of traps and amount of control is limited by the number and quality of the lens and mirror optics.

A solution to translation of the trap in a direction perpendicular to the optical axis, is to time-share one optical trap. In colloidal systems, where the typical Brownian time is on the order of $1 - 10$ s, a beam that can cycle round between spots at 10 Hz can create at least 10 optical traps which are static from the view point of the colloidal particles. Early systems used galvano-scanning mirrors [63] and piezoelectric systems [64] for mirror control to direct a beam quickly between spots and create multiple optical traps. However, due to the inertia of the moving mirrors these systems were limited to creating on the order of 10 traps. Acousto-optic deflectors (AODs) can time-share one optical trap over hundreds of positions in the focal plane [65]. A schematic of an AOD is shown in figure 2.6. Directing the beam through two perpendicularly placed AODs allows control of the beam via deflection in the horizontal and vertical directions respectively. An AOD contains a $Te0_2$ crystal attached to a piezoelectric transducer base. A

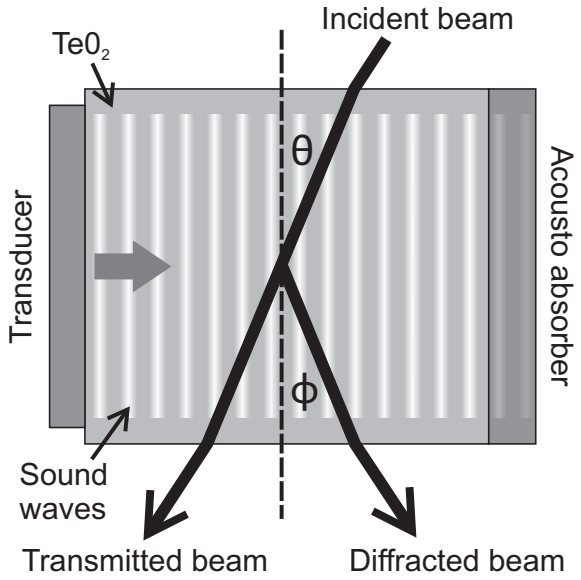

Figure 2.6: Illustration of the principle operation of an acousto-optic deflector. A radio frequency field is applied to the piezoelectric transducer which creates sound waves that propagate to the right through the TeO_2 crystal and are absorbed by the acousto absorber. The density variation set up in the TeO_2 crystal acts as a grating through which the incident laser beam is diffracted, producing here, a first order diffracted beam and an undiffracted transmission beam.

radio frequency voltage is applied to the piezoelectric transducer, which then propagates a sound wave through the $Te0_2$ crystal, before being absorbed by the acousto absorber. The density variation set up in the crystal by the sound wave acts as a diffraction grating. A laser beam incident at the Bragg angle θ is diffracted by the grating by an angle ϕ, this creates the first order diffracted spot. Some laser light passes through the grating undiffracted and forms the zeroth order transmission beam. The diffracted grating is not created mechanically so the grating can be changed with a frequency on the order of 100 kHz, enabling ideally hundreds of traps to be created. The angle ϕ of the first order output beam can be altered by changing the sound wave frequency, the beam's intensity can be controlled by the sound wave amplitude. Placing two AODs perpendicularly to each other in the beam path then gives control of the incident beam in the horizontal and vertical directions. The result is four principle beam paths outputted from the combined AODs, the transmission zeroth order (0,0), a (0,1), a (1,0) and the first order (1,1). During alignment of the TeO_2 crystals, the maximum amount of the incident beam as possible is directed into the (1,1) order, typically achieving $\sim$60 % efficiency. The (1,1) beam is used to form the optical tweezer, giving control of the optical trap in a 2D plane.

AODs can only create optical traps in one plane. A Pockels cell can be used with an AOD to give tweezing in two planes [66], but to create 3D tweezing a different approach is required. Holographic optical tweezers can create multiple optical traps in 3D arrangements by using a computer controlled hologram and a spatial light modulator [67–69]. The holograms, and hence the trap positions can be changed in real time, therefore creating a powerful technique for multi-object manipulation in fields ranging from nano-technology [70], biology [71, 72] to microfluidics [73].

2.2.5 Experimental set-up

Two experimental set-ups are used in this work, a stand-alone Olympus inverted bright field microscope and a custom-built inverted bright field microscope as part of an optical tweezer set-up. All the microscope designs are inverted to allow observation of colloidal particles from underneath the sample. A picture of the optical microscope section of the optical tweezer is shown in figure 2.8, along with a schematic drawing of the whole optical tweezer set-up in figure 2.7. Here follows a step-by-step guide through the optical tweezer set-up as shown in figure 2.7. A diode pumped Coherent Compass continuous wave neodymium vanadate laser, vertically polarised with a wavelength of 1064 nm is used. Firstly, the beam is expanded about $10\times$ in the beam expander, lenses L_1 and L_2. The vertically polarised laser beam then passes through the lambda-half plate, W_1, and is reflected in the polarising beam splitter, B_1. Altering the beam polarisation with the lambda-half wave plate enables the beam to pass straight through the beam splitter into a different set-up if required.

The vertically polarised light is directed into first the vertical then the horizontally positioned AODs, the acousto-optic deflectors (Opto-Electronic), which make up the beam steering system. In each AOD a sound wave propagating through a TeO_2 crystal sets up a standing wave diffraction grating. This diffraction pattern deflects the laser beam at different angles and intensities according to the sound wave frequency and amplitude respectively. Each AOD diffracts the incident laser beam into a first order beam and a transmission, zeroth order beam. Careful alignment of the horizontal and vertical AODs results in $\sim 60\%$ of the laser light being directed into the (1,1) beam. The mirror, M_1, is positioned to only select the (1,1) beam. Any higher order beams along with the lower order (0,0), (0,1) and (1,0) are directed away. The diffrac-

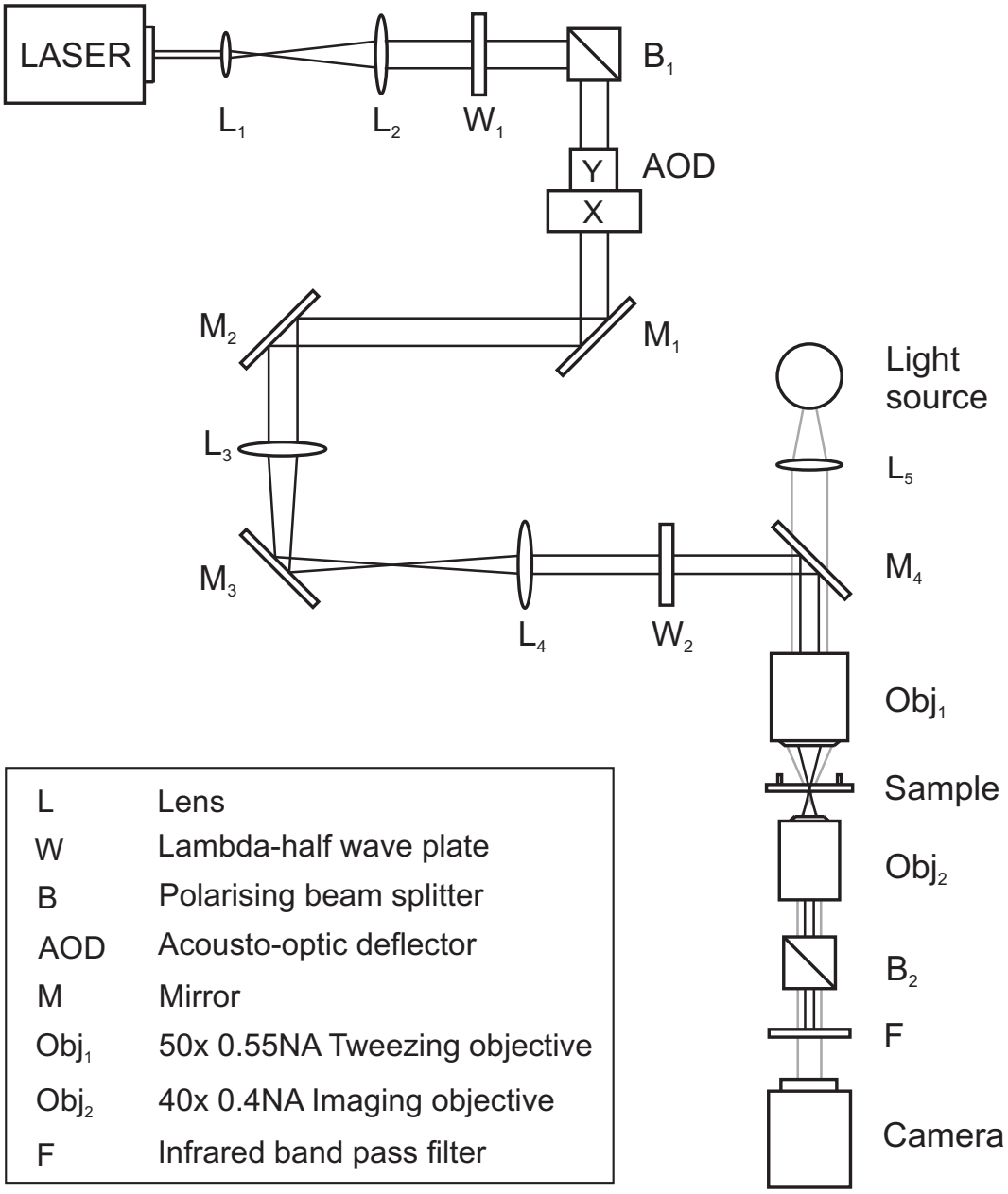

Figure 2.7: A schematic of the experimental set-up to create an upright optical tweezer and an inverted transmission optical microscope.

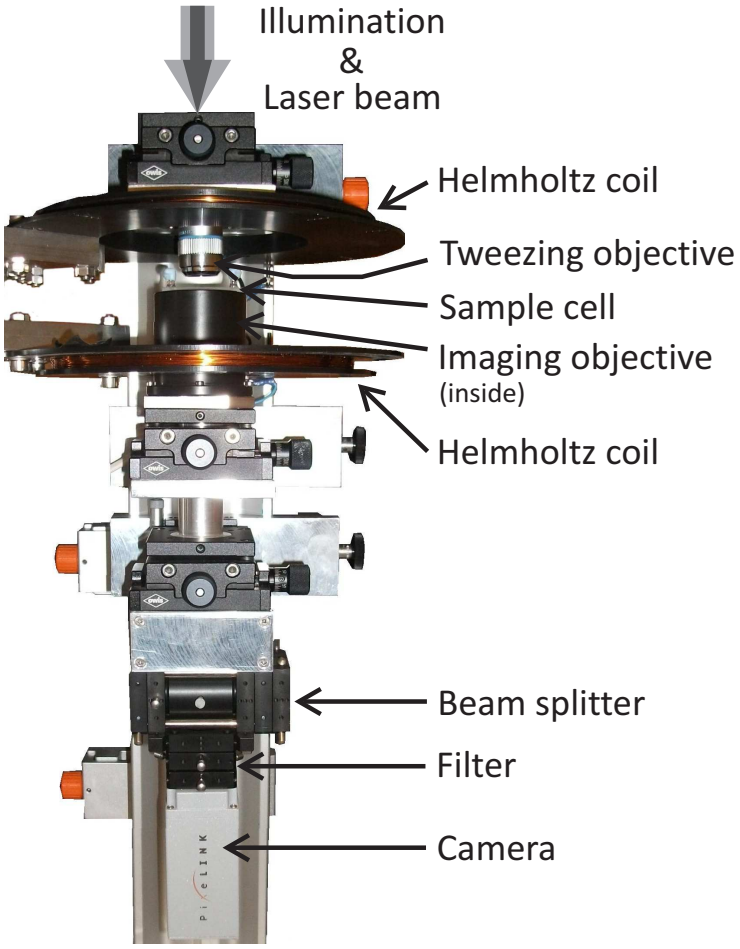

Figure 2.8: Picture of the optical microscope and optical tweezer section of the whole optical tweezing set-up (figure 2.7).

tion patterns and hence the optical trap positions are controlled via the user interface software Aresis 'Tweez'. Tweez links to an Aresis beam steering controller which in turn is connected to the AODs. Tweez also links to the camera output allowing direct real time control over the optical trap positions in the 2D trapping plane, while superimposed over the microscope images. Multiple optical traps and arrays of traps can be created and moved in real time, enabling great flexibility over the optical trapping procedures.

In the next section, including mirrors M_1, M_2 and M_3 the beam is directed up and onto a tower on the workbench, such that the later sections form an upright inverted microscope on the other side of the tower (figure 2.8). This section also includes a telescope, lenses $L3$ and $L4$, that focuses the beams projected from the AODs at variable angles, into the back aperture of the tweezing objective. After the telescope, the next component is the lambda-half wave plate

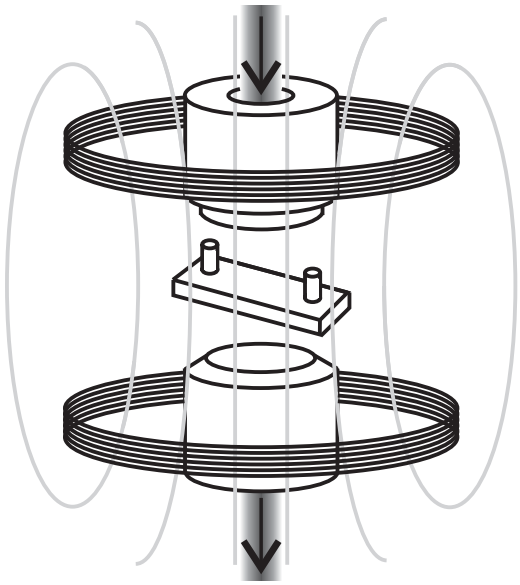

Figure 2.9: A schematic of the Helmholtz coils (diameter 15 cm) around a Hellma cell. The tweezing (Leica 50 × 0.55 NA)(top) and imaging objectives (Zeiss 40 × 0.4 NA)(bottom) are shown along with a representation of the magnetic field lines.

W_2. This is used in conjunction with the polarising beam splitter B_2. Often, it is desirable to observe the laser beam whilst operating the tweezer. So as not to damage the camera, the beam intensity must be reduced whilst not affecting the beam at the sample position. The infrared bandpass filter, F, is removed and the amount of laser light reaching the camera is controlled by altering the beam polarisation with the wave plate. The intensity of the beam reaching the camera is reduced as non-vertically polarised light is redirected into a beam dump via B_2.

The final section forms the custom-built optical microscope and tweezer. The laser beam is directed into the back aperture of the tweezing objective, Obj_1, (Leica 50 × 0.55 NA) along with light from the illumination light source (ThorLabs Halogen bulb) via the infrared reflecting mirror M_4. The tweezing objective focuses the laser beam into the imaging plane, located in the sample, forming an optical trap. The trap can be translated up to 40 μm in each direction and time shared at frequencies up to 100 kHz using the AODs, which allows the creation of many arrays of traps. The resulting transmission image is collected by the imaging objective, Obj_2, (Zeiss 40 × 0.4 NA) and directed through the beam splitter to the filter. If in operation, the infrared bandpass filter absorbs the laser beam, the imaging light passes through and is captured by the 8 bit (1280 × 1024 pixels) grayscale CMOS camera (PixeLINK). All lenses are made by Melles Griot and movable sample stages (not shown) by Owis. The optical tweezer set-up was

originally designed in Clemens Bechinger's group at the University of Stuttgart.

The optical tweezer and microscope is also equipped with two Helmholtz coils around the objectives and sample as shown in figure 2.8 (not shown in figure 2.7). The Helmholtz coils can generate magnetic fields of up to $\pm$ 4 mT perpendicular to the imaging plane, as illustrated in figure 2.9. The large coil radius with respect to sample size ensures a homogeneous field across the sample.

The standard Olympus inverted bright-field microscope which forms the additional set-up is not shown here. This experimental arrangement also has Helmholtz coils to generate magnetic fields in a similar arrangement to in figure 2.9. This set-up was used solely for microscopy and used for the work in chapter 6 on 'Particle dynamics in random confinement'.

2.2.6 Sample cells

Custom built Hellma sample cells, see figure 2.10, were used for most projects. These reusable quartz glass cells have main body dimensions of $45 \times 13 \times 3$ mm and an inner channel of width 10 mm and height 200 μm. These cells are easily filled by pipette with colloidal suspensions and the channel sealed with Blu-Tack. Quartz glass is hydrophilic, creating a small surface charge in water that repels the likewise negatively charged colloidal particles, and so minimising colloidal particles adhering to the surface. The Hellma cells are cleaned periodically with strongly alkaline Hellmanex solution, this dissolves any biological matter including any colloidal particles.

Figure 2.10: A Hellma sample cell containing 2.8 μm super-paramagnetic polystyrene colloidal particles. The colloidal particles are brown due to them containing iron oxide nanoparticles. The cell has length 45 mm, width 13 mm and internal height 200 μm. The inlet channels are sealed with Blu-tack.

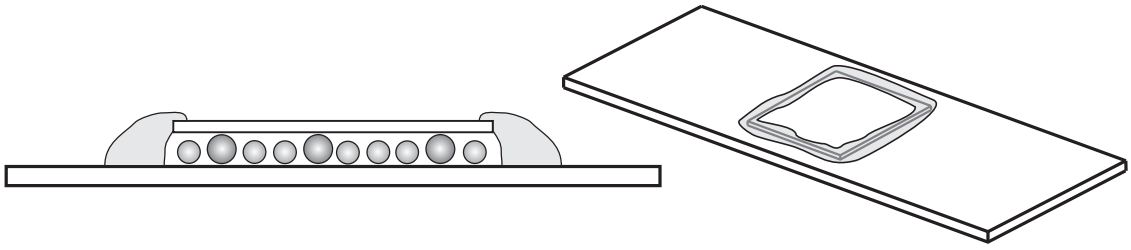

Figure 2.11: Left: An illustration (not to relative scale) showing how the 2D confinement is created by the large particles that act as spacers to support the top slide. UV glue seals the cell. Right: illustration of the whole 2D sample cell, approximately to scale.

In chapter 6 on 'Particle dynamics in random confinement', 2D confinement is created by sandwiching a colloidal sample between a large lower glass slide and small upper glass cover slip, see figure 2.11. A binary system is used so that the larger particles act as spacers and support the glass cover slip. The volume of the colloidal suspension is set to 1.11 μl to create a cell of height 4.95 μm over the area of the glass cover slip (dimensions 15×15 mm). After applying a small amount of pressure to the cover slip, to aid the liquid spreading to the edges, UV glue is used to seal the cell around the edges.

2.3 Particle detection and image analysis

All experiments within this thesis rely on accurately tracking the positions of the colloidal particles from the microscopy images. The images from the microscope are captured by a PixeLINK CMOS camera and saved to a computer as 8 bit 1280 x 1024 pixel images. Good spatial resolution of the colloidal particle positions is achieved as each particle is at least 10 pixels in diameter.

Each colloidal particle appears as a circularly symmetric intensity profile in the captured images, see figure 2.12a. This allows the centre of each particle to be found to good accuracy. The general image processing procedure is described below and in figure 2.12. After image capture the images, see figure 2.12a, are filtered using a bandpass filter in Image J. This enhances the intensity profiles relating to the specified particle size to produce figure 2.12b, noise and unwanted size objects are suppressed. Next, the filtered images are imported into IDL (Interactive Data Language) to find the particle positions. The images are processed using IDL routines developed

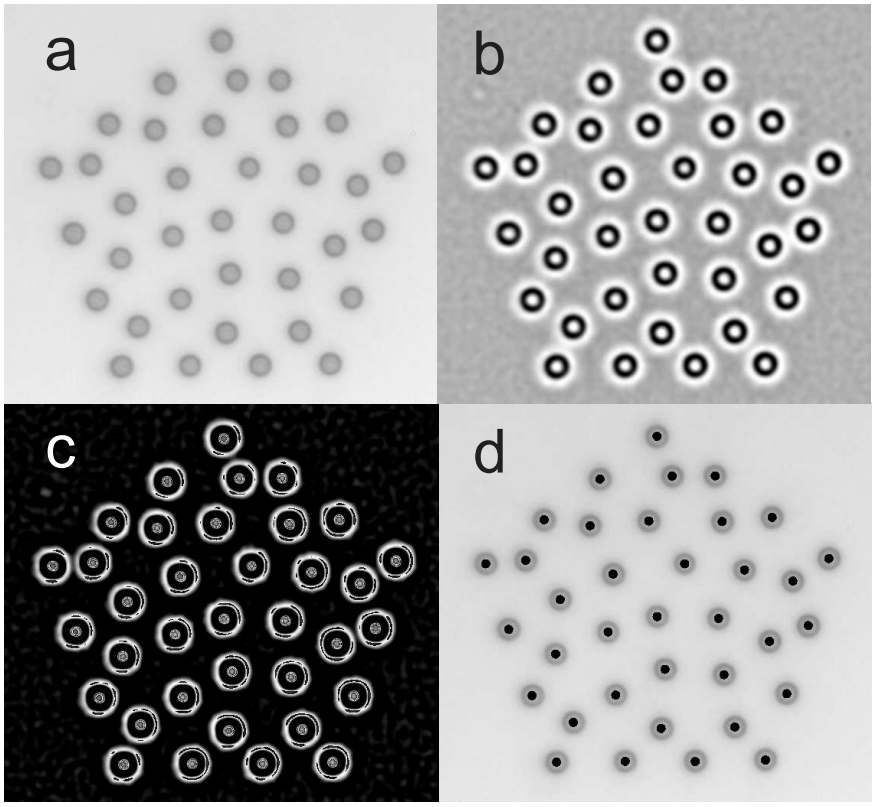

Figure 2.12: An example of image processing from the raw image to the particle coordinates. a) Raw image taken with a PixeLINK CMOS camera. b) Image processed with bandpass filter in Image J. c) Image processed with bandpass filter in IDL. d) Plot of detected particle positions on top of the original image.

by Crocker and Grier [74]. First, an additional bandpass filter, 'bpass', is applied to each image, producing figure 2.12c. Once filtered the routine 'feature' is applied to locate the particle positions by fitting a Gaussian profile to all signals. The resulting coordinates are then sorted by the radius of gyration, eccentricity and brightness of their corresponding signals, to select only the particle coordinates. For illustration, the resultant particle coordinates are plotted back on the original image in figure 2.12d.

To assign an identity to each particle, so that its position can be tracked through time, another routine by Crocker and Grier, 'track' is used. The result is a 2D array, x, y, t, i, containing for each particle, i, the x and y coordinates at time t. Lastly, before the particle positions can be analysed, a drift correction is carried out. No bulk concerted movement of the colloidal particles is expected in the systems studied here, but small amounts occur due to objective and sample position drift induced by temperature variation and vibrations. In certain

projects, for instance the pentagonal confinement chapter, a selection of particles are fixed by the optical tweezer. In these cases all the particle positions are referenced relative to these static particles. In the grain boundary work, chapters 3 and 4, the particle positions are referenced to the bulk crystal away from the interface. The particle coordinate data is now in a form to be analysed.

Acknowledgments

The Clemens Bechinger group at the University of Stuttgart is thanked for the basic optical tweezing set-up design and Andrew Bothroyd from the University of Oxford for use and assistance with their SQUID magnetometer.

Chapter 3

Grain boundary fluctuations in 2D colloidal crystals

ABSTRACT

The fluctuations of grain boundaries are studied in two-dimensional (2D) colloidal crystals using optical video microscopy. The grain boundary fluctuations are quantified by static and dynamic correlation functions which are both accurately described by expressions derived from capillary wave theory. This directly leads to the key parameters that describe the grain boundary, the interfacial stiffness and interface mobility. These parameters are of central importance to the phenomenon of curvature driven grain boundary migration. Furthermore, the average grain boundary position is demonstrated to perform a one-dimensional random walk as suggested by recent computer simulations [Science **314**, 632 (2006)]. The value for the interfacial mobility inferred from this method is in good agreement with those found from the grain boundary fluctuations.

This chapter is based on and reprinted with permission from [Thomas O. E. Skinner, Dirk G. A. L. Aarts and Roel P. A. Dullens, (2010), *Grain-boundary fluctuations in two-dimensional colloidal crystals*, Phys. Rev. Lett. 105, 168301].

3.1 Introduction

Material microstructure is characterised by the distribution of defects present throughout a material's structure. Even crystalline systems contain many imperfections including dislocations and grain boundaries. Creation of these defects can arise due to stresses on the crystal or as a result of freezing-in during crystallisation and grain growth. These microstructural defects, their frequency and distribution, define the physical properties of many materials including metals, composites and ceramics [75–77]. More specifically, grain boundaries are important due to their role in many technological materials including high temperature superconductors [78], thin films for corrosion and wear resistant coatings [25, 79] and in the emerging field of graphene research [80]. The size and quantity of different crystallites is notably important for the material's mechanical properties, whose material strength is directly related to grain size [81,82]. The evolution and motion of grain boundaries, and therefore the grain size, heavily influences processes including phase transformations, grain growth and recrystallisation [77,83]. As such, the key to understanding and controlling these processes is the ability to accurately describe grain boundary formation and migration.

Much of the current experimental knowledge of grain boundaries stems from detailed high-resolution transmission electron microscopy studies [84–87], yielding information on bulk grain boundary migration rates. However, accessing the fluctuations of atomic grain boundaries is a different matter, and is not yet possible due to the inherent time and length scales present in atomic systems [88]. Hence, only computer simulations have thus far been able to extract values for the interfacial properties from atomic grain boundaries [30, 89–94]. In contrast to atomic systems, the time and length scales associated with colloidal systems means interface fluctuations are more readily accessible [29, 95]. The ability to experimentally follow particle movement in real time and their thermodynamic equivalence, enables colloidal particles to act as model systems for atomic materials [96–99]. In this chapter, a 2D colloidal crystal is used to directly monitor grain boundary fluctuations in real space. Dynamic and static correlation functions of the fluctuating interfacial profile, which are well described by capillary wave theory, directly lead to the key grain boundary properties: the interfacial stiffness and mobility. In addition, the approach suggested in recent computer simulations [100], of determining the grain

boundary mobility from the diffusive motion of the mean interface position is experimentally confirmed.

3.2 Background

3.2.1 Grain boundaries and material properties

The structure of a polycrystalline material is made up of grains, or crystallites, each having a different orientation to the next. The interface between adjacent grains is known as the grain boundary, the only difference across the boundary is the grain orientation. As this work focuses on grain boundaries in two dimensional (2D) crystals, all further descriptions will apply to defects in 2D systems. In 2D, a grain boundary is a quasi-1D defect composed of an array of point defects termed dislocations, see figure 3.1. Each dislocation defect is in turn comprised of two disclinations. In a hexagonal lattice, see figure 3.1a, the two disclinations that constitute a dislocation are a 5-fold (positive) and 7-fold (negative) coordinated particle. As evidenced by the insertion of an extra (gray) line in figure 3.1a, an isolated dislocation is a defect that primarily affects the translational symmetry of the lattice. A free disclination, for instance an isolated 5-fold defect, disrupts the orientational order of the crystal. The appearance of first free dislocations and then free disclinations as temperature is increased, forms the basis of the KTHNY scenario for the melting of 2D crystals [101–103].

The importance of grain boundaries, in particular their effect on material properties, is demonstrated by the Hall-Petch law [104–106] which describes the strengthening of materials by changing the average grain size, see figure 3.2. A measure of material strength is the yield stress, which is the point at which a material starts fracturing and deforming plastically. The yield stress of a material is proportional to the resistance to moving dislocations through the microstructural landscape of defects and grain boundaries. Grain boundaries slow down the movement of dislocations and resist them traversing grains and propagating the fracture. This pinning effect stems from two intrinsic properties of grain boundaries; their disordered structure compared to the crystal and the orientation difference between the crystals, forcing the dislocation to change direction. Hence, increasing the grain boundary density (reducing the grain

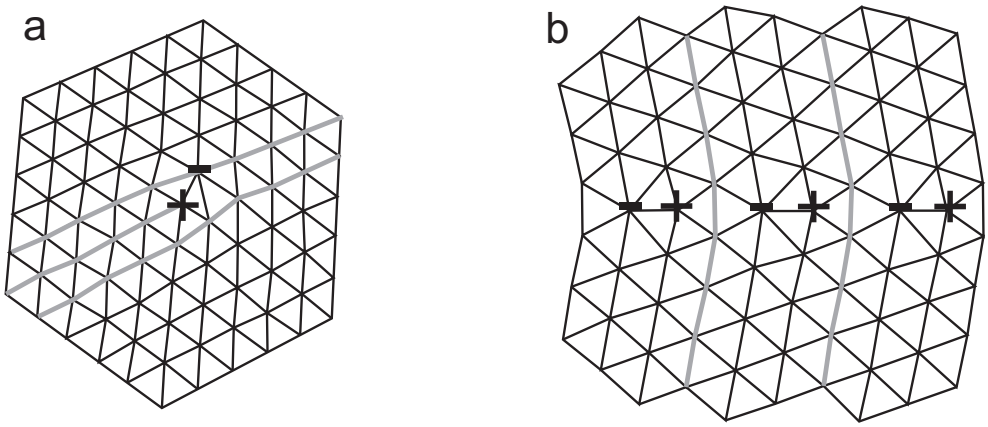

Figure 3.1: a) An example of an isolated dislocation. The dislocation consists of a 5 and 7-fold disclination, represented as a positive (+) and a negative (-) coordinated defect respectively. Vertices correspond to particle positions. The gray lines indicate the effective insertion of an extra row of particles which disrupts the translational order. b) A chain of dislocations forming a grain boundary. The gray lines illustrate the change in orientation across the interface.

size) can increase a material's strength by disrupting this dislocation slip. The Hall-Petch law states that the yield stress is proportional to the square root of the grain size and therefore as figure 3.2 illustrates, decreasing the grain size can increase the yield stress. This relationship applies down to a minimum grain size, after which the structure is so fragmented that grain boundaries now slide past each other. In this regime, the standard Hall-Petch law no longer applies, and the yield stress falls with decreasing grain size.

3.2.2 Grain boundary migration

Grain size defines material strength, and grain growth is affected by grain boundary migration, hence, understanding grain boundary migration is key to controlling grain size. Grain boundaries naturally migrate through the crystal as both thermal fluctuations and interfacial curvature seek to shape the interface. Indeed, a polycrystalline structure is not in equilibrium; the grains will continue to grow until one crystal is formed, albeit very slowly. Other driving forces can emanate from imbalances or gradients in pressure, defect density or temperature [107, 108]. During grain growth and recrystallisation an important driving force for microstructure evolution is the interfacial curvature. This is the drive towards a reduction in the grain boundary surface area, which competes against the roughening effect of thermal fluctuations. In the curvature driven

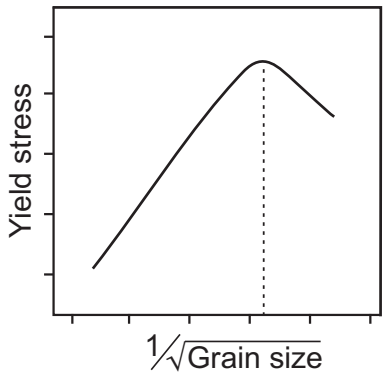

Figure 3.2: Hall-Petch strengthening by decreasing the grain size. Increasing the grain boundary density reduces the propagation of dislocations and increases the yield stress. At very small grain sizes the yield stress reaches a maximum and decreases due to grain boundary slip. Note the grain size is plotted, as is convention, as an inverse scale.

regime the driving forces, P, on the crystal are typically small such that the grain boundary velocity, ν, can be assumed to be directly proportional to the driving force:

$$\nu = MP \tag{3.1}$$

where the proportionality constant, M, is the interface mobility [84, 109]. The mechanism of grain boundary migration is not well established, but is most likely facilitated by a combination of hopping across and cooperative motion along the interface, as suggested by simulations [110–112]. This suggests that migration of grain boundaries is thermally activated, and that the mobility may be represented by an Arrhenius relation [113] as:

$$M = M_0 e^{-Q/RT} \tag{3.2}$$

where Q is the activation energy for boundary movement, M_0 is a weakly temperature dependent pre-exponential factor, R the gas constant and T the temperature. The grain boundary mobility is a measure of the ease with which a grain boundary migrates and is a property of the interface at a specific orientation and temperature [111, 114, 115].

For curvature driven grain boundary migration, the driving force P depends on γ, the interfacial free energy, γ'' its second derivative with respect to the boundary orientation and κ

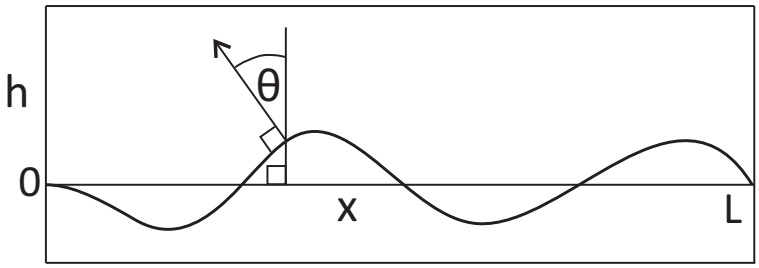

Figure 3.3: An illustration of the interface profile, $h(x)$, of length L and displaying the angle θ for the slope at a position along the interface.

the interfacial curvature as given by the Herring relation [75]:

$$P = (\gamma + \gamma'')\kappa \tag{3.3}$$

For a 1D interface, κ is the second derivative of the interface height, h, as a function of position x along the interface, $\kappa = \frac{d^2h}{dx^2}$, see figure 3.3. Combining the expressions for the interface velocity eq. (3.1) and for the driving force eq. (3.3) gives:

$$\nu = M(\gamma + \gamma'')\kappa = M\Gamma\kappa \tag{3.4}$$

where $\Gamma = \gamma + \gamma''$ is the interfacial stiffness. The interfacial stiffness contains the orientation dependence and is a significant parameter in anisotropic systems, especially in grain boundaries. Here, the anisotropy in the stiffness is much greater than that in just the interfacial energy. The anisotropy in the interfacial energy is well studied in grain boundaries [116–119], but due to the difficulty of calculating the interfacial stiffness it became common practice to neglect the γ'' term. Considering the full stiffness, rather than just the interfacial energy, was confirmed to be important in Ising model grain boundary simulations [120]. In solidification, the stiffness is well known to be important as its orientation dependence helps control dendrite growth and orientation [89]. As eq. (3.4) demonstrates, the key parameters that govern the structure and dynamics of curvature-driven grain growth are the interfacial stiffness and mobility. Experimentally extracting these two parameters forms the main focus of this work.

There are various ways of characterising the interfacial properties, like the interfacial tension and mobility, of a grain boundary from experiments [84, 121]. However, the extraction of accurate interfacial stiffness values is more difficult [90, 122, 123] due to the difficulties of

controlled experiments on grain boundaries [124]. Therefore, there has been a rapid increase in the number of grain boundary simulation studies, mostly using molecular dynamics (MD) [30, 91, 92, 94, 100, 125]. Many of these simulations [30, 90, 91, 100, 126] are based on an elegant zero-driving force approach where the grain boundary stiffness and mobility are extracted from the equilibrium grain boundary fluctuations. In this thesis, this analysis of the grain boundary fluctuations during the curvature driven regime is applied to the grain boundary fluctuations observed in colloidal experiments.

3.2.3 Capillary wave theory

Grain boundary fluctuations are the sum of thermally excited capillary waves [127–129]. This forms the basis of the capillary fluctuation method from which the interfacial properties, the stiffness and mobility, can be determined [30, 89]. The free energy change of disturbing a 1D interface can be expressed as $dE = \gamma(\theta)ds$ where ds is the change in arc length of the displaced interface and $\gamma(\theta)$ is the interfacial tension as a function of the angle, θ, between the interface normal at x and the normal of the flat interface. An illustration of the interface is shown in figure 3.3. A change in arc length, ds, can be represented via Pythagoras's theorem as:

$$ds = \sqrt{1 + \frac{dh^2}{dx^2}}\, dx \tag{3.5}$$

where $h(x)$ is the interface height at position x along the interface. The free energy of the whole interface spanning the system size L can then be written as:

$$E = \int_0^L \gamma(\theta)\sqrt{1 + h'(x)^2}\, dx \tag{3.6}$$

where the prime represents differentiation with respect to x. The anisotropy in $\gamma(\theta)$ can be expanded to second order in θ:

$$\gamma(\theta) \approx \gamma + \gamma'\theta + \frac{\gamma''}{2}\theta^2 \tag{3.7}$$

where the prime denotes differentiation with respect to θ. Assuming that the interfacial fluctuations are small in amplitude, the arc length can be simplified to:

$$\sqrt{1 + h'(x)^2} \approx 1 + \frac{h'(x)^2}{2}. \tag{3.8}$$

and θ can be given in terms of the derivative of h as $h^{'} = \frac{dh}{dx} = \tan(\theta) \approx \theta$. Substitution of eq. (3.7) and eq. (3.8) into eq. (3.6) results in:

$$E = \int_0^L \left(\gamma + \gamma^{'} h^{'}(x) + \frac{\gamma^{''} h^{'}(x)^2}{2}\right)\left(1 + \frac{h^{'}(x)^2}{2}\right) dx. \tag{3.9}$$

The free energy cannot depend on the sign of the gradient of the function h, therefore, when multiplying out eq. (3.9), the $h^{'}(x)$ and $h^{'}(x)^3$ terms produce no contribution. The term to fourth order, $h^{'}(x)^4$, is negligible in size and so the expression becomes:

$$E = \int_0^L \left(\gamma + \frac{\gamma h^{'}(x)^2}{2} + \frac{\gamma^{''} h^{'}(x)^2}{2}\right) dx. \tag{3.10}$$

Integrating out the first term gives $L\gamma$, the free energy of the flat interface. Defining $\Delta E = E - L\gamma$ and substituting in the stiffness, where $\Gamma = \gamma + \gamma^{''}$, gives:

$$\Delta E = \frac{1}{2}\Gamma \int_0^L h^{'}(x)^2 \, dx. \tag{3.11}$$

The interface profile $h(x)$ is expressed as a sum of capillary waves, $h(x) = \sum_k A(k) e^{ikx}$, which after differentiating yields:

$$h^{'}(x) = \sum_k ikA(k) e^{ikx} \tag{3.12}$$

where $k = n2\pi/L$. Substituting eq. (3.12) into eq. (3.11) gives:

$$\Delta E = \frac{1}{2}\Gamma \int_0^L \sum_{k_m} ik_m A(k_m) e^{ik_m x} \sum_{k_n} -ik_n A^*(k_n) e^{-ik_n x} \, dx \tag{3.13}$$

where $A^*(k)$ is the complex conjugate of $A(k)$. Next, the expression can be simplified by combining the exponents to give:

$$\Delta E = \frac{1}{2}\Gamma \int_0^L \sum_{k_m} \sum_{k_n} k_m k_n A(k_m) A^*(k_n) e^{ix(k_m - k_n)} \, dx \tag{3.14}$$

For the case when $k_m \neq k_n$, then the argument of the integral is the sum over all wavelengths and has no contribution. For $k_m = k_n$, the exponential term collapses to 1 and the expression simplifies to:

$$\Delta E = \frac{1}{2}\Gamma \sum_k Lk^2 A(k) A^*(k) \tag{3.15}$$

From the equipartition theorem it follows that each k mode contributes an average energy of $\frac{1}{2}k_BT$, so therefore $k_BT = L\Gamma k^2\langle|A(k)|^2\rangle$, from which the static fluctuation spectrum for a 1D solid-solid interface is obtained [128, 129]:

$$\langle|A(k)|^2\rangle = \frac{k_BT}{L\Gamma k^2} \tag{3.16}$$

where the angular brackets denote a configurational average. This power spectrum forms the basis of the capillary fluctuation method [30, 89–91].

To obtain the dynamic correlation function, Hoyt *et al.* [30], used a generalised Langevin equation analysis to determine an expression for the time dependence of the mean square amplitude. This corresponds to a dynamic correlation function of the amplitudes of the Fourier components, $A(k)$:

$$\langle A(k,0)A^*(k,t)\rangle = \langle|A(k)|^2\rangle e^{-M\Gamma k^2 t} \tag{3.17}$$

where $A^*(k,t)$ is the complex conjugate and the decay time is $\tau(k) = 1/(M\Gamma k^2)$. Substituting the expression for the static capillary fluctuation spectrum, eq. (3.16), for the k^2 in the definition of τ, results in:

$$\langle|A(k)|^2\rangle L\tau^{-1}(k) = Mk_BT. \tag{3.18}$$

The interface mobility can thus be extracted via finding τ from the decay of $\langle|A(k)|^2\rangle$ for each wavevector.

The remainder of this chapter is organised as follows. Firstly, the experimental methods and the interface localisation are described. Next, the grain boundary fluctuations are analysed in terms of first the spatial and then the dynamical correlation functions. In each case, a real space methodology is derived from the standard Fourier space capillary fluctuation method before a comparison to the Fourier space method is made. Lastly, in section 3.4.3, the applicability is demonstrated, and then the interfacial properties determined, via a fluctuation-dissipation based real space method developed by Trautt *et al.* [100].

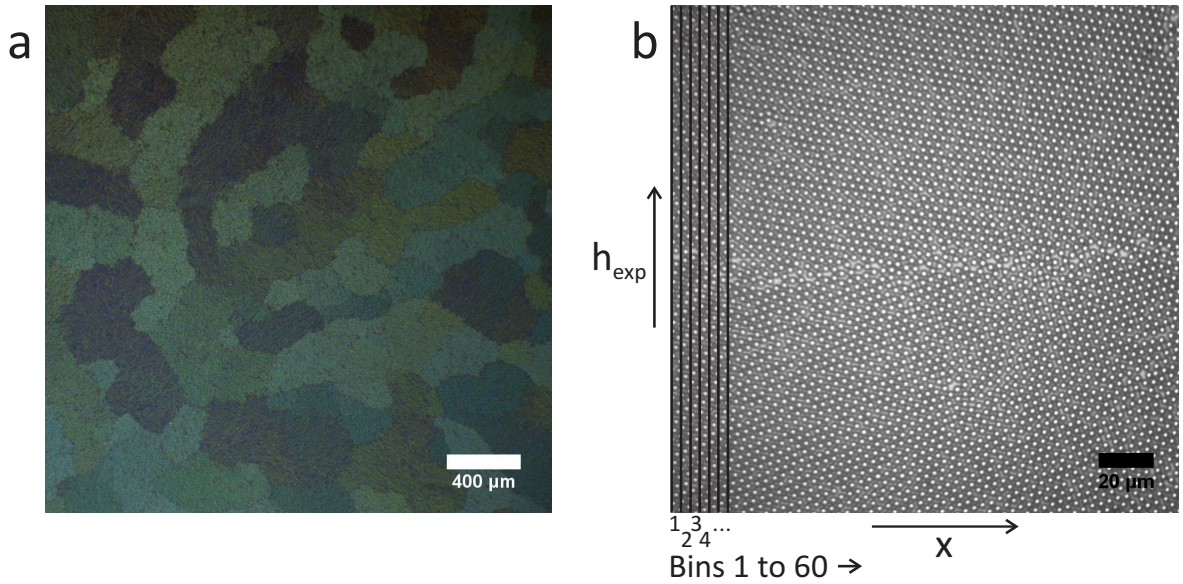

Figure 3.4: (a) An example of a 2D colloidal crystal formed from 2.7 µm diameter melamine formaldehyde colloidal particles and displaying a network of grain boundaries visible as the interfaces between the (false) coloured grains. b) An example of a grain boundary image at the resolution used in the experiment. The approximate size of the slices of the interface used as bins 1 to 60 is shown. The interface position is found within each bin to create the overall interface profile seen in figure 3.5.

3.3 Experimental methods and data analysis

3.3.1 Colloidal model system

As introduced in chapter 2 section 2.1.5, 2.7 µm diameter melamine formaldehyde spheres (microParticles) are used. The particles are dispersed in water where their carboxyl surface groups dissociate, creating a short-range screened Coulombic repulsion. The particles are contained in a 200 µm thick glass, Hellma sample cell and the number density is tuned such that a 2D hexagonal colloidal crystal is formed, as shown in figure 3.4b. As the particle size is much greater than the gravitational height, the out of the plane fluctuations of the particles are negligible. Using optical video microscopy long image stacks of the colloidal grain boundary (see figure 3.4b) of length $L \sim 180$ µm are recorded at 0.5 Hz for 2500 s. Standard particle tracking software is used to find the particle coordinates, as detailed in chapter 2 section 2.3 [74]. The particle coordinates are drift corrected with respect to a section of the bulk, and then rotated (4°) to

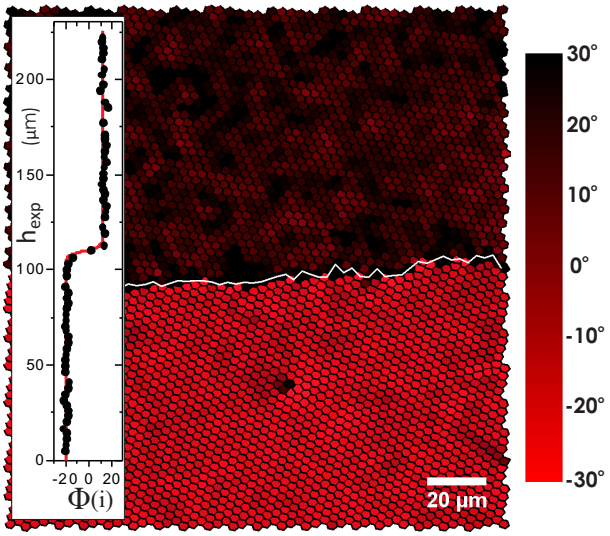

Figure 3.5: An orientational Voronoi plot corresponding to the grain boundary image in figure 3.4b. Each Voronoi cell represents a particle and its colour corresponds to the local orientation of the particle as indicated by the colour scale. The distinction in orientation between the crystallites is easily recognised. Inset: fitting a tangent-hyperbolic to the local orientation for a particular bin as a function of distance perpendicular to the interface. The interface is localised for each bin and then the complete interface found, as shown by the solid line.

bring the interface level. The grain boundary region has an area fraction of 70% and the grain boundary is unsymmetrical with an angle of 28°.

3.3.2 Interface localisation

To find the interface a local orientation parameter $\Phi(i)$ is assigned to each particle i. To this end, first a Delaunay triangulation is used to find the N nearest neighbour coordinates $\vec{r_j}$ of every particle i. Next the angle $\theta_j = \tan^{-1}[(\vec{y_j} - \vec{y_i})/(\vec{x_j} - \vec{x_i})]$, with $-\pi \leq \theta_j \leq \pi$, subtended from the central particle i to each of its nearest neighbours j is found. The orientation parameter is then obtained as $\Phi(i) = \frac{1}{N}\sum_j \theta_j$. The local orientation parameter can then be plotted for each particle in a Voronoi plot, see figure 3.5, where the colour scale represents the local orientation parameter. Figure 3.5 clearly displays the orientation difference between the crystals and the subtle fluctuations within the crystal bulk. Each grain boundary image is subsequently split into bins, of size approximately the particle diameter, perpendicularly to the interface direction, see illustration in figure 3.4b. Note the use of x as distance along the interface and h_{exp} as

distance in the perpendicular direction. The interface position within each bin is found from a tangent hyperbolic fit to the local orientation parameter plotted for all particles within the bin as a function of h_{exp}, see inset in figure 3.5. Note that the graph inset in figure 3.5 is displaying filtered points to improve the quality of the fits. Particles at the interface often have a random orientation, hence those with orientation outside the limits set by the averages of $\Phi(i)$ in both bulk crystals are ignored. As a result, the interface height h_{exp} as a function of the distance along the interface x and time t is obtained, $h_{exp}(x,t)$. To analyse the interface fluctuations, the interface averaged over all frames is subtracted: $h(x,t) = h_{exp}(x,t) - \langle h_{exp}(x)\rangle_t$.

3.4 Results and discussion

The colloidal grain boundary fluctuations are analysed in real space by constructing the time-dependent height-height correlation function:

$$g_h(x,t) = \langle [h(x_0,t_0)][h(x_0+x,t_0+t)]\rangle \tag{3.19}$$

where $\langle\rangle$ represents an average over all x and t.

3.4.1 Static correlation functions

The static correlation function, $g_h(x)$, averaged over all x_0 and time t, is expressed as:

$$g_h(x,t=0) = \langle h(x_0)h(x_0+x)\rangle \tag{3.20}$$

and shown in figure 3.6a. The correlation function shows a rapid monotonic decay and approaches zero around 20 μm. To extract the grain boundary stiffness from the static correlation function, it is noted that the interface position $h(x,t)$ can be written as $h(x,t) = \sum_k A(k,t)e^{ikx}$. Therefore, Fourier transforming eq. (3.16) will directly lead to a real space expression for $g_h(x)$ that can be fit to the experimental data in figure 3.6a. The Fourier transform of eq. (3.16) becomes:

$$g_h(x) = \frac{k_B T}{L\Gamma}\sum_k \frac{1}{k^2}e^{ikx}. \tag{3.21}$$

Converting the sum to an integral over all k values and expanding the exponent according to Euler's theorem produces:

$$g_h(x) = \frac{k_B T}{L\Gamma} \frac{L}{2\pi} \int_{-k_{max}}^{k_{max}} \frac{1}{k^2} [\cos(kx) + i \sin(kx)] dk. \tag{3.22}$$

Integrating over the odd $i\sin(kx)/k^2$ term produces no contribution. The $\cos(kx)/k^2$ term is even, therefore the integral limits can first be changed to $2\int_{k_{min}}^{k_{max}}$ and then assuming that $k_{min} = 0$ and $k_{max} = \infty$, the expression becomes:

$$g_h(x) = \frac{k_B T}{\pi\Gamma} \int_0^{\infty} \frac{1}{k^2} \cos(kx)\ dk \tag{3.23}$$

To avoid divergence of the integral as $k \to 0$, a lateral correlation length ξ is introduced which ensures a smooth long wavelength cut-off [130, 131]:

$$g_h(x) = \frac{k_B T}{\pi\Gamma} \int_0^{\infty} \frac{1}{k^2 + \xi^{-2}} \cos(kx)\ dk \tag{3.24}$$

Integrating produces a real space expression for the spatial correlation function, but now containing the interfacial parameters of the stiffness and correlation length.

$$g_h(x) = \frac{k_B T}{2\Gamma} \xi e^{-x/\xi} \tag{3.25}$$

Fitting the real space spatial correlation function, eq. (3.25), to the data, figure 3.6a, produces a very good fit, and yields a grain boundary stiffness of 1.7×10^{-15} Jm^{-1} and a correlation length of 4.9 μm. The length L of the boundary is much greater than ξ, demonstrating that the fluctuation spectrum is not affected by the finite interface length.

Alternatively, the spatial correlation result may also be approximated to the one point self correlation function. This is equivalent to the mean square interfacial width, as $\langle h^2 \rangle = g_h(0) = k_B T \xi / 2\Gamma$, and also gives a consistent stiffness result of $\Gamma = 1.6 \times 10^{-15}$ Jm^{-1}. As the stiffness is only present in the pre-factor of eq. (3.25), little extra information is in fact extracted from fitting to the exponential regions of figure 3.6a.

Next, these results are compared to those obtained from the power spectrum eq. (3.16). As outlined in section 3.3.2, the average interface profile is subtracted away from the interface

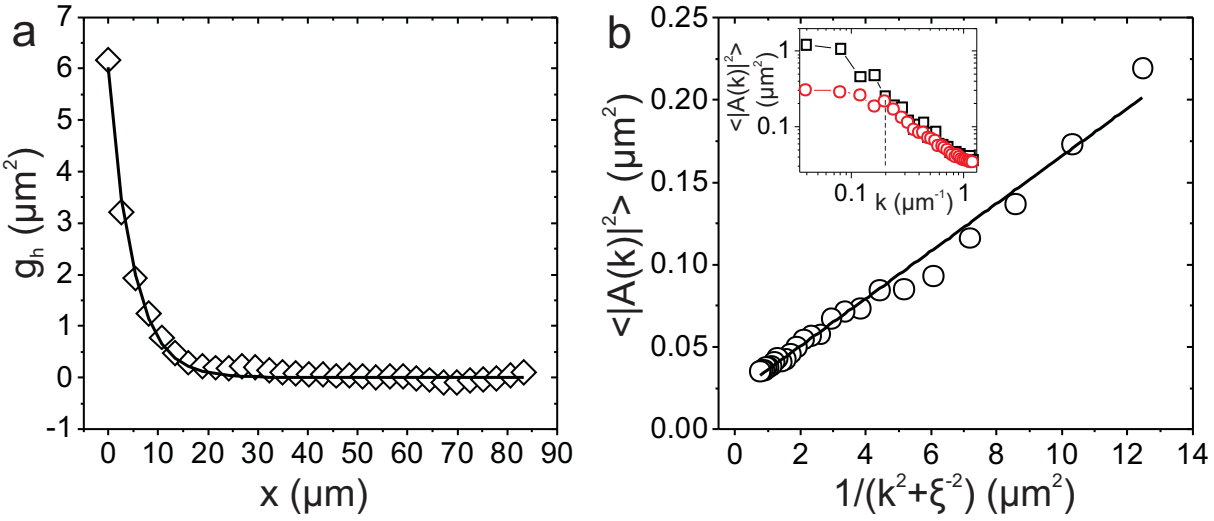

Figure 3.6: (a) The height-height correlation function $g_h(x)$: experimental data (symbols) and a fit (solid line) according to eq. (3.25). (b) The power spectrum displaying the wavevector dependence on the equilibrium static interface fluctuation spectrum, from which the stiffness is deduced using eq. (3.26). Inset: power spectrum with (○) and without (□) subtracting away the average interface profile.

profile as a function of time, removing the intrinsic structure. This process provides a natural long wavelength (and short wavevector) cut-off. As a result, an estimate for the correlation length ξ can be extracted simply by observation of the minimum wavevector not affected by this process (see inset in figure 3.6b, and shown for data with (○) and without (□) the average interface profile subtracted away, the dashed line corresponds to ~ 5 μm). This is in very good agreement with that found from the static correlation function in figure 3.6a. Likewise to the static case shown above, a correlation length ξ is introduced into the power spectrum to enable accurate mapping to the experimental data:

$$\langle |A(k)|^2 \rangle = \frac{k_B T}{L\Gamma(k^2 + \xi^{-2})}. \tag{3.26}$$

Next, to find $\langle |A(k)|^2 \rangle$, the interfacial profile is Fourier transformed for each time frame, the square modulus taken and then the result averaged over all frames. The power spectrum is plotted in figure 3.6b, showing a good fit to a straight line, and hence eq. (3.26). The interfacial stiffness is found from the gradient of figure 3.6b and results in $\Gamma = 3.5 \times 10^{-15}$ Jm^{-1} which compares well to the that computed from the real space methods.

The applicability of capillary wave theory to this system is demonstrated by the $1/k^2$ dependence in the power spectrum, shown in figure 3.6b. Previously, capillary wave theory expressions have been applied in the colloidal regime, where the particles are significantly smaller in size compared to the interface fluctuations, for example liquid-liquid interfaces [29]. The applicability of the theory to the coarser case of solid-solid interfaces, where the particles are of similar size to the fluctuations, confirms the relevance of the capillary fluctuation method, as used in atomic grain boundary simulations [30, 89].

3.4.2 Dynamic correlation functions

The dynamic correlation function of the grain boundary profile is simply given by:

$$g_h(t) = \langle h(t_0)h(t_0 + t)\rangle \tag{3.27}$$

and is shown in figure 3.7. As introduced in section 3.2.3, eq. (3.17) is the equivalent expression for $g_h(t)$ in Fourier space where $A(k)$ is the Fourier analogue of $h(x)$ [30]. This dynamic correlation function in Fourier space describes how the mean square amplitude of each Fourier mode decays exponentially with a decay constant $\tau = 1/M\Gamma k^2$. Importantly this dynamic correlation function expression (eq. (3.17)) depends on both the grain boundary stiffness Γ and the mobility M. Substituting the power spectrum eq. (3.16) into the dynamic Fourier space correlation function eq. (3.17) gives:

$$\langle A(k,0)A^*(k,t)\rangle = \frac{k_BT}{L\Gamma k^2}e^{-M\Gamma k^2 t}. \tag{3.28}$$

Fourier transforming leads to:

$$g_h(t) = \frac{k_BT}{L\Gamma}\sum_k \frac{1}{k^2}e^{-M\Gamma k^2 t}e^{ikx}. \tag{3.29}$$

The second exponent has no contribution as x can be set to 0 and therefore $e^{ikx} = 1$. Converting the sum to an integral over all values of k:

$$g_h(t) = \frac{k_BT}{L\Gamma}\frac{L}{2\pi}\int_{-k_{max}}^{k_{max}} \frac{1}{k^2}e^{-M\Gamma k^2 t}. \tag{3.30}$$

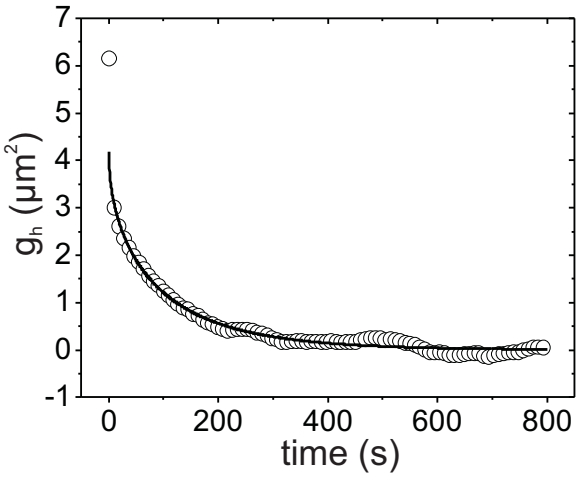

Figure 3.7: The dynamic correlation function $g_h(t)$: experimental data (symbols) and a fit (solid line) according to Equation (3.32).

The argument of the integral is even and the limits can be changed to $2\int_{k_{min}}^{k_{max}}$. Assuming that $k_{min} = 0$ to $k_{max} = \infty$ and introducing a correlation length ξ to prevent divergence at small wavevectors, yields the following expression:

$$g_h(t) = \frac{k_B T}{\pi\Gamma} \int_0^\infty \frac{1}{k^2 + \xi^{-2}} e^{-M\Gamma(k^2+\xi^{-2})t}\, dk. \tag{3.31}$$

Integrating produces a real space version of the Fourier space dynamic correlation function:

$$g_h(t) = \frac{k_B T \xi}{\Gamma} \mathrm{Erfc}\left(\frac{(\Gamma \mathrm{Mt})^{\frac{1}{2}}}{\xi}\right) \tag{3.32}$$

where Erfc(t) is the complimentary error function. Hence, in contrast to the static correlation function, the dynamic correlation function directly yields the grain boundary stiffness Γ *and* the mobility M. Consistently, the one point self correlation function also reduces to the mean square interface width, $k_B T\xi/2\Gamma$. The dynamic correlation function in figure 3.7 is described excellently by the real space dynamic correlation function, eq. (3.32), and from the fit, a grain boundary stiffness and mobility of 2.4×10^{-15} Jm^{-1} and 56 m^3/Js respectively, are extracted. Here, $\xi = 4.9 \times 10^{-6}$ m is used as found from $g_h(x)$. This value for the stiffness is in good agreement with the value obtained from the static correlation function and the power spectrum, though it is expected that the dynamic method is more accurate as the limiting factor is time rather than the interface length.

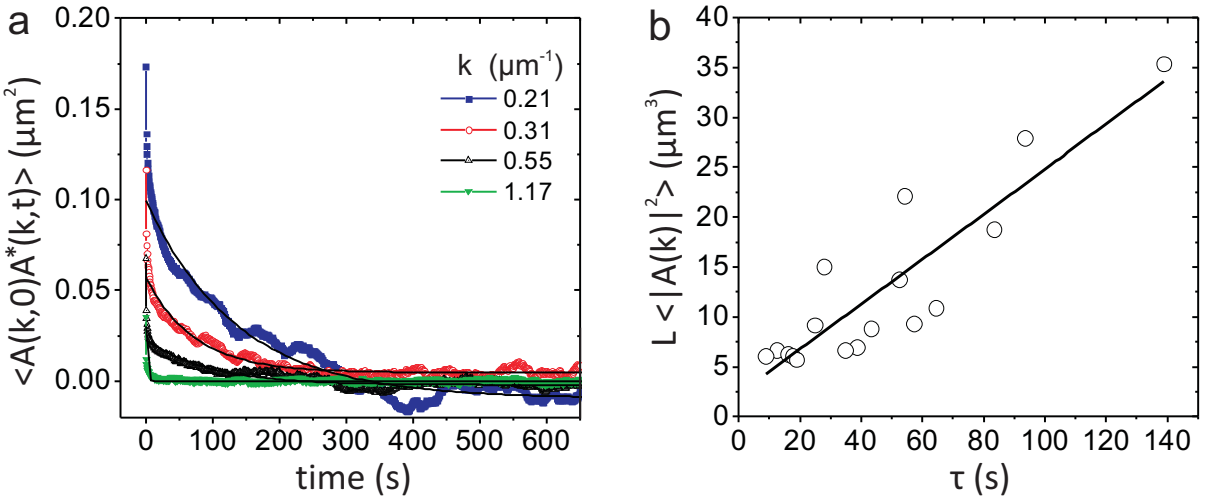

Figure 3.8: a) Decay of the amplitudes of the Fourier modes for a selection of wavevectors and shown with exponential fits. b) For each wavevector, $L\langle|A(k)|^2\rangle$ is shown versus the decay constant found from the time decay of the amplitude of that wavevector. The line represents a line of best fit.

Next, the interfacial properties are extracted from the dynamic correlations of the interfacial fluctuations, but in Fourier space. As a comparison to the real space method just shown, the reciprocal space dynamic correlation function, eq. (3.17), as described by Hoyt *et al.* [30] is directly used. A few examples of the decay of the Fourier modes, $\langle A(k,0)A^*(k,t)\rangle$ versus time, are given in figure 3.8a. Note that the fitting is poor at short times. It is thought this is maybe due to the sampling rate (2Hz) being significantly faster than the Brownian time ($\sim 11\ s$ (at infinite dilution)) creating greater correlation at short times. The decay constant, τ, in eq. (3.17) is given by $\tau = 1/M\Gamma k^2$, and substituting this into eq. (3.16) gives $L\langle|A(k)|^2\rangle = k_BTM\tau$ (eq. (3.18)). Subsequently, plotting $L\langle|A(k)|^2\rangle$ as a function of τ, see figure 3.8b, leads to a mobility of M = 55 m^3/Js, which compares excellently to the grain boundary mobility obtained from the dynamic height-height correlation function.

The grain boundary properties of the interfacial stiffness and mobility have been found, and show good agreement between the standard capillary fluctuation method and that from the real space derivations. Next, a different real space approach as developed by Trautt *et al.* [100] is tested, where the random walk performed by the average interface position is used to find the interfacial mobility.

3.4.3 Mobility from random walk analysis

Computer simulations by Trautt *et al.* [100] suggest that the grain boundary mobility can also be extracted using a fluctuation-dissipation based theorem in the limit of zero driving force. This approach is based on the average interface position performing a one-dimensional (1D) random walk. This is the interface-analog of the Stokes-Einstein relation for 1D diffusion of a Brownian particle, $\langle \bar{h}^2 \rangle = 2Dt$ where the diffusion constant D is directly proportional to the grain boundary mobility M. The dimensionality of their result is reduced for use with a 1D grain boundary. The resulting expression relates the average interface height $\bar{h} = \frac{1}{L}\int_0^L h(x,t)dx$ to a random walk via:

$$D = \frac{Mk_BT}{L}. \tag{3.33}$$

A typical trajectory of the average interface position, $\bar{h}$, for 200 s is shown in figure 3.9a with the corresponding probability distribution shown in figure 3.9b. The distribution displays a clear Gaussian shape confirming that the interface performs a 1D random walk and is therefore consistent with the method suggested in [100]. As shown in figure 3.9c, the grain boundary mobility is subsequently extracted from the time dependence of the mean square displacement. A grain boundary mobility of 70 $\mathrm{m^3Js^{-1}}$ is found from the gradient, which is again in very good agreement with the mobility obtained from the dynamic correlation function. Note that data for times smaller than the Brownian time ($\sim$ 11 s at infinite dilution) are not taken into account as the interface has had insufficient time to sample space.

3.4.4 Scaling comparisons for stiffness and mobility

To the author's knowledge, previous values for the grain boundary stiffness and mobility in colloidal crystals have not been reported, therefore the results are discussed in light of computer simulations of atomic grain boundaries in 2D and 3D crystals (i.e. quasi-1D and quasi-2D grain boundaries respectively). Typical stiffness results reported in 2D and 3D atomic simulations are on the order of 10^{-11} $\mathrm{Jm^{-1}}$ [90] and 1 $\mathrm{Jm^{-2}}$ [91] respectively. This is consistent with the stiffness scaling as $\sim k_BT/l_c$ in 2D and $\sim k_BT/l_c^2$ in 3D, where l_c is the characteristic length scale, which for atomic systems is $\sim$ 1 Å. Applying this scaling argument to a 2D colloidal

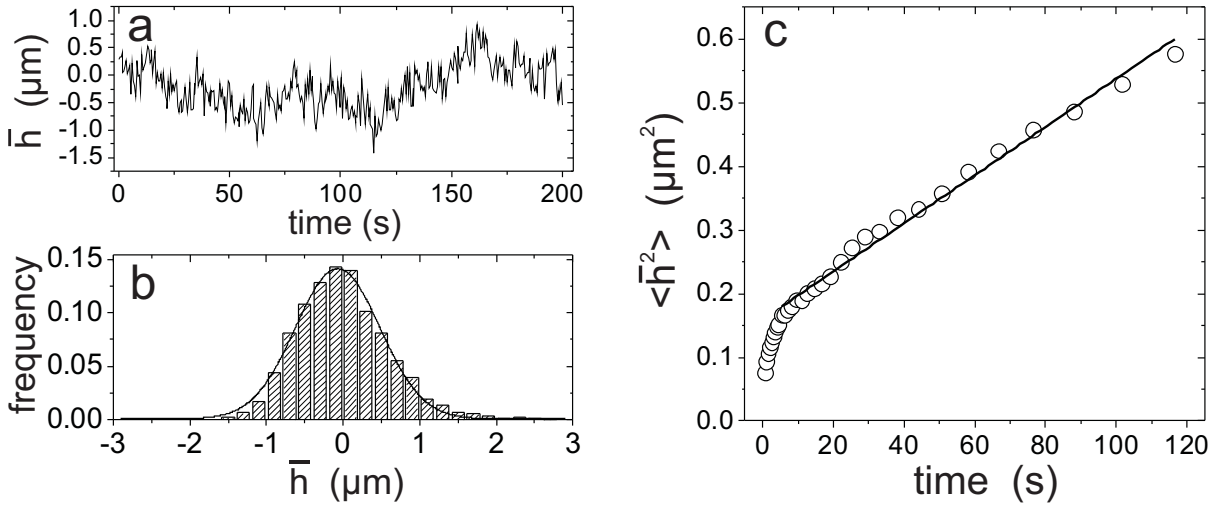

Figure 3.9: (a) The average interface position $\bar{h}$ as a function of time for a typical trajectory. (b) The probability distribution of $\bar{h}$ for $t = 200$ s with the solid line displaying a Gaussian fit. (c) The mean square displacement of $\bar{h}$ as a function of time with the solid line a linear fit to the data (for times larger than the Brownian time).

system, where $l_c \sim 1$ μm, a stiffness of $\sim 10^{-15}$ Jm^{-1} is expected, therefore demonstrating very good agreement with the results in this work. The mobility can then be addressed in a similar fashion, typical mobilities found in 3D atomic simulations (no 2D data available) range from $\sim 10^{-7}$ to 10^{-9} m^4/Js [91, 100]. A corresponding scaling relation for the mobility can be found as $M \sim l_c^4/(k_B T \cdot t_c)$, where t_c is the characteristic time scale which for atomic systems is ~ 1 ps. For a 2D system this expression reduces to $M \sim l_c^3/(k_B T t_c)$, so that in a 2D colloidal system, with a quasi-1D grain boundary, and $t_c \sim$ 10 s, a mobility of ~ 100 m^3/Js is expected. This is in excellent agreement with the mobility values found from the dynamic correlation functions and the random walk analysis. These simple scaling arguments show the robustness and the applicability of the real space analysis derived here, for the investigation of grain boundary fluctuations and the direct measurement of the grain boundary stiffness and mobility. In addition to proving useful for simulation studies, it is believed that this approach will also be useful in further studies using colloidal particles as a condensed matter model system to address the effect of impurities and confinement on the structure and mobility of grain boundaries.

3.5 Conclusions

The interfacial fluctuations of a quasi-1D grain boundary have been experimentally analysed in a 2D colloidal crystal. Expressions pertaining from capillary wave theory have been found to be applicable to these interfaces. The interfacial parameters, the mobility and stiffness, have been calculated from real space versions of the spatial and dynamical capillary wave theory expressions as used in the capillary fluctuation method. Good agreement is found between the methods derived here and from the dynamic and spatial correlation functions in Fourier space using the standard capillary fluctuation method. The prediction from simulation, that the mean square displacement of the average interface position can be used to find the mobility, has also been experimentally demonstrated and shows excellent agreement with all methods. Lastly, the grain boundary results found in these colloidal crystals display good agreement with those found from atomic grain boundary simulations using simple scaling arguments.

Acknowledgments

This work was done in collaboration with Dirk Aarts. Gert Aarts, Anna Maciolek and Klaus Mecke are thanked for useful discussions and Alice Thorneywork and Michael Juniper for critically reading the manuscript.

Chapter 4

Supercooled dynamics of grain boundary particles

ABSTRACT

The dynamics of particles within a grain boundary are investigated in a two-dimensional colloidal crystal. The mean square displacement of the grain boundary particles displays a clear plateau followed by an upswing indicative of cage breaking. The van Hove correlation functions and the non-Gaussian parameter show that the grain boundary particle dynamics are highly heterogeneous. Furthermore, clusters of cooperatively moving particles are identified and the time-dependence of the weight-averaged mean cluster size analysed. Good correlation between the behaviour of the mean square displacement, the time dependence of the non-Gaussian parameter and the cluster size, as also reported for various supercooled systems is found. These results provide experimental support for the similarity between particle dynamics in grain boundaries and those in supercooled liquids, as suggested by recent computer simulations.

This chapter is based on and reprinted with permission from [Thomas O. E. Skinner, Dirk G. A. L. Aarts and Roel P. A. Dullens, (2011), *Supercooled dynamics of grain-boundary particles in colloidal crystals*, J. Chem. Phys. 135, 124711].

4.1 Introduction

Grain boundaries (GBs) are the interface between adjacent crystals of differing orientation. Material microstructure is characterised by the network formed by GBs and other defects within a material, which then determine material properties including corrosion resistance, conductivity and strength [75, 77]. The development of most modern materials therefore requires precise control over the microstructural evolution during manufacture. As the structure and dynamics of GBs play an important role in microstructural development, GBs have been extensively studied in simulations [30,90–92,94,100,126] and experiments [87,97,117,120,132–134]. Studies of the dynamics of individual grain boundary particles however, have been mainly addressed using simulations [32,110]. Although the structure of grain boundaries in atomic systems has been studied in experiment [84,86,135], the time resolution needed to follow the movements of individual atoms is not yet attainable. The dynamics of particles at crystal boundaries is known to be important in several areas: the onset of melting [98], in the crystallisation of hard sphere glasses [136] and in the dynamics of dislocations [96,97].

It has been suggested many times, as early as about 1900, that grain boundaries may have an amorphous structure [31]. Due to the confinement of the atoms between the crystals, it was postulated that the atoms within a grain boundary may also exhibit dynamics akin to glass forming liquids [111,137–139]. Strong support for this hypothesis was more recently provided by molecular dynamics simulations [32,111] of high temperature grain boundaries, which indicated that the dynamics of GB particles are heterogeneous and show cooperative motion, which is also typically found in the particle dynamics of supercooled and glass-forming liquids [140–144]. Note that during publication of this work [145] a related study on grain boundary particle behaviour was published by Nagamanasa *et al.* [146], which came to similar conclusions.

High temperature grain boundary behaviour can have important consequences for properties relevant to materials processing, including GB strength [147] and mobility [148]. This underlines the importance of the need to understand the dynamics of particles in grain boundaries to ultimately enable greater microstructural control through grain boundary engineering [149]. Colloidal systems have proved to be very useful model systems with which to study GBs experimentally [23, 96, 98, 99, 134]. In this work, the dynamics of particles constituting GBs in

two-dimensional (2D) colloidal crystals are studied. The aim is to experimentally investigate in a colloidal system, the analogy between the particle dynamics in grain boundaries and those of supercooled liquids.

4.2 Background

4.2.1 Supercooled and glass forming systems

Amorphous solids are ubiquitous in our modern day lives. Synthetic polymers, for instance those used in fabrics and plastics, have at least a partially disordered structure. Window glass is made from amorphous silicon oxide, thin film semiconductors from amorphous silicon [150] and the developing area of amorphous metallic glasses, demonstrate superior strength to normal metals [151]. Structurally, amorphous solids, or glasses, lack the long range order of crystalline materials, have a structure similar to liquids, but exhibit arrested particle dynamics.

An amorphous solid can be made by first cooling a liquid below its melting point to form a supercooled liquid, which on further cooling, eventually forms an arrested amorphous structure [152]. Although at this temperature the crystal is the most thermodynamically stable state, the metastable supercooled liquid can be achieved with a sufficiently fast cooling rate and a lack of nucleation sites. A hallmark property of supercooled liquids is that as they are cooled, their viscosity increases and their particle dynamics slow down. This dynamical slowing down of the particle movements, arises from the temperature being lowered more quickly than the particles can positionally relax, leading to ever longer dynamical timescales. Eventually, the timescales of the particle rearrangements become so long that the system is said to be 'frozen' on the timescale of observation and is termed a glass.

The glass transition is not an equilibrium phase transition and is characterised by a smooth continued increase in particle relaxation times. Traditionally, the glass transition is defined as that when the viscosity reaches 10^{12} Pa s [154]. A typical plot of viscosity versus temperature for a supercooled liquid is shown in figure 4.1 [142,153] and illustrates the vast increases in viscosity, and consequently decreases in particle movement that occur as a liquid is cooled towards the glass transition. Figure 4.1 displays the two extremes of behaviour seen in glass forming systems,

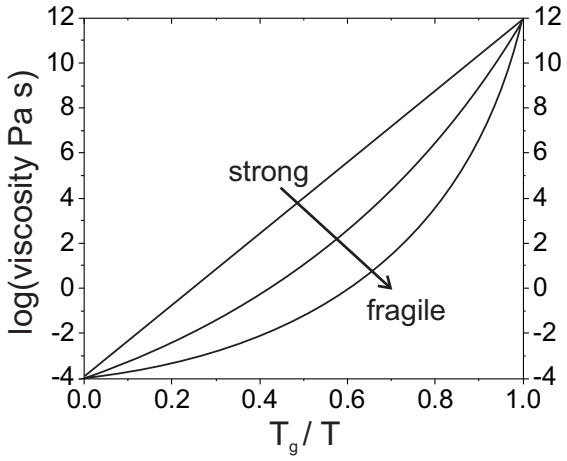

Figure 4.1: An 'Angell' plot displaying the vast increase in viscosity as a material is supercooled towards the glass transition, T_g, defined as 10^{12} Pa s [153].

those defined as strong and fragile glasses. The fragility characterises the large differences in the rate of dynamical slowing down that occur in different supercooled liquids, and has been shown to decrease on confinement [155].

In addition to an amorphous structure and slow dynamics, a characteristic feature of supercooled systems is the formation of cooperatively moving regions. These cooperative particle dynamics provide a pathway for structural relaxation and are found in many supercooled systems including atomic, colloidal glasses and granular matter systems [32,140–144,156,157]. The presence of cooperative particle movements within a system creates dynamical heterogeneities, areas with varying levels of movement and is signified by the presence of non-Gaussian particle dynamics. When confinement becomes similar or smaller in magnitude to the size of cooperatively rearranging regions, this is expected to have an effect on the glass transition temperature, and in turn on the fragility [154,155].

4.2.2 Grain boundary structure

It is nearly a 100 years since Rosenhain and Ewen [31] suggested their 'amorphous cement' theory, where 'the crystals of which metals are built up are held or 'cemented' together by an extremely thin layer of amorphous or non-crystalline material'. They even specified that the amorphous grain boundary region is 'identical with or closely analogous to the condition of a

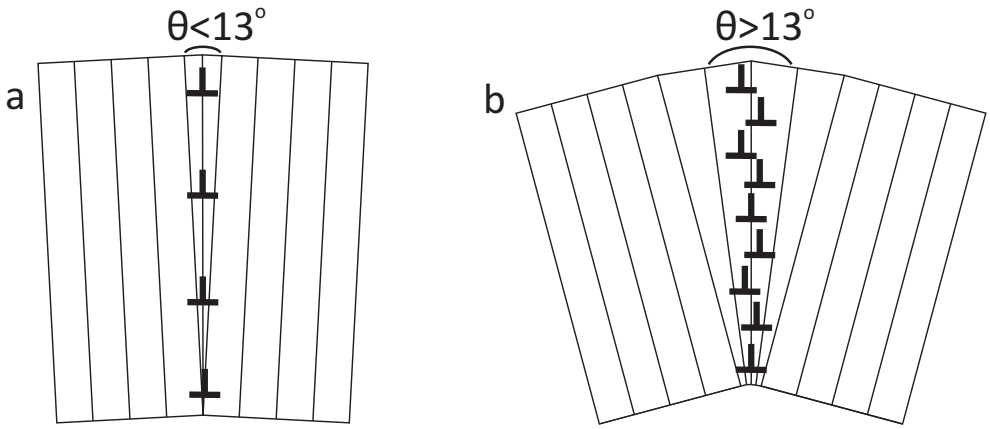

Figure 4.2: a) Schematic of a low angle grain boundary, typically with mis-orientation angle θ, less than 13°, and with discrete dislocations $\perp$. a) Schematic of a high angle grain boundary, typically with mis-orientation greater than 13°, and with a continuum of dislocations.

very greatly undercooled liquid'. This idea explained well their observed results on the strengths of iron at high temperatures, but there was no means to experimentally verify their theory at the atomic level. Their work nicely illustrates, even then without the knowledge of atomic structure, the interest in the similarities and differences between amorphous solids, glasses and grain boundaries.

In 1929, once the atomic structure of materials was known, Hargreaves and Hills [158] suggested a far more ordered grain boundary structure: where the atoms at the interface would still 'belong' to one crystal or the other, with a small amount of positional relaxation to fit. In contrast, in the Rosenhain and Ewen model, the disordered boundary region is not expected to be associated with either crystal, but serves as a region to accommodate the orientation transition. More recently, advances in microscopy have led to direct observation of grain boundary structure and interestingly, both the ordered and disordered forms have been reported [135, 159–161].

One may suggest that the predicted similarities between grain boundary particles and supercooled liquids can stem from simple packing frustration arguments. The organisation of particle positions in grain boundaries is a compromise between the enforced orientation of both adjacent crystals. Likewise to in supercooled liquids, grain boundary particles are confined and hindered by the structure around them [142]. Now follows a brief discussion on the types of grain boundaries and at what temperature, supercooled particle dynamics may appear. Note that as with chapter 3, grain boundaries are now referred to as being quasi-1D defects within a

2D lattice.

Grain boundaries can be separated into low and high angle interfaces, with the crossover in mis-orientation being typically $\sim 13^\circ$ [135,160,162]. Low angle grain boundaries have a small mis-orientation and can be described by a regularly spaced array of dislocations. A dislocation is a crystal defect which in 2D is a 5-fold and a 7-fold coordinated particle adjacent in the structure, see chapter 3, figure 3.1. Low angle grain boundaries are relatively well understood and their energy is accurately described by the Read-Shockley model [135]. Increasing the boundary mis-orientation decreases the dislocation spacing and eventually leads to overlapping dislocations. This signals the start of the high angle grain boundary regime, where extra dislocations are required to accommodate the greater orientation difference between the crystals. A schematic in figure 4.2 illustrates qualitatively the differences in defect distribution between low and high angle boundaries. In contrast to low angle boundaries, high angle grain boundaries generally possess a more irregular structure and are less well understood [149, 163–165].

High angle grain boundaries undergo a structural transition to a more amorphous state at high temperatures [138,166–168]. Understanding the behaviour of high angle grain boundaries at high temperatures is important as they are reported to play a rate limiting step in grain boundary migration during grain growth [138]. In contrast, low angle grain boundaries tend to remain crystalline for longer and their more ordered structures are less weakened by temperature [168]. The most likely grain boundaries in which to find supercooled particle dynamics are therefore those with high angles, low levels of symmetry and at high temperatures.

This chapter is organised as follows: in section 4.3.1, the colloidal model system and the experimental procedures are described. In 4.3.2, the data analysis procedures to characterise the single particle dynamics are outlined, followed by the method of locating the interface and how the GB particles are identified. Lastly, in section 4.4, the dynamical properties of the GB particles, cooperative motion and the cluster-size distribution are discussed.

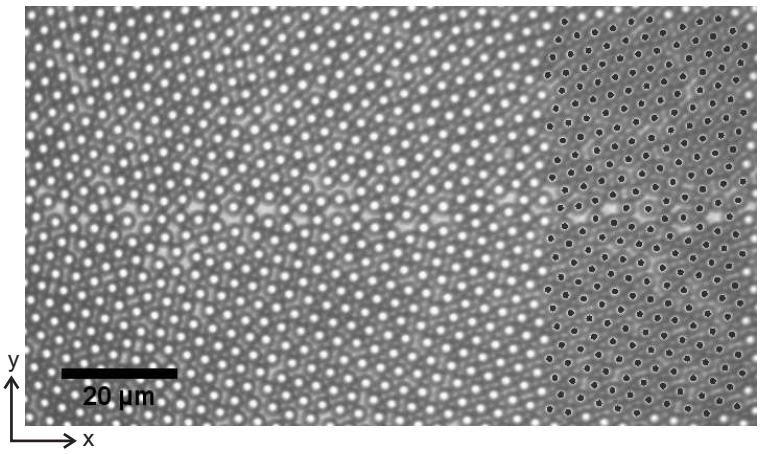

Figure 4.3: An image of part of the grain boundary showing the general disordered interface structure for this $\theta = 28^\circ$ grain boundary. The overlaid dots show the accurate particle tracking that is required.

4.3 Experimental methods and data analysis

4.3.1 Colloidal model system

A 2D colloidal crystal is formed from monodisperse 2.7 μm diameter (σ) melamine formaldehyde colloidal spheres (microParticles). The particles are dispersed in water and interact through a short-range screened Coulomb potential. The particles are contained in a 200 μm thick glass Hellma sample cell. The particles sediment and the number density is tuned such that a 2D crystal is formed. The system can be assumed to be fully 2D as out of the plane fluctuations of the particles are negligible, due to the particle size being much greater than the gravitational height (0.08 μm). Using optical video-microscopy, GBs of length $L \sim 180$ μm are recorded for 2500 s at 2 frames per second. Standard particle tracking software [74] is used to find the particle coordinates in time. The system has an area fraction of 70%. On the right hand side of figure 4.3 the recorded particle positions are shown plotted on top of the original image and demonstrate the high particle detection accuracy required.

The grain boundary shown in figure 4.3 is an asymmetrical high angle grain boundary (28°), which is also notable from the Voronoi construction in figure 4.4. Here, each polygon represents a particle, those with 6 nearest neighbours are shown colourless and those that are 5-fold or 7-fold coordinated are coloured light gray and dark gray respectively. The density of

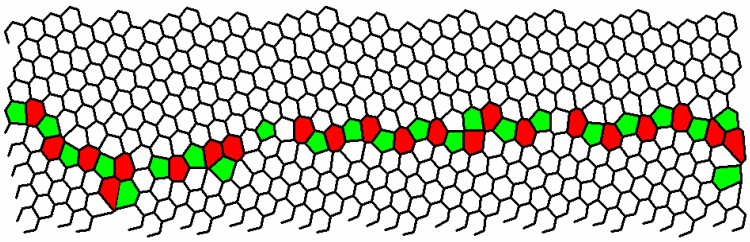

Figure 4.4: A Voronoi construction showing the location of the dislocations in the grain boundary. Each particle is displayed as a polygon with the number of sides and shade representing its coordination number. 6-fold particles are coloured white, and disclinations corresponding to particles with 5 and 7 nearest neighbours are coloured light gray and dark gray respectively.

these dislocations is high and continuous, as expected for a high angle grain boundary [135]. In a colloidal system, particle density can be interpreted as an inverse temperature scale. Hence, to model a high temperature grain boundary the crystal number density is set, as shown, to be sufficiently high for crystallisation, but low enough such that there is noticeable free volume in the interface, see figure 4.3.

4.3.2 Single particle dynamics

The statistical techniques that will be applied to the coordinates of the grain boundary particles in order to analyse their movement are introduced here. The dynamics of the single particles are characterised by the self part of the van Hove correlation function [169], $G_s(x,t)$, which is the probability distribution that a particle has traveled a distance x in a time interval t:

$$G_s(x,t) = \frac{1}{N}\left\langle \sum_{i=1}^{N} \delta\left(x + x_i(0) - x_i(t)\right)\right\rangle, \tag{4.1}$$

where N is the number of particles. The mobility of the particles can then be measured in terms of the mean-squared displacement, $\left\langle x^2 \right\rangle$, defined as the second moment of $G_s(x,t)$:

$$\left\langle x^2(t)\right\rangle = \sum_{i=1}^{N} x^2(t) G_s(x,t) = \frac{1}{N}\sum_{i=1}^{N}[x_i(t) - x_i(0)]^2. \tag{4.2}$$

The non-Gaussian character of the self part of the correlation function can be quantified by the non-Gaussian parameter, α_2, defined as follows:

$$\alpha_2(t) = \frac{\langle x^4(t) \rangle}{3 \langle x^2(t) \rangle^2} - 1, \tag{4.3}$$

where $\langle x^4 \rangle$ is the fourth moment of $G_s(x,t)$. The heterogeneity of the particle dynamics can therefore be found from the time development of α_2, which is zero for a Gaussian distribution, and $\alpha_2 > 0$ for non-Gaussian behaviour. Together, the van Hove correlation function, the mean square displacement and the non-Gaussian parameter form useful tools for characterising the degree, if any, of heterogeneous particle dynamics and cage breaking as is expected in glass forming systems.

4.3.3 Interface localisation

To identify the grain boundary particles, the coordinates of the interface must first be found using a local orientation parameter, $\Phi(i)$, assigned to each particle, i. First, the nearest neighbour, n_c, coordinates, $\vec{r_j}$, of every particle are found using a Delaunay triangulation. Next, the angle $\theta_j = \tan^{-1}[(y_j - y_i)/(x_j - x_i)]$, where $(-\pi \leq \theta_j \leq \pi)$, subtended from the central particle, i, to each of its nearest neighbours, j, is obtained. The local orientation parameter, $\Phi(i) = \frac{1}{n_c} \sum_j \theta_j$, yields a measure for the orientation of the particle. It corresponds to the orientation of the (1,1)-axis of the crystal – that the particle would be in – relative to the (horizontal) x-axis. Each frame is subsequently split into bins of approximately the particle diameter, perpendicular to the interface direction. The local orientation parameter is then plotted across the interface as shown inset in figure 4.5a. A tangent-hyperbolic fit to this profile gives the interface position for each bin. As a result, the interface height, $h_{exp}(x,t)$ is obtained for distance along the interface, x, for all times, t. The resulting interface position is plotted as a white solid line in figure 4.5a.

4.3.4 Identification of grain boundary particles

The identification of the particles which constitute the grain boundary is a subtle procedure. Grain boundaries are dynamic, with some particles frequently changing identity between crystal and grain boundary. In addition, due to fluctuations in the local orientation, the amount of

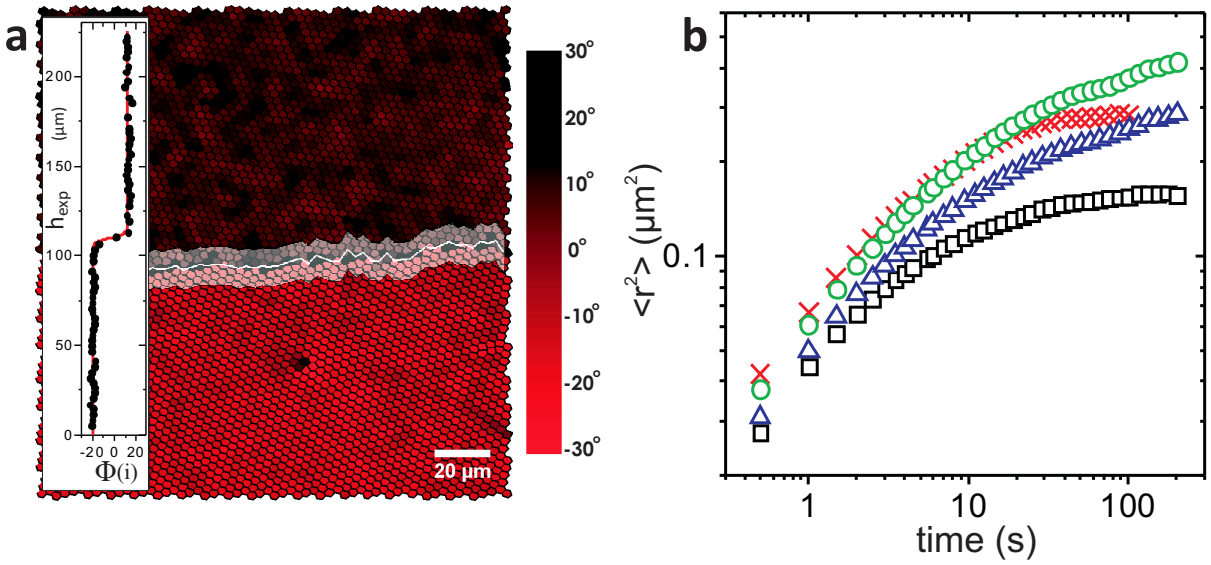

Figure 4.5: a) The 2D crystal containing the grain boundary plotted as an orientational Voronoi construction, where the color of each cell represents the local orientation parameter of the corresponding particle, as indicated by the color scale. The shaded band around the interface (solid line) represents the distance criterion for locating the GB particles (see 4.3.4). The inset on the left shows a typical tangent-hyperbolic fit to the local orientation parameter profile for a single bin. (b) The mean square displacement for the selection $n_c \neq 6$ ($\times$), for $5\sigma_{n_c}$ ($\circ$), for 12σ ($\triangle$) and for the bulk crystal particles ($\square$).

particle movement is variable along the interface, see figure 4.6. To locate the interface particles a combination of the following two criteria are applied:

1. a particle's coordination number, n_c;
2. a distance criterion from the local interface position, $h_{exp}(x,t)$.

(1) To a good approximation, all particles near the interface with coordination number not equal to 6 are GB particles. The mean square displacement of this selection of particles is shown as crosses in figure 4.5b. Only the short time behaviour is available, as few of this particle subset have $n_c \neq 6$ for a significant length of time.

(2) The distance criterion corresponds to a band centered around the interface (shaded band in figure 4.5a). The width of the band is tuned, in conjunction with a filter to cut out particles with $n_c = 6$ for the whole time series, to closely match the short time behaviour of the MSD,

Figure 4.6: A plot of a selection of the grain boundary particle coordinates (one pixel each) plotted over a period of 2500 s. Different regions displaying varying degrees of particle mobility are visible.

to that of the $n_c \neq 6$ subset (from the first criterion). The resultant selection of GB particles is shown as circles in the MSD in figure 4.5b. This corresponds to selecting all the particles within a 5σ band centered around the interface, who do not have $n_c = 6$ for the whole time series. A typical plot of some of the GB particles positions over a period of 2500 s is shown in figure 4.6, where each particle position is represented as one pixel per time frame. If the distance criterion is widened, for example to 12σ (triangles in figure 4.5b), too many crystalline particles are included. On further widening of the band, the MSD gradually reduces towards that of the bulk crystal (squares in figure 4.5b).

4.4 Results and discussion

4.4.1 Grain boundary particle dynamics

The analysis techniques outlined in section 4.3.2 are now used to investigate the dynamics of the GB particles. First, the mean square displacement of the particles constituting the grain boundary and the bulk crystal are plotted in figure 4.7. The mean square displacements all reach a plateau after $\sim$ 200 s, but the magnitude of the GB particles' plateau is significantly greater than that of the bulk crystal. This observation is consistent with the more disordered and fluid-like nature of the grain boundary as compared to the bulk crystal [31, 137, 138, 170, 171]. The enhanced mobility of the GB particles with respect to the bulk has interestingly, been suggested to be important for crystallisation in a hard sphere glass [136, 172]. Decomposing the displacement into x and y, i.e. parallel and perpendicular to the GB respectively, shows clearly that $\langle x^2 \rangle > \langle y^2 \rangle$. In this particular grain boundary, particle movement along the interface is therefore substantially easier than perpendicular to it. This observation however, is expected

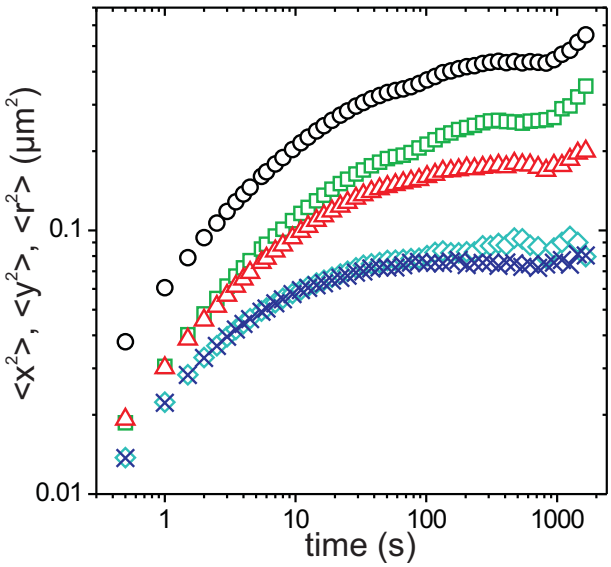

Figure 4.7: Mean square displacements for the grain boundary particles $\langle r^2 \rangle$ ($\circ$), decomposed into, along the boundary, $\langle x^2 \rangle$ ($\square$), and perpendicular to it, $\langle y^2 \rangle$ ($\triangle$), and for the bulk crystal in the x ($\times$) and y ($\diamond$) directions.

to sensitively depend on the structural details of the grain boundary [77, 173]. As expected $\langle x^2 \rangle \simeq \langle y^2 \rangle$ for the particles in the bulk crystals.

The increase in the mean square displacement of the GB particles at long times shows the onset of cage breaking and rearrangement, unlike as expected, in the mean square displacement for the crystalline particles. This behaviour is indicative of that expected from a supercooled liquid and is consistent with that observed in [32,146]. The onset of cage breaking is also significantly more pronounced along the grain boundary than perpendicular to it. As already noted, the structural details of the boundary are expected to be of importance here, but the possibility that this observation is reminiscent of the 1D nature of the grain boundary has been considered. Due to the motion of the particles being more confined in a direction perpendicular to the grain boundary. Furthermore, in slightly wider grain boundaries, the caging of the GB particle dynamics generally appear less pronounced indicating the subtle effect the dimensionality has on the particle dynamics.

Next, the dynamics of the GB particles are analysed to investigate the presence of any dynamical heterogeneities by computing the self part of the van Hove correlation function, $G_s(x,t)$, see eq. (4.1). The $G_s(x,t)$ is shown in figure 4.8a for the motion along (x) and per-

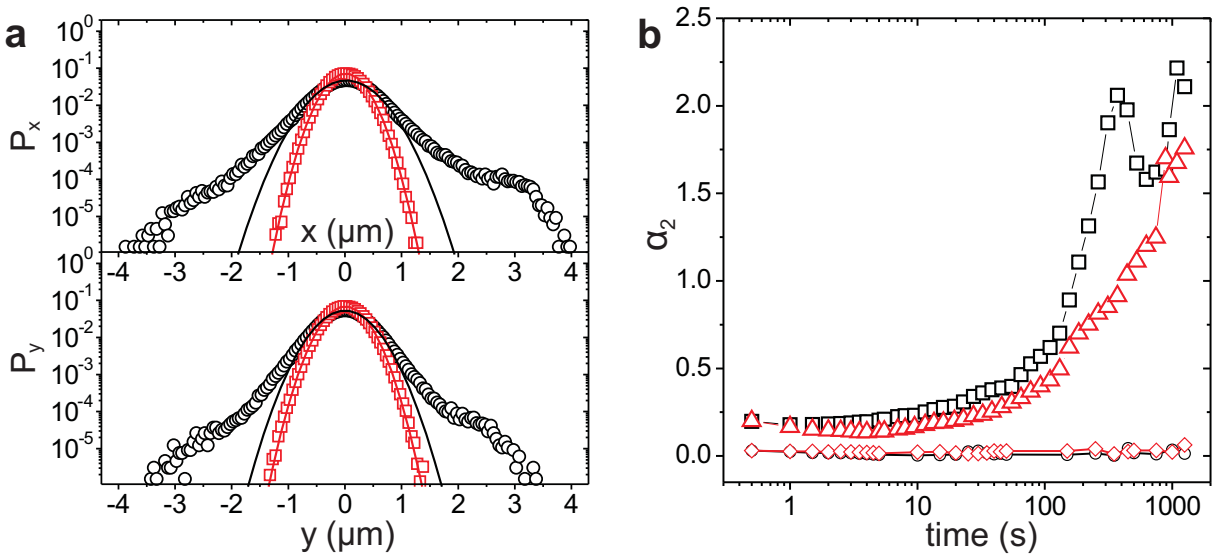

Figure 4.8: a) Self part of the van Hove correlation function along (x) and perpendicular (y) to the grain boundary for the grain boundary particles ($\circ$) and the bulk crystalline particles ($\square$), for $t = 200$ s. Gaussian fits to the data are shown as solid lines. (b) Non-Gaussian parameters for the movement along the grain boundary (x, $\square$), perpendicular to it (y, $\triangle$) and for the bulk crystalline particles in x ($\circ$) and y ($\diamond$).

pendicular (y) to the grain boundary. The distributions for the bulk crystalline particles are shown for comparison, and as expected they display Gaussian distributions. In contrast, the GB particles clearly exhibit non-Gaussian particle distributions in both directions. This behaviour is indicative of heterogeneous particle dynamics and is similar to that found in supercooled liquids [140, 141, 143, 144].

The time dependence of the non-Gaussian parameter (α_2) is shown in figure 4.8b. Whilst $\alpha_2 \sim 0$ for the bulk crystalline particles, α_2 for the GB particles is clearly non-zero. The α_2 starts very small at short times, characteristic of diffusive motion, before at longer times (~ 200 s) the particles encounter their cage of surrounding particles and α_2 increases significantly as particles become caged to differing extents. This timing coincides with the plateau formed in the mean square displacement as the particles are slowed by their cages. The mean square displacement increases again at long times which signifies the end of the cage trapping regime, and which should coincide with a decrease in α_2 [141, 174]. This is observed to some extent for motion along the boundary, but less so perpendicular to it. It is expected that this is largely due to the

more prominent increase of the mean square displacement in the x direction and the decrease in statistical accuracy at very long times. The heterogeneous dynamics can be observed more visually in a plot of the GB particle positions over time as shown earlier in figure 4.6.

4.4.2 Cooperative motion and cluster size distributions

The presence of any cooperative particle motion in the grain boundary particle dynamics is now investigated. Cooperative particle motion is a very characteristic feature of supercooled liquids [140–144, 152] and has also been observed in the GB simulations [32, 110]. In order to find groups of particles that move in a concerted fashion, particles are sorted into clusters based on their relative movements between times t_0 and t. The same methodology as Donati *et al.* [140] is used where two adjacent particles, i and j, are classified within the same cluster if:

$$\min[\ |\vec{r_i}(t) - \vec{r_j}(t_0)|,\ |\vec{r_i}(t_0) - \vec{r_j}(t)|\ ]\ <\ d \tag{4.4}$$

where $d = 0.9\ \sigma$. Note that here, the d value is set greater than that used in [140]. This is due to the inherently slow dynamics present in a 2D system and the highly confined nature of the GB particles.

An example of a typical cluster of moving particles within the grain boundary is illustrated in figure 4.9, corresponding to $t = 200$ s. In this example, the motion is shown relative to the particle size to give a clear representation of the dynamics. The formation of these string-like clusters in the grain boundary is very similar behaviour to that expected in supercooled liquids [140–144] and indicates the presence of cooperative particle motion in the GB. This cluster also highlights the pronounced 1D character of most motion in the GB. The majority of clusters form along the grain boundary, consistent with the increased MSD in the x direction. This 1D character is noticeably more pronounced than that observed in the 'planar' grain boundaries of 3D systems [32, 146]. The string-like clusters formed are also very transient, as the direction of particle motion changes frequently. Therefore, most particles do not traverse far and as a consequence, any 'backflow' motion is limited, but accommodated by the typical grain boundary width of $\sim 3\sigma$ where required [175].

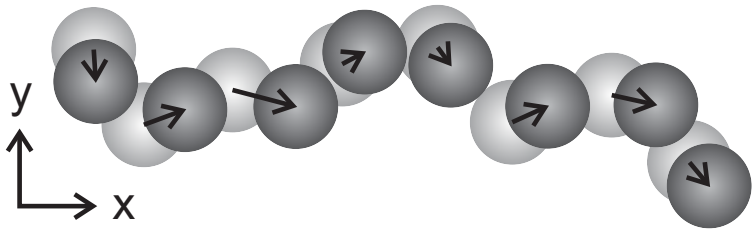

Figure 4.9: A schematic of a typical cluster of moving particles in the grain boundary and illustrating the cooperative nature of the particle motion. The light spheres are the particle positions at $t_0 = 0$ s and the dark spheres are the positions at $t = 200$ s. The movement is shown relative to the particle size.

To further analyse the particle clusters formed and any cooperative motion, the distribution of cluster sizes is determined. The cluster size distribution is shown in the log-lin plot in figure 4.10a where $P(n)$ is the probability of finding a cluster containing n grain boundary particles. The nearly straight line distributions in figure 4.10a indicate that the cluster size distributions are approximately exponential, as is also observed in supercooled and glass-forming systems [32,174,176]. The cluster size distributions are also highly dependent on the observation time window, t. To quantify this time dependence, the weight-averaged mean cluster size, S_w, is calculated as a function of t [174, 176]:

$$S_w(t) = \frac{\langle n^2(t) \rangle}{\langle n(t) \rangle} = \frac{\sum n^2(t) P(n(t))}{\sum n(t) P(n(t))}. \tag{4.5}$$

Any clusters formed at short times are random due to the particle motion still being uncorrelated. Therefore the contribution from random clusters is taken out by normalizing S_w with respect to the average cluster size at the shortest time S_0: $S \equiv S_w/S_0$ [174, 176]. The resulting average cluster size, S, is shown as a function of time in figure 4.10b. A rapid increase is observed as the the time window increases, reaching a maximum at ~ 200 s, before slowly the average cluster size decreases again at long times.

The time development of the increase in the average cluster size coincides with the formation of the plateau in the mean square displacement, see figure 4.7. At these times the particles are encountering the cages formed by their nearest neighbours. This causes the particle motion to start to become more non-Gaussian and cooperative motion to become apparent. The maximum average cluster size is roughly observed when the mean square displacement has fully

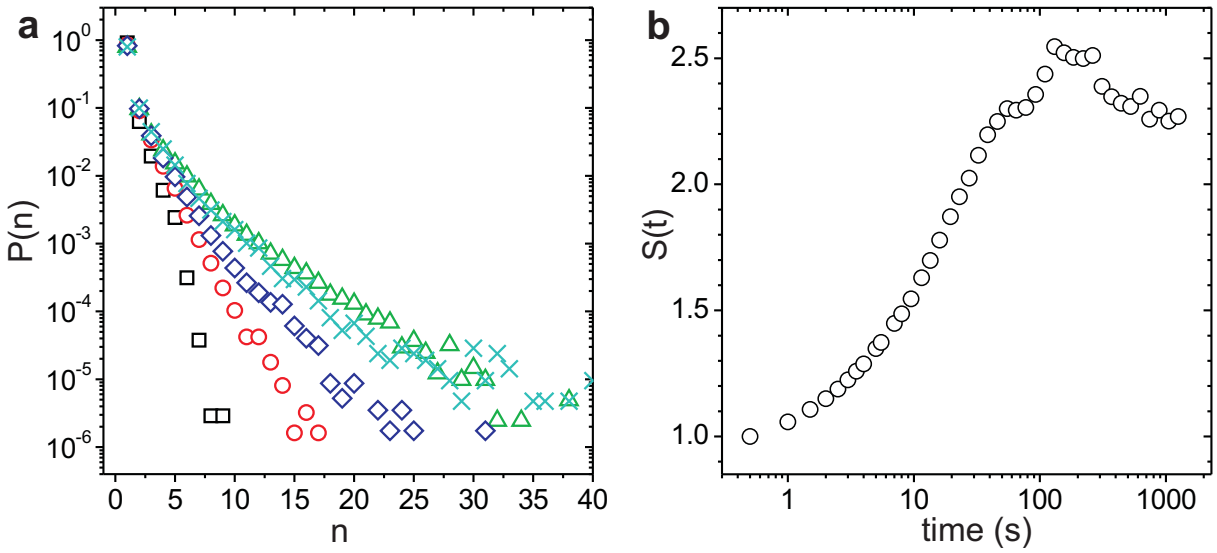

Figure 4.10: a) Probability distribution, $P(n)$, of cluster sizes, n, for different times: $t = 1$ s (□), $t = 5$ s (○), $t = 10$ s (◇), $t = 220$ s (△) and $t = 1050$ s (×). (b) The normalized weight-averaged mean cluster size, S, as a function of the observation time window, t.

plateaued, and the particles are 'rattling in their cages'. The non-Gaussian parameter, α_2, in particular corresponding to motion along the grain boundary, also reaches a maximum at this time. This is consistent with the more pronounced cooperative motion and heterogeneous particle dynamics in this direction. At longer times, cage breaking and cage rearrangements start to occur, evident from the increase of the mean square displacement at long times, and bringing about the return to diffusive motion of the particles. As diffusive motion is random in nature, this motion leads to the observed decrease of the average cluster size and the non-Gaussian parameter.

The observed correlation between the mean square displacement, non-Gaussian parameter and mean cluster size has also been observed for a range of glass forming systems, for instance polymer melts [176], network glass formers [177] and colloidal glasses [141]. Hence, this provides very good support for the analogy between the dynamics of grain boundary particles and supercooled liquids, as suggested by simulation [32] and experiment [146]. As a final note, it is worth pointing out that the grain boundary particles in this 2D experimental system have a reduced dimensionality compared to the planar grain boundaries in [32, 146]. As confinement is known to have a large impact on the particle dynamics of systems [178, 179], preliminary observations

suggest that the cluster sizes decrease for GBs of smaller width. These experimental results may also be relevant for supercooled systems in other highly confining structures such as porous media [34].

4.5 Conclusion

The dynamics of particles constituting grain boundaries in a 2D colloidal crystal has been quantitatively analysed in real space and time using optical video-microscopy. The mean square displacement of the grain boundary particles shows a pronounced plateau at intermediate times followed by a subsequent increase at longer times. This is indicative of the supercooled nature of the grain boundary particle dynamics. The mobility is found to be higher along the boundary than perpendicular to it, although this is expected to be sensitive to the microscopic details of the grain boundary structure, it is consistent with the highly confined 1D nature of the grain boundary. The grain boundary particle dynamics are highly heterogeneous, as is evident from the non-Gaussian shape of the self part of the van Hove correlation function, and from the time dependence of the non-Gaussian parameter. Furthermore, cooperative motion has been observed and analysed in terms of the time dependence of the weight averaged mean cluster size. The observed correlation between the mean square displacement, the non-Gaussian parameter and the mean cluster size is very similar to that found in supercooled systems [140–144,174,176,177]. This study therefore provides direct experimental evidence for the similarity between the nature of the particle dynamics in grain boundaries and supercooled liquids as suggested by computer simulations [32, 110].

Acknowledgments

This work was done in collaboration with Dirk Aarts. Paddy Royall is thanked for useful discussions. Alice Thorneywork and Michael Juniper are thanked for critically reading the manuscript.

Chapter 5

Structure and dynamics in pentagonal confinement

ABSTRACT

The structural and dynamical behaviour of colloidal particles confined within a two-dimensional (2D) pentagonal environment is studied. The confinement is created using an optical tweezer to fix the positions of a pentagonal array of colloidal particles. Particles within the pentagonal area are free to move. All the particles are super-paramagnetic and their interaction potential is controlled by an external magnetic field. The behaviour of the confined particles and the packing frustration created is studied via two contrasting pathways. In the first section, a system consisting of 16 confined particles is melted from a crystalline to a confined liquid-like state as the external magnetic field is reduced. In the second section, the magnetic field is kept constant and the number of confined particles sequentially increased from 10 to 21. Re-entrant orientational ordering and dynamically frustrated states occur as the number of confined particles is increased.

5.1 Introduction

Crystallisation in confinement is a widespread phenomenon, occurring in the natural processes of biomineralisation [180] and freeze-thaw weathering [181], and in technological applications including the fabrication of nanoparticles [182] and drug delivery [183]. The development and control of these processes is dependent on understanding melting and crystallisation in these confined volumes. Under extreme confinement, liquids can also appear to form rigid glass-like structures above their melting temperatures, as such, this has far reaching consequences for lubrication [184–186], hydrodynamics near walls [12] and lab-on-a-chip applications [187].

The effect of confinement on phase behaviour has been widely studied in small pores [188–190] and in planar confinement [191]. Crystallisation is well known to differ from the bulk, especially when the confinement is of comparable size to the particles, when excluded volume effects become important [192–194]. The glass transition temperature has been seen to both increase and decrease in confinement [195, 196], with the increases in viscosity and decreases in particle motion occurring when boundary layering effects become important, the particle movement restricted and the packing frustrated. In particular, crystallisation has been shown to be very different in 2D systems, including in shaped confinement [197].

Colloidal systems are often used as model systems to investigate phase transitions [98, 99, 198, 199]. The control imparted from manipulation of their chemical and physical characteristics allows the inter-particle potential to vary from hard sphere-like [16] through to a long range repulsion [199]. Crystallisation and melting has been widely studied in colloidal systems, both in 3D [98] and 2D [200–202]. Also, the effect of circular confinement on crystallisation has been studied [197], which showed that shell rotations can cause re-entrant freezing behaviour. In this chapter, the structure and dynamics of particles confined within a pentagonal environment is studied. The incommensurate symmetry and high level of confinement makes this system truly frustrated. The packing of pentagons in a circle has been analysed due to the similarities with granular systems [203], but to the author's knowledge there has been no study on the packing and dynamics of circular particles confined in a pentagon.

5.2 Background

5.2.1 Colloidal systems in 2D confinement

Melting in two dimensional (2D) systems occurs via a dramatically different pathway to that of the bulk [204] and occurs via a two-step process described by KTHNY theory [101–103]. This is a defect mediated two-step melting transition comprising of dislocation and disclination pair unbinding processes. In 2D systems, a dislocation consists of two disclinations, one a 5-fold and one a 7-fold coordinated particle adjacent to each other in a crystal lattice, see figure 3.1 in chapter 3. Melting in a 2D crystal starts with the unbinding of dislocation pairs, disrupting the crystalline translational order. This forms an intermediate phase termed the hexatic, characterised by short range translational and quasi-long range orientational order. A further decrease in temperature results in a total loss of long range translational and orientational order via dislocations unbinding into their constituent disclinations.

Another factor that can effect phase transitions under confinement is symmetry. Particles contained within 2D circular and square confinements have shown that particle mobility and packing arrangements are heavily affected by the imposed symmetry [197, 205, 206]. In circular confinement, a greater amount of angular with respect to radial mobility is observed, resulting in shell rotation [197, 207]. In contrast, in square confinement, the large difference to the preferred hexagonal symmetry induces packing frustration, small particle mobilities and leads to degenerate structures forming [205].

Interestingly, colloidal particles confined in 2D circular environment have been shown to exhibit a re-entrant ordering process during melting [197]. The system consists of superparamagnetic colloidal particles in a 2D plane inside a circular non-magnetic cavity. An external magnetic field controls the inter-particle repulsion and the particles subsequently arrange in a shell-like structure in the cavity. Upon decreasing the field, the system initially starts the melting process via a loss of angular order between the shells. Further reduction of the magnetic field however, sees the angular order restored, before finally the whole system melts. The intermediate inter-shell rotation phase is mediated by the confinement creating a lower energy barrier to rotation as compared to radial deviations.

When the symmetry of the confinement is incommensurate to the preferred hexagonal ordering of the particles, interesting packing frustration results. The phenomena of pentagonal symmetry has long intrigued people due to its incompatibility with long range order and space filling [208]. One method to induce large packing frustration, is to study how phase behaviour is affected by pentagonal confinement.

5.2.2 Why study 5-fold symmetric structures?

In nature, 5-fold symmetry is seen as unremarkable and fairly common, examples include starfish, molecules, fruits and many flowers [208, 209]. In contrast, in the areas of mathematics and physics, it is seen as mysterious and troublesome; the symmetry is regarded as forbidden as 5-fold structures cannot tile the plane. Kepler, Dürer and Penrose each found solutions to this problem by tessellating pairs of shapes to make aperiodic patterns; these contained 5-fold symmetry and were able to fill 2D space [210, 211]. Pre the early 1980s, it was believed that ordered crystals were always periodic and that orientational order was limited to 2,3,4 and 6 fold rotational symmetries. However, in 1982 Shechtman discovered a 5-fold symmetric aperiodic structure in a manganese and aluminium alloy [212]. Shortly afterwards Levine and Steinhardt [213] realised that 'Penrose tiling' could be used to explain these 'impossible crystals', which lack translational symmetry, and thus coined the term 'quasicrystal'. The realisation of the existence of aperiodic crystal structures earned Shechtman the 2011 Nobel prize for Chemistry [214].

Besides quasicrystals [209, 215], the younger field of nano-technology has also reported a relative abundance of 5-fold symmetric structures [216, 217]. Many nanoparticles and nanorods that have been synthesised with pentagonal cross-section [216]. Here, the presence of the pentagonal symmetry is often integral to the structure, for instance in creating anisotropic growth for nano-wires [218–220]. An illustration of a nanorod with pentagonal cross section is shown in figure 5.1. Notice the five symmetric grain boundaries and the central 5-fold disclination at the centre. Many unrelated systems have observed the presence of 5-fold symmetric structures, but due to the unfamiliarity, the mere observation of pentagonal structures still provokes intrigue [221–224].

This chapter is organised as follows. Firstly, the colloidal model system and the exper-

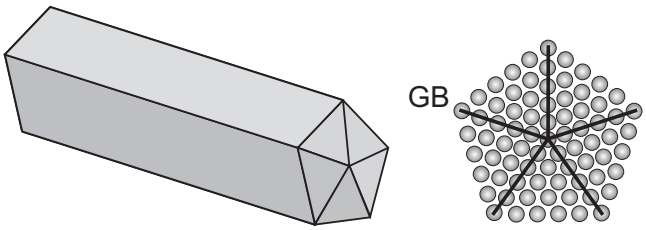

Figure 5.1: Left, a schematic of a nanorod, showing 5 symmetric grain boundaries. Right, a front on (2D) view showing the central 5-fold disclination.

imental techniques are introduced. Next, in section 5.4.1 a pentagonally confined 16 particle system is studied. This number of confined particles, creates a system commensurate with the confining geometry. The effective particle size is reduced via an external magnetic field to induce structural melting and disorder. Lastly, in section 5.4.2, the structural and dynamical changes occurring as the number of confined particles is sequentially increased from 10 to 21 are observed, while keeping the magnetic field constant.

5.3 Experimental methods and data analysis

5.3.1 Colloidal model system

The system consists of monodisperse super-paramagnetic polystyrene colloidal spheres (Dynabeads) 2.8 μm in diameter (σ) dispersed in water. As introduced in chapter 2 section 2.1.5, the colloidal particles contain uniformly dispersed iron oxide nanoparticles which make the colloidal particles super-paramagnetic. In the absence of an external magnetic field, B, the super-paramagnetic colloidal particles have zero magnetic dipole moment, but gain a dipole moment in the direction of an applied field, leading to a repulsive pair potential. The colloidal particle interaction strength is characterised by the dimensionless interaction parameter Γ, which is defined as the ratio between the magnetically induced interaction potential, E_{mag}, and thermal energy k_BT [204]:

$$\Gamma = \frac{E_{mag}}{k_BT} = \frac{\mu_0}{4\pi}\frac{\chi^2 B^2 (\pi\rho)^{3/2}}{k_BT} \tag{5.1}$$

where ρ is the particle number density, χ the particle magnetic susceptibility and μ_0 the permeability of free space. This magnetic field induced control over the particle interaction potential and state of the system acts as a from of temperature gauge, equivalent to $1/\Gamma$.

The colloidal particle system is contained within a 200 μm thick, glass Hellma sample cell. The particles sediment and as the particle size is much greater than the gravitational height, the out-of-plane fluctuations of the particles are negligible. A very dilute sample is created where there are typically 5 particles per 100 μm^2 of sample cell.

5.3.2 Optical tweezing, magnetic fields and video microscopy

The sample is placed in the optical tweezer and microscopy set-up, which is described in chapter 2, section 2.2.5. As a brief recap, an optical tweezer is a highly focused laser beam that can trap particles and move them. One laser beam is time-shared between many points to create many 'individual' traps using an acousto-optic deflector. The laser beam can move between these points sufficiently quickly that, on the time-scale of the Brownian movements of the colloidal particles, each optical trap is seen as discrete.

Within the sample cell the required number of colloidal particles, typically 31, are isolated using the optical tweezer to a selected area of the cell, leaving a region, $\sim$ 100 μm in all directions free from particles. The pentagonal confinement is created by tweezing an array of particles to produce a pentagon shape as shown in figure 5.2a. These traps then remain on for the entirety of the experiment to retain the pentagonal environment. An additional trap is used to add the remaining required number of particles into the confined zone, before being switched off.

The particle spacing of the pentagonally shaped confinement is set to 10 μm. This enforced gap leads to a lower bound on the magnetic field used of 1 mT before particles escape. To reduce the effect of the optical tweezer on the free particles inside the pentagon, the optical tweezer trap strength is set to the minimum value that can sustain the pentagonal environment (time-shared 20 mW). The magnetic field is increased to the required value at a rate of 0.001 mTs^{-1} to allow the system to equilibrate. Using optical video-microscopy (PixeLINK CMOS camera) image stacks are recorded at 1 Hz for 4000 s. Standard particle tracking software [74] is used to find the colloidal particle coordinates in time, as is described in chapter 2, section 2.12.

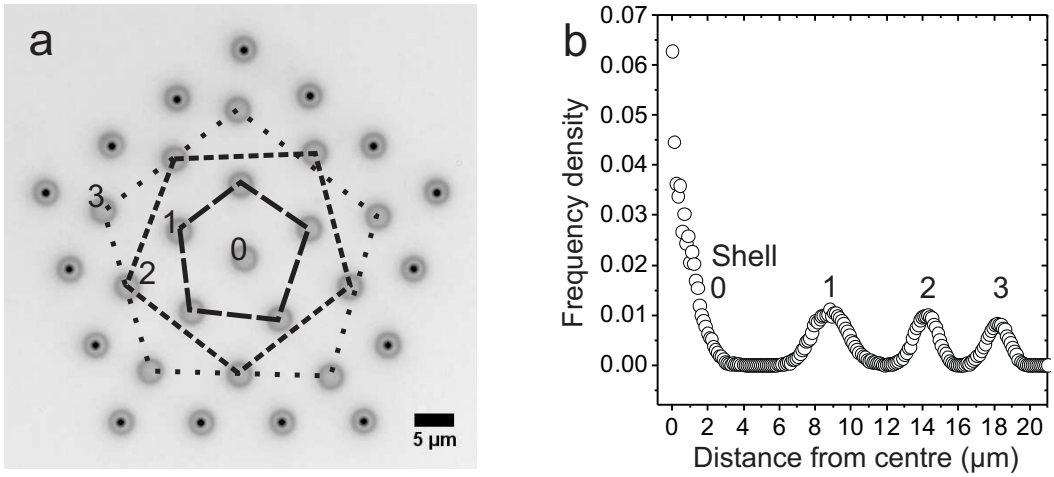

Figure 5.2: a) 31 colloidal particles of which 16 are confined within a pentagon created by the other 15, fixed into position (black dots overlaid) using an optical tweezer. The shells are denoted 3, 2, 1 and 0, where 0 is the central particle. Gravity and magnetic field are perpendicular to the plane. b) Radially averaged histogram of the particle positions measured from the pentagon centre over a period of an hour for the system to the left. The shell structure contains a central particle and 5 particles in each of the shells 1, 2 and 3.

5.3.3 Characterising the particle environments

A shell based terminology is introduced to characterise the particle positions. The positions of 16 confined colloidal particles in the pentagonal environment are shown in figure 5.2a, with the radial density distributions of the same system averaged over the course of an hour shown in figure 5.2b. The particles in figure 5.2a which are optically tweezed to create the pentagon, are shown with dots overlaid. The positions highlighted in figure 5.2a, and the corresponding pentagons they encompass, displays the four distinct shells within the pentagon as is evident from the peaks in the radial histogram in figure 5.2b. Hence, a central particle and three surrounding pentagons, denoted shells 0, 1, 2 and 3 are identified. This packing configuration is schematically denoted as a 5,5,5,1 shell structure, i.e. three shells of 5 particles with 1 particle at the centre. This is referred to as an 'ideal' configuration with a commensurate number of particles. If particles move shells then their average radial position is used as a guide. This terminology is used to describe the observed structures: for example 5,5,5,4 corresponds to three shells of 5 particles with 4 particles occupying the the innermost area.

5.3.4 Structural analysis

To characterise the local symmetry environment of a particle, the 6-fold bond orientational order parameter $\Psi_6(r_i)$ is calculated [18]. This represents a method of quantifying how similar the environment created by the nearest neighbours of a particle are from a hexagonal arrangement. A perfect hexagonal system has a Ψ_6 value of 1. Here, a 6-fold order parameter is used rather than a 5-fold parameter due to the majority of particles occupying 6-fold symmetric sites. To this end, first a Delaunay triangulation is used to find the nearest neighbour coordinates for each particle [225]. Next, the bond orientational order parameter is given by:

$$\Psi_6(r_i) = \frac{1}{n_c} \sum_{j=1}^{n_c} e^{6i\theta(r_{ij})} \tag{5.2}$$

where n_c is the coordination number of particle i and $\theta(r_{ij})$ is the angle difference between particles i and j from an arbitrary fixed axis. For simplicity, the absolute value of Ψ_6 averaged over all particles is simply referred to as Ψ_6. For comparison, 16 particles arranged perfectly symmetrically in the pentagonal environment, similar to in figure 5.2a, has $\Psi_6 = 0.71$ and for a fluid system in 2D $\Psi_6 \sim 0.3 - 0.4$ [226].

5.3.5 Dynamical analysis

The mobility of the particles is measured in terms of the mean-squared displacement:

$$\langle r^2(t) \rangle = \frac{1}{N} \sum_{i=1}^{N} [\vec{r}_i(t) - \vec{r}_i(0)]^2 \tag{5.3}$$

where $\vec{r}_i(t)$ is the position of particle i at time t and N is the number of particles. Note that this 2D pentagonal system is sufficiently confined such that no system size based divergence is accorded in contrast to unconfined 2D crystals [204]. The Lindemann parameter represents a general melting criterion [18, 227, 228]. A 2D dipolar system is said to be molten when particle fluctuations in the system are great enough such that the mean square displacement over the lattice spacing squared is greater than $\sim 12\%$ [229]. The dynamic version of the Lindemann parameter, γ_L, is defined as [18]:

$$\gamma_L(t) = \frac{\frac{1}{N} \sum_{i=1}^{N} [\vec{r}_i(t) - \vec{r}_i(0)]^2}{r_a^2} \tag{5.4}$$

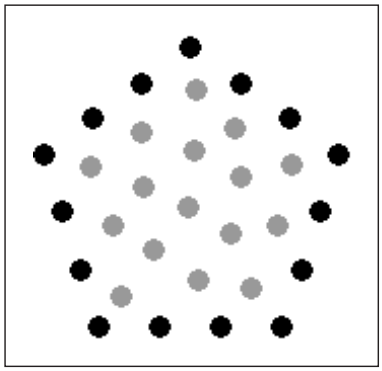

Figure 5.3: Snapshot of a Monte Carlo run for 16 confined particles. The fixed particles (black) and the mobile particles (gray) interact via a $1/r^3$ potential with a hard core diameter of 1.

where r_a is the mean lattice spacing.

Finally, the bond-order correlation function in time, $g_6(t)$, is calculated which describes the decay rate of orientational correlations and is found from a dynamic correlation function of the local bond order parameter Ψ_6 [18, 204]:

$$g_6(t) = \langle e^{i6[\theta(t)-\theta(0)]} \rangle \tag{5.5}$$

where $\theta(t)$ is the angle of the bond between two particles and $\langle\rangle$ represents an average over all bonds. The $g_6(t)$ can act as a melting criterion with a order-disorder transition expected from a crystalline or hexatic phase through to a fluid in bulk 2D systems, when the long time decay scales as $g_6(t) \sim t^{-1/8}$ [230].

5.3.6 Monte Carlo Simulations

Standard Monte Carlo simulations are performed in the canonical ensemble [231] to qualitatively mimic the experimental set-up of particles confined in a pentagonal environment. A snapshot of a Monte Carlo system is given in figure 5.3 showing the fixed (black) and confined, but mobile (gray) particles. Likewise to the experiment, the particles act as point dipoles with a repulsive $1/r^3$ interaction potential. The particles have a non-overlapping diameter of 1 and the outer particles are fixed with a separation of 3 diameters which is comparable to the experiment. The simulation cycles are started by equilibrating the confined particles with 10^3 steps per particle. The step size is adjusted during equilibration so that the acceptance rate of the Monte Carlo

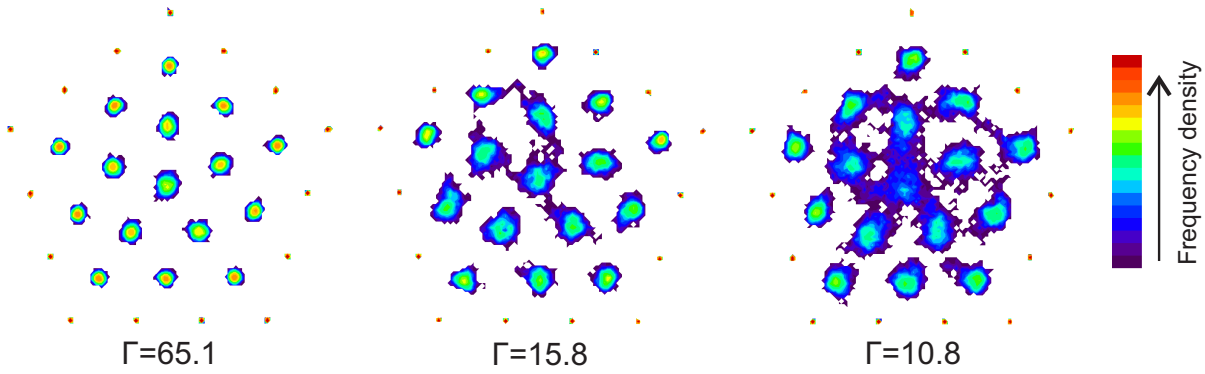

Figure 5.4: 2D histograms displaying the particle positions over the whole experiment. These systems contain 16 confined particles and are shown for the highest ($\Gamma = 65.1$), lowest ($\Gamma = 10.8$) and an intermediate ($\Gamma = 15.8$) repulsive interaction potential.

steps is between 0.3-0.5. The number of inner particles is sequentially increased from 10 to 21 and each time the simulation runs for 10^5 steps per particle. The coordinates of the particles are analysed in the same way as the experimental data.

5.4 Results and discussion

5.4.1 Magnetic field induced melting

Arranged with pentagonal symmetry, the commensurate number of particles that pack within the confining pentagon is 16, which is the configuration shown in figure 5.2a. This commensurate particle arrangement with 5-fold symmetry is similar to that found around 5-fold disclinations in metals [232] and as part of Thomson problem [233]. How this pentagonal system melts as the magnetically induced inter-particle repulsion is decreased is investigated. The magnetic field is reduced to the lower bound whereby the inter-particle potential is just sufficient to confine the particles in the optically tweezed pentagon. The magnetic field, and hence the interaction potential, is expressed in terms of the dimensionless gamma parameter (see eq. (5.1)) which acts as a form of temperature gauge, equivalent to $1/\Gamma$.

Firstly, the spatial structure of the 16 confined colloidal particles are analysed as a function of the sequentially reducing Γ parameter. Two-dimensional histograms that display the

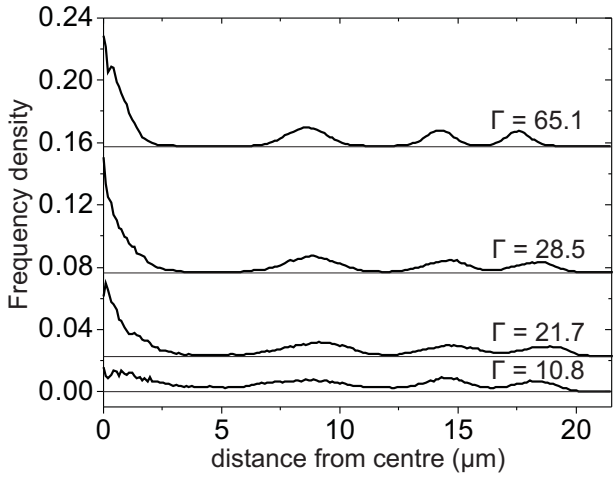

Figure 5.5: 1D radial histograms displaying the particle positions over the whole experiment. These systems contain 16 confined particles and are shown for several Γ ranging from $\Gamma = 65.1$ to $\Gamma = 10.8$.

particle positions for each experiment over the whole observation period are shown for a few representative Γ in figure 5.4. From left to right, the histograms correspond to a decrease in Γ from 65.1 to 10.8. The particle positions change from highly localised to being more evenly distributed as Γ is reduced, suggesting that partial melting is taking place. Also noticeable from all the histograms in figure 5.4, are the varying levels of particle localisation as a function of distance from the boundary.

This effect is also observed in the radial histograms of the particle position distributions plotted in figure 5.5. Here, the change from 4 distinct shells at high Γ, to a more continuous particle distribution, is observed as Γ is reduced. The change in the first peak, corresponding to the shell closest to the pentagon centre, shows the most pronounced change in particle localisation. Likewise to the trend indicated in figure 5.4, the decrease in Γ does not lead to a complete absence of shell structure. The highly confined system still exhibits wall induced layering [234].

For a more quantitative analysis of the local symmetries in the system as the magnetic field is reduced, the orientational order parameter, Ψ_6, is computed. The average Ψ_6 over all particles and time is shown as a function of Γ in figure 5.6a for the experiment along with the Monte Carlo simulation data for the 16 confined particle system as a function of the interaction strength. Both the experimental and Monte Carlo data show a sharp decrease in Ψ_6 upon lowering the interaction strength. This signifies how the colloidal particles change from occupying

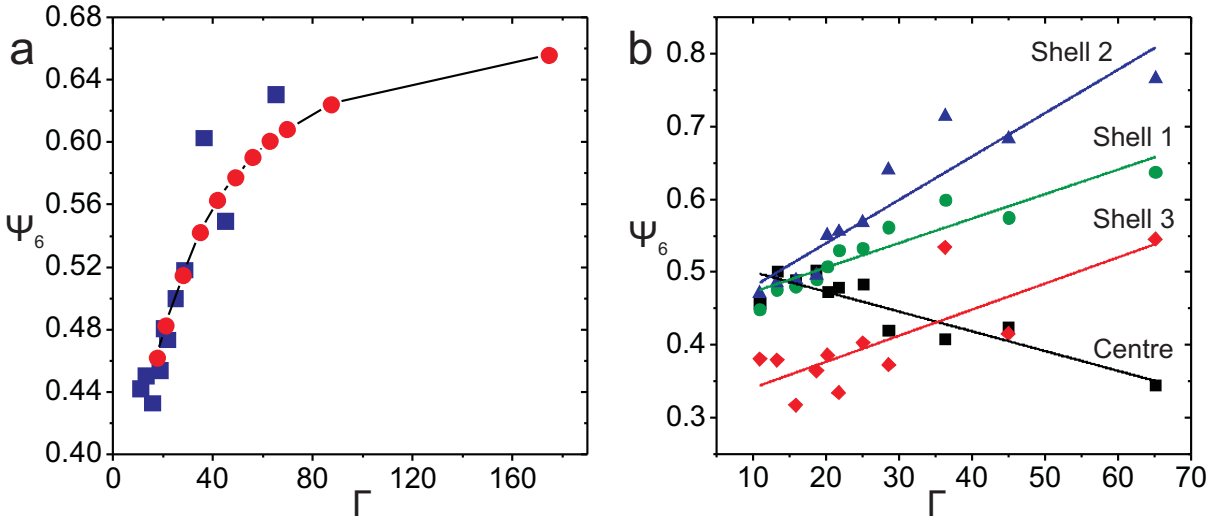

Figure 5.6: a) The orientation order parameter Ψ_6 as a function of interaction parameter Γ for the experiment (□) and the Monte Carlo simulation (◯). b) Ψ_6 as a function of Γ for each shell. Straight line guides to the eye are shown for each shell.

predominately 6-fold symmetric sites to those of a more disordered nature. The lowest Ψ_6 of ~ 0.44 indicates that, as suggested by the 1D and 2D histograms, there is not a complete loss of orientational order in the system at low Γ. Typically an unconfined 2D liquid has a Ψ_6 of 0.3-0.4 [226].

As evident from the histograms in figure 5.5, the behaviour of the colloidal particles differs between shells. To decompose the shell dependent contributions, Ψ_6 is shown in figure 5.6b time-averaged over all particles in each shell as a function of Γ. With the exception of the central particle, a reduction in Γ results in a decrease in Ψ_6. The central particle starts in a predominately 5-fold symmetric site at high Γ and gradually becomes more hexagonal as Γ decreases. In contrast, shells 1, 2, and 3 exhibit a decrease in Ψ_6 with decreasing Γ, as their environments get increasingly disordered. The highest Ψ_6 is seen in shell 2, where the particles are the furthest from the wall and the central disclination. Apart from the central particle, at high Γ, particles in shell 3 have the lowest Ψ_6 as they are confined into the corners in a 'pseudo' pentagonal environment. At low Γ all the shells have a similar Ψ_6, indicating that the shell environments are more homogeneous, the boundary effects less significant and the particle orientational ordering more liquid-like [226].

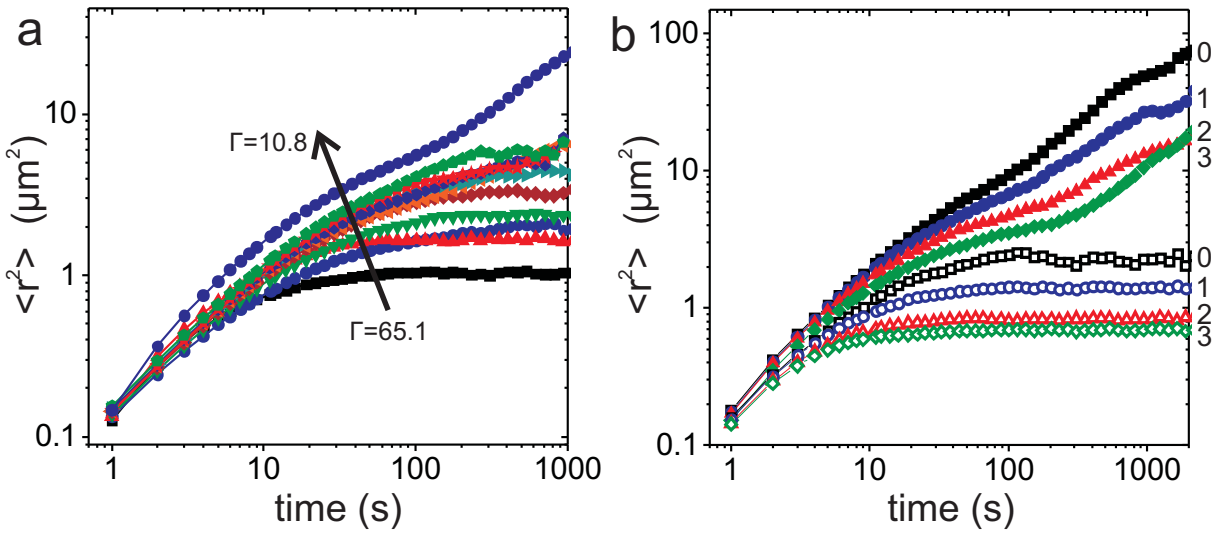

Figure 5.7: a) Mean square displacements (MSDs) for the 16 confined particles for $\Gamma = 65.1$ to $\Gamma = 10.8$. b) MSD as a function of shell for $\Gamma = 65.1$ and $\Gamma = 10.8$. The numbers to the right indicate the shell, for the datasets $\Gamma = 10.8$ (filled symbols) and $\Gamma = 65.1$ (hollow).

The spatial and orientational correlations in the system indicate that the particles undergo a gradual order to disorder transition with decreasing Γ. The dynamics of these confined particles are now analysed, starting with the mean square displacements (MSDs) averaged over all confined particles, as shown in figure 5.7a. A steady progression in the MSD is observed at long times from a plateau at high Γ through to fairly diffusive behaviour at low Γ, indicating a crystalline to liquid-like transition. This trend is consistent with observation of the particle density distributions in figure 5.4 and the trend in Ψ_6. To differentiate the shell-dependent contributions, the MSD per shell is plotted for the datasets corresponding to the highest and lowest Γ parameters in figure 5.7b. The differing long time behaviour between the shells immediately illustrates the strong effects of the confinement. At the highest magnetic field ($\Gamma = 65.1$) shown in figure 5.7b, the MSDs of all shells clearly plateau. As is evident from the different plateau heights, although the particle dynamics are similar to that in a crystal, the confinement effects of the boundary still create differing cage sizes. On reducing the interaction potential to the lowest Γ of 10.8, the MSDs in figure 5.7b demonstrate a switch to more diffusive behaviour at long-times. Likewise to the high Γ case, there is a marked difference in long-time movement between the shells. This shell dependent sub-diffusive particle movement indicates that the

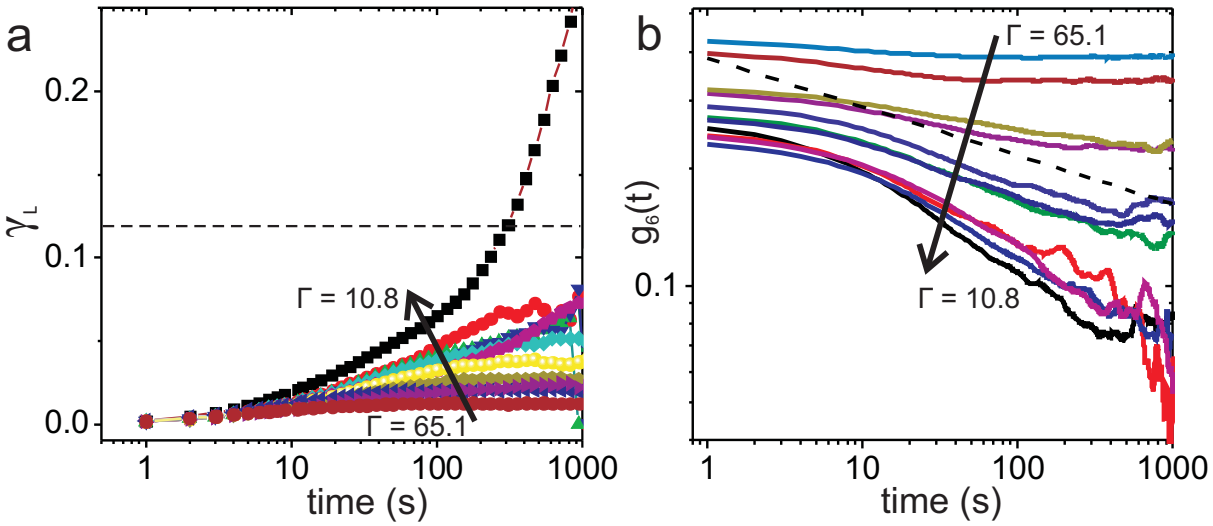

Figure 5.8: a) Dynamic Lindemann parameter plotted for a range Γ with a dashed line indicating the 12% threshold [229]. b) The bond order correlation function in time $g_6(t)$ with decreasing Γ. The dashed line indicates a $g_6(t) \propto t^{-1/8}$ as expected for the hexatic phase [204].

liquid-like state formed still has measurable order and boundary effects.

In order to assign crystalline properties to the data, the dynamic Lindemann parameter γ_L is computed as a function of decreasing Γ, see figure 5.8a. A 2D dipolar system is said to be molten once the Lindemann parameter reaches $\sim 12\%$ [228, 229]. A dashed line in figure 5.8a indicates this $\gamma_L^c = 12\%$ threshold and immediately illustrates how only for $\Gamma = 10.8$ do the particle dynamics reach this level. The Lindemann parameter only reaches $\sim 1\%$ at long times for high Γ, indicating strongly crystalline behaviour. At intermediate Γ, the Lindemann parameter reaches 4%. Here, as can be seen from the central histogram in figure 5.4, the inner particles move significantly, but the outer shell remains localised. For $\Gamma = 10.8$, the Lindemann parameter at long times extends to greater than 25% indicating a confined liquid-like behaviour. Overall, slow change from a crystalline to a highly confined liquid with significant localisation and residual order is observed. Note that this dynamic Lindemann parameter with a $\gamma_L^c = 12\%$ threshold is a typical criterion for bulk 2D systems and must therefore be used with caution in this highly confined environment where it is only shown for reference.

The local bond orientational correlation function in time, $g_6(t)$, is shown in figure 5.8b. The dashed line in figure 5.8b represents a $g_6(t) \propto t^{-1/8}$ which corresponds to the transition

from a crystalline/hexatic phase to a fluid for bulk 2D systems [230]. For the highest Γ there is limited decay of the bond order correlation indicating crystalline behaviour. As Γ is reduced, a weak decrease in orientational order is observed, before at the lowest Γ there is a noticeable drop in correlation at long times. At intermediate Γ, the slope of the decay is indicative of the $g_6(t) \propto t^{-1/8}$ decay, the hexatic/solid to fluid transition. The presence of a hexatic, typified with the presence of quasi-long range orientational and short range translation order is not relevant in this highly confined system and so the relation is merely used as a general melting criterion. Although the exponent decreases further as the system melts, the decay is still algebraic rather then exponential as expected for a liquid, suggesting a more ordered liquid structure due to the confinement.

This highly confined system of 16 particles trapped in a pentagonally shaped environment melts from a localised crystalline-like state at 'low temperature' to a confined-liquid-like state at 'high temperature'. All the results of the analysis are consistent with this change in the dynamics and structure of the confined particles as Γ is reduced. Reducing Γ increases the free volume in the system permitting greater particle dynamics. Closer examination revealed how the melting transition starts at the central particle (a disclination) and propagates outwards as the system tries to remove this defect. The inner shells start to delocalise their positions first, before at the lowest Γ all the shells have started to delocalise. A loss of shell-structure dependence is indicated at the lowest Γ in Ψ_6. However, as the algebraic decay in the bond orientational correlation function indicates and the differences in the MSD between shells at the lowest Γ illustrates, significant particle ordering is still present. These remaining boundary effects display the highly confined nature of the system and the dynamical slowing down near the boundary.

In contrast to the circular system studied by Bubeck *et al.* [197], the confining pentagonal symmetry restricts any shell rotation. They observed a two step melting mechanism facilitated by a shell rotation state. In contrast, the pentagonal system studied here melts with no detectable differences between angular or radial mean square displacements (not shown). The geometry frustrates the system such that complete melting cannot occur, boundary effects are prevalent and the system is best described as a confined liquid.

5.4.2 Particle number induced ordering behaviour

Partial melting occurs in this highly confined pentagonally shaped system when Γ is reduced via control of an external magnetic field. Next, Γ is not controlled via the inter-particle interaction strength, but by the number density of the confined colloidal particles. This is a problem more akin to packing in confinement where the enforcement of an incommensurate 5-fold symmetry on the system is expected to produce frustrated states.

As per section 5.4.1, 15 particles are tweezed to create a confining pentagon. However, here, the number of confined particles, N, is sequentially increased from 10 to 21, whilst keeping the magnetic field constant (2.1 mT). The interaction parameter, Γ, scales with the particle number density via $\Gamma \propto \rho^{\frac{3}{2}}$ (see eq. (5.1)). Therefore, for simplicity the datasets are referred to by their number of confined particles rather than Γ.

Two-dimensional histograms of the particle positions plotted over the observation time as a function of the number of confined colloidal particles are shown in figure 5.9. The relative amounts of particle movement appear to significantly fluctuate, revealing that the levels of packing frustration sensitively vary with the number of confined particles. The different structures that form as the number of confined particles increases from 10 to 21 are also illustrated in the radial histograms in figure 5.10a. The histograms are normalised such that the area under each curve is equal to the number of confined particles in each dataset, allowing direct comparison of the peak heights between datasets. As the number of confined particles increases, the peaks move outwards and an extra peak is also added at 16 and 21, where a particle now occupies the pentagon centre and a new shell is added.

Next, to give a more quantitative analysis of the packing symmetries, the orientational bond-order parameter Ψ_6 is calculated. The Ψ_6 averaged over all the confined particles for each dataset is shown in figure 5.10b, along with results from the Monte Carlo simulations. The Ψ_6 fluctuates almost periodically with the number of particles. There appear to be two distinct regimes in particle ordering behaviour: a general increase in Ψ_6 from 10 to 16 particles and quite different behaviour from 16 to 21 confined particles. The experimental and Monte Carlo results qualitatively show very good agreement. The small systematic deviations relate to the difficulties in mimicking the experiment, including the exact particle pair potentials and fixation

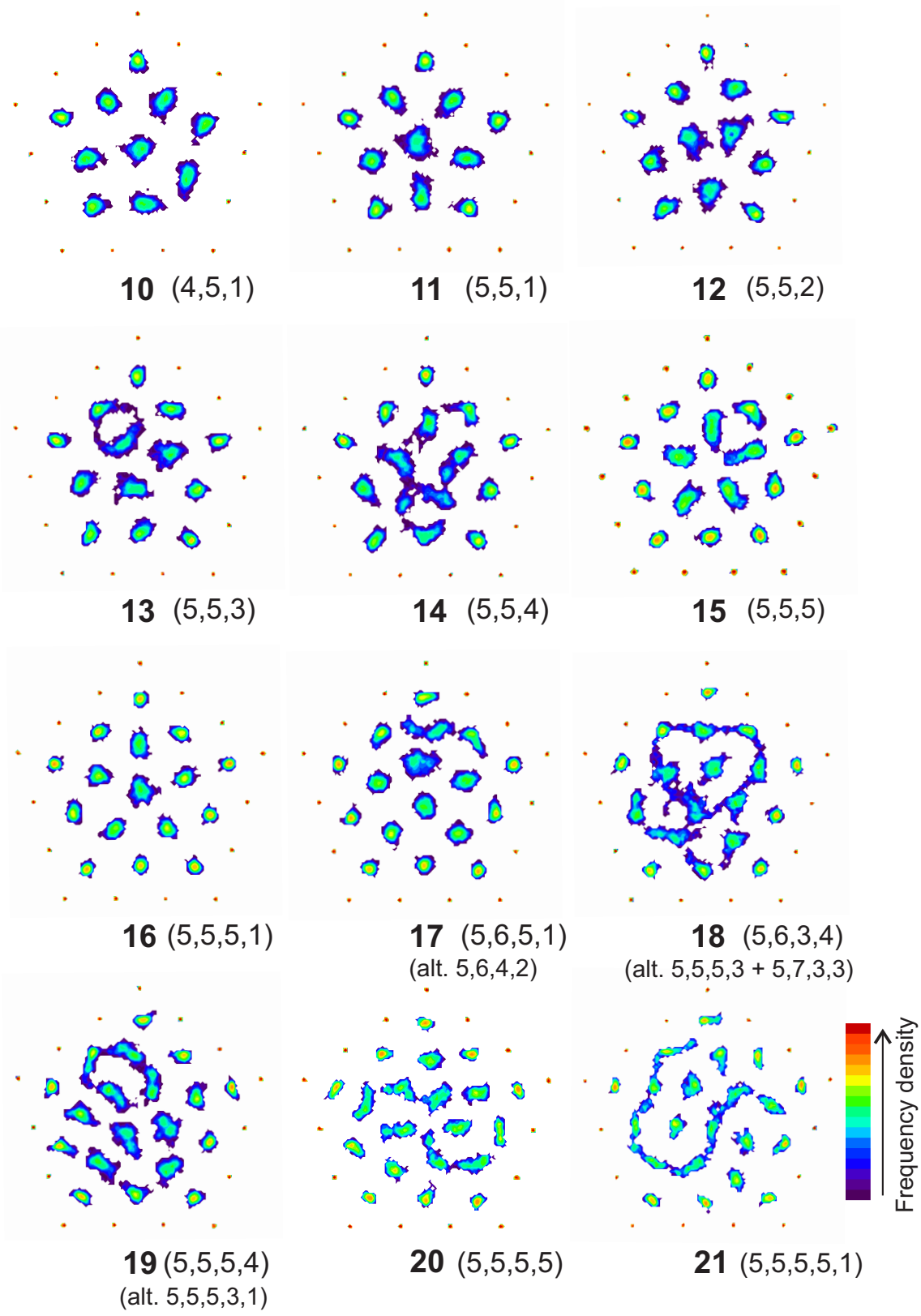

Figure 5.9: Two-dimensional histograms of the particle positions over the observation time as a function of the number of confined particles. The 'codes' describe the structure, see section 5.3.3.

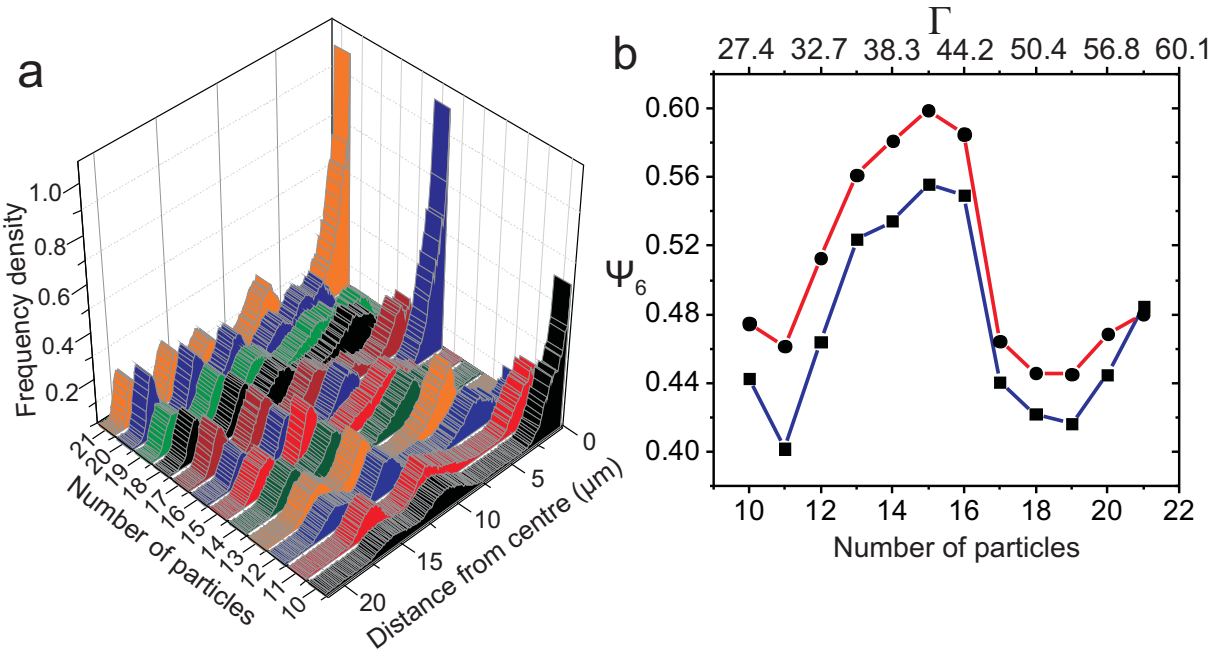

Figure 5.10: a) Radial histograms of the particle positions from the pentagon centre for the whole measurement period as a function of the number of confined particles. Histograms normalised to the number of confined particles in each dataset. b) Ψ_6 averaged over all confined particles for the experiment (squares) and MC simulation (circles) as a function of the number of confined particles and jointly Γ.

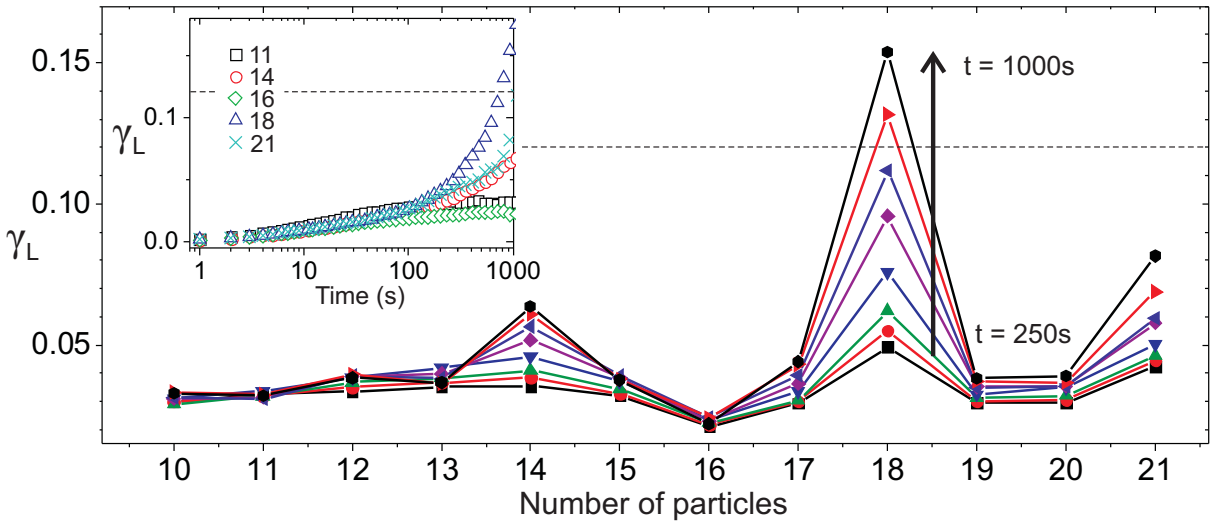

Figure 5.11: Cross-sectional plot of the dynamic Lindemann parameter versus the number of confined particles, shown for t = 250 s to 1000 s. Inset: dynamic Lindemann parameter for datasets 11, 14, 16, 18 and 21. The dashed lines indicate $\gamma_L^c = 12\%$.

of the pentagonal confinement. The effect of increasing Γ by increasing the number density has a profoundly different effect to that seen in section 5.4.1 where Γ was increased with magnetic field. There, a gradual monotonic increase in Ψ_6 was observed, whereas here, the ordering behaviour is highly non-monotonic and almost cyclical in nature with increasing Γ.

The dynamical properties are quantified by the dynamic Lindemann parameter, γ_L, which is shown in figure 5.11 for the full range of numbers of confined particles, N. Due to the fluctuating nature of γ_L, it is displayed as a cross-sectional plot through the conventional γ_L versus time format, which is shown in the inset of figure 5.11 for $N = 11$, 14, 16, 18 and 21. The sample containing 16 confined particles plateaus after the initial diffusive period at $t \sim 250$ s. Therefore for clarity, in figure 5.11 only times greater than $t = 250$ s are shown. The γ_L profiles indicate that the amount of movement in each sample fluctuates greatly, with $N = 14$, 18 and 21 being noticeably more mobile.

The graphs containing the static, figure 5.10b, and dynamic, figure 5.11, behaviour show dramatic changes as the number of particles is increased from 10 to 21. The amount particles move and their local structure appears very sensitive to the particle density and packing symmetry. To explain the observed re-entrant ordering transitions and changes in structure, the discussion is broken down into two sections: $N = 10$ - 16 and $N = 17$ - 21 confined particles. There are three packings that are more commensurate with the confining geometry. These are those containing 11, 16 and 21 particles, arranged with a central particle with rings of 5 particles surrounding them. The structural and dynamical changes occurring as the number of particles passes through these more symmetric states will be discussed in a case by case fashion within each section.

5.4.3 Low number densities: 10 to 16 particles

The shell structures seen in figure 5.9 and figure 5.10a are summarised in the table below for datasets containing 10 - 16 confined particles. For each shell structure, the spatial and orientational changes taking place, particularly in Ψ_6, are analysed before the particle dynamics are then addressed.

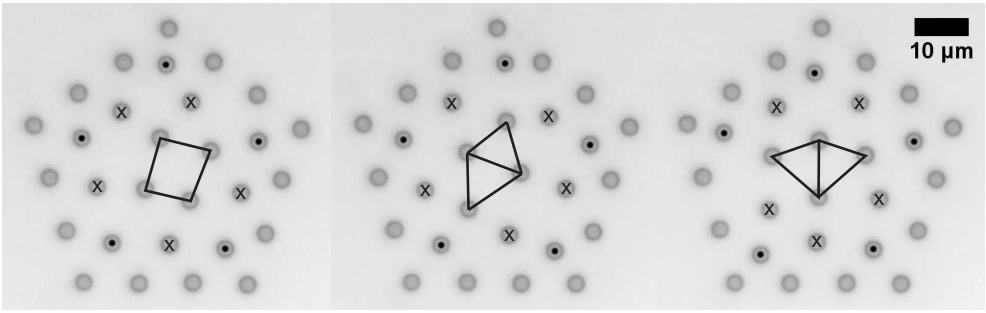

Figure 5.12: For 14 confined particles, a few examples of the actual configurations observed. The inner 4 particles, shell 0, arrange in squares and diamonds, with the vertexes having weak direction dependence. Shell 1 is illustrated by crosses and shell 2 by dots.

Number of particles	Shell structure	Number of particles	Shell structure
10	4,5,1	14	5,5,4
11	5,5,1	15	5,5,5
12	5,5,2	16	5,5,5,1
13	5,5,3		

The first system contains 10 confined particles, see figure 5.9, and has a 4,5,1 shell structure. The incomplete outer-shell leads to an asymmetrical configuration and causes the central particle to fluctuate between 5 and 7-fold symmetry. Addition of one particle, to $N = 11$, results in a 5,5,1 shell structure, which is commensurate with the confining symmetry, and the appearance of the 5-fold symmetric central particle causes the decrease in Ψ_6 seen in figure 5.10b. Addition of a further particle, to $N = 12$, destroys the commensurate configuration, creating a distorted structure, described as 5,5,2. The loss of the single central 5-fold coordinated particle leads to an increase in Ψ_6. A fairly monotonic increase in Ψ_6 can then be observed as the number of confined particles is increased first to $N = 13$ and then up to 14 and 15. Here, this increase in orientational order is due to the increasing particle number density leading to a greater chance of the particles being in a more hexagonal environment, rather than 3 or 4-fold environments common for the inner particles when N is low. Essentially, the system is filling the central shell.

The dynamic Lindemann parameter, γ_L, shown in figure 5.11 illustrates how the dynamics of the confined particles also display a non-monotonic trend as the number of confined particles is increased from 10 to 16. The peaks and troughs in this behaviour do not however, match those in Ψ_6. The changes are more subtle due to combinations of packing symmetry, frustration

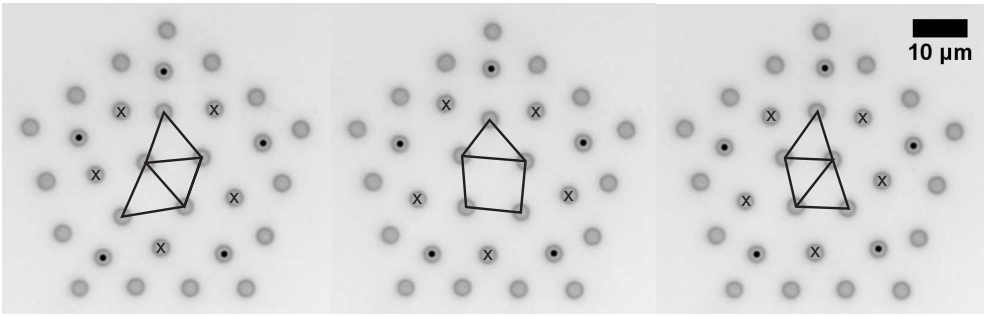

Figure 5.13: For 15 confined particles, a few examples of the particle configurations observed. The 5 inner particles (shell 0) arrange in distorted pentagons, with the vertexes having weak radial and strong angular dependence. Shell 1 is illustrated by crosses and shell 2 by dots.

and free volume changes. The particle dynamics for systems with $N = 10$ and $N = 11$ confined particles are strongly plateaued. Despite their low number densities, the effective particle radii are sufficient for them all to form crystal-like states. The dynamic Lindemann parameters for $N = 12$ and $N = 13$ also plateau, but with a slightly higher cage size despite the increased density. For $N = 12$, a 5,5,2 structure is formed with the 2 central particles off centre and for $N = 13$, with a 5,5,3 structure, the 3 inner particles form a triangle. The amount of movement of the inner particles increases slightly compared to that seen at lower number densities. The 2 and the 3 centrally positioned particles compete to access the other degenerate structures (other rotations of the central particles with respect to the confining symmetry) and hence the particle fluctuations increase slightly, see figure 5.9.

The system containing $N = 14$ particles, a 5,5,4 structure, shows the first real signs of change in terms of particle dynamics, see figure 5.11. Here, as shown in figure 5.12, the 4 inner particles conforming to the pentagonal environment results in several different configurations, ranging from off axis squares to diamonds. These shapes are also not commensurate with the confining geometry, but the greater number of degenerate states that can easily interchange leads to more particle movement than that seen when 2 or 3 particles occupied the centre. The γ_L does however only reach 7%, still indicating solid-like behaviour. The inner particles behave like a confined liquid, but the outer particles remain highly localised, see figure 5.9.

The $N = 15$ particle system has a 5,5,5 structure. However, as figure 5.13 illustrates, the inner 5 particles do not generally form a perfect pentagon shape, but instead various distorted shapes. The amount of particle movement actually lowers again after the peak at $N = 14$. Here,

at $N = 15$, the 5 inner particles more closely match the confining symmetry and as the particle movement is highly cooperative, the particles do not have space to interchange positions and the fluctuations decrease. The movement is however, more directionally dependent, with the fluctuations in the radial direction increased due to switching between the distorted pentagon shapes, see figure 5.13. Despite this particle movement, there is no cage breaking and γ_L plateaus, indicating crystalline-like dynamics. At $N = 16$, the commensurate 5,5,5,1 system forms, this stable configuration locks the particle positions, resulting in crystal-like dynamics as is evident from figure 5.9.

The filling of the central shell as the number of confined particles increases from 10 to 16 has been described. This is illustrated well in figure 5.10a where the number of peaks (shells) stays the same for the 10 to 15 particle datasets, but the position of the central peak (shell) shifts outwards. An abrupt change is then seen on addition of a particle to form the commensurate 16 particle configuration. Four distinct shells are visible including a central peak. Note that an abrupt change is not seen at the commensurate 11 particle system as dataset 10 already has a fairly central particle. These histograms are a good indicator that the transitions observed here as the number of confined particles (Γ) increases, are those of changing orientational order and packing symmetry, which in turn dictate the amount of particle movement possible, leading to the formation of crystalline and highly confined liquid-like states.

5.4.4 High number densities: 17 to 21 particles

The trend observed in Ψ_6 for 10 to 16 confined particles was that of a general increase. Next, the changes in Ψ_6 in the latter half, from particle numbers 17 to 21 are explained. Contrary to that seen in the field melting section, here, an increase in Γ causes a significant drop in Ψ_6 and at first glance seemingly unconnected increases in particle movement, see figure 5.11. The shell structures seen in figure 5.9 and figure 5.10a are summarised in the table below for datasets containing 17-21 confined particles. Note that several systems here show multiple shell structures, the global properties are averaged over these configurations.

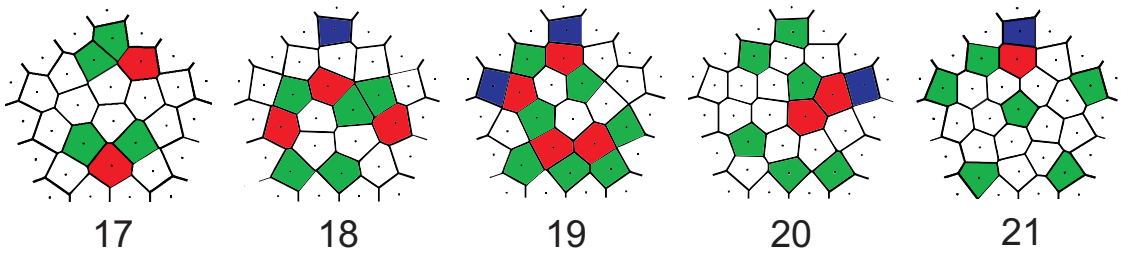

Figure 5.14: Voronoi plots for snapshots for $N = 17$ to 21. Each polygon represents a particle (dot = particle position) and is coloured according to its coordination number, n_c, where $n_c = 4$ blue, $n_c = 5$ green, $n_c = 6$ white, $n_c = 7$ red.

Number of particles	Shell structure	Number of particles	Shell structure
16	5,5,5,1	19	5,5,5,4 + 5,5,5,3,1
17	5,6,5,1 + 5,6,4,2	20	5,5,5,5
18	5,5,5,3 + 5,6,3,4 + 5,7,3,3	21	5,5,5,5,1

Firstly, as an illustration of the general disorder in the particle packing at these densities, as indicated by the multiple structures in the above table, Voronoi plots for snapshots of each system are shown in figure 5.14. The dots represent the particle positions and the number of sides of the polygon indicate the coordination number of each particle. The incomplete boundary polygons are the optically tweezed ring. For clarity those of coordination number, $n_c = 4$ are coloured blue, those for $n_c = 5$ green, $n_c = 6$ white and those where $n_c = 7$ are red.

Likewise to the low number density section, here, first the orientational order and then the particle dynamics are analysed. The 17 particle system starts to break the commensurate shell structure seen in the 16 particle system, as the system becomes overcrowded, see figure 5.9. The exact position of this extra particle can vary, hence the multiple structures formed. In the 2D histograms in figure 5.9 the extra particle is positioned towards the outer shell, distorting the packing symmetry. This change is accompanied by a significant drop in Ψ_6. The system is asymmetric, with an off centre central particle and several dislocations, see figure 5.14.

Addition of further particles to form the $N = 18$ and then $N = 19$ confined particle systems causes only slight reductions in Ψ_6. Here, the packing structures become ever more disordered with more particles forming defects, but due to the disorder already present at 17 it makes little difference to Ψ_6. In contrast to the low number density section, where increasing

the number of particles generally increased Ψ_6 and the number of 6-fold environments, here, Ψ_6 generally decreases due to the fact that the system contains more than the commensurate $N = 16$ particles. Hence, the increased packing fraction forces more particles into 4, 5 and 7-fold environments, particularly the 4-fold corner sites, see figure 5.14.

A slight increase in Ψ_6 is actually observed on formation of the $N = 20$ particle system. Despite the added particle, the symmetry of the system increases due to a 5,5,5,5 shell structure forming with a vacancy at the centre. This central hole is then filled on addition to form the 21 particle system, a 5,5,5,5,1 structure, which is commensurate with the confining geometry and is accompanied by a further increase in Ψ_6. Unlike the earlier transitions to commensurate states (the shifts from $N = 10 \rightarrow 11$ and $N = 15 \rightarrow 16$), here Ψ_6 increases on filling the central hole. Despite forming a 5-fold disclination at the centre, this ordering effect increases Ψ_6 in the outer shells sufficiently to create an overall increase.

In terms of particle movement, as indicated by the dynamic Lindemann parameter in figure 5.11, the dynamics are variable and not coherent with Ψ_6. For the 17 particle system, the particle dynamics are greater than the 16 particle system, but are still fairly plateaued. The most dramatic change in particle dynamics occurs on addition to 18 particles. Here, γ_L , as shown in figure 5.11 demonstrates that the particle dynamics are liquid-like and indicative of melting, easily breaching the 12% threshold expected for melting in 2D dipolar systems [229]. However, the particle movements are also strongly heterogeneous, chains of cooperatively moving particles, constituting the 'molten' particles, move between the remaining highly static particles. This increased particle movement is consistent with the many different shell structures observed, see the table above, just one is illustrated in figure 5.9.

An equally abrupt change in system properties occurs on addition to $N = 19$ particles, here, the particle dynamics shift from liquid-like to crystalline. The particles become jammed and more localised due to the high number density in the system. Such a large change in particle mobility on addition of one particle is remarkable and illustrates the subtleties of the system. The particle density and symmetry at this packing density are not favourable for chains of cooperatively moving particles to form.

Although Ψ_6 changes noticeably between 19 and 20, no change in particle dynamics is observed on forming the 20 particle system. The dynamics are strongly crystalline, and as the 1D and 2D histograms illustrate, see figure 5.9 and figure 5.10a, the particles are highly localised despite their lack of orientational order. On formation of the commensurate 21 particle system an increase in the particle dynamics is observed. Although not as abrupt as the change at $N = 18$, the mobility increases to $\gamma_L \sim 9\%$ at long times, despite the increased number density. This sub-diffusive behaviour is against the trend seen in the other commensurate configurations, $N = 11$ and $N = 16$, who demonstrate strongly crystalline dynamics. It is hypothesised that this mobility increase is due to the higher symmetry helping to unjam the system.

Due to the highly frustrated nature and the long time scales involved in the systems containing high numbers of confined particles, Monte Carlo (MC) simulations were performed to compare with the experimental particle density distributions. The experimental and MC simulation results qualitatively show excellent agreement in the terms of the orientation order parameter Ψ_6, as shown in figure 5.10b. The small differences arise due to difficulty in matching the $1/r^3$ potential between the experiment and simulation and the fixing of the pentagonal array.

The 2D histograms for the MC simulations for datasets with 16 to 21 confined particles are shown in figure 5.15. The simulation is far more efficient at sampling phase space than the experiment. To enable a better comparison with the simulation the sampling of the experiment is artificially increased by computing all the symmetry operations, for all the particle positions, over all time. Given the 5-fold rotational and the 5 reflection symmetry axes present in the system, and setting the pentagon centre as the reference, the colloidal particle positions over the experimental run are rotated and reflected 5 times each. The 'equilibrium' histograms of the experimental data are shown in figure 5.15 along side the MC histograms. The 2D histograms of the particle coordinates from the MC simulation are in good agreement to the symmetry adjusted experimental data for all the number densities shown in figure 5.15. The peaks and troughs in intensity all lie at the same positions around the pentagon. This illustrates that although not all the configurations are sampled within the duration of the experiment it is consistent with the 'equilibrium' behaviour of the simulations.

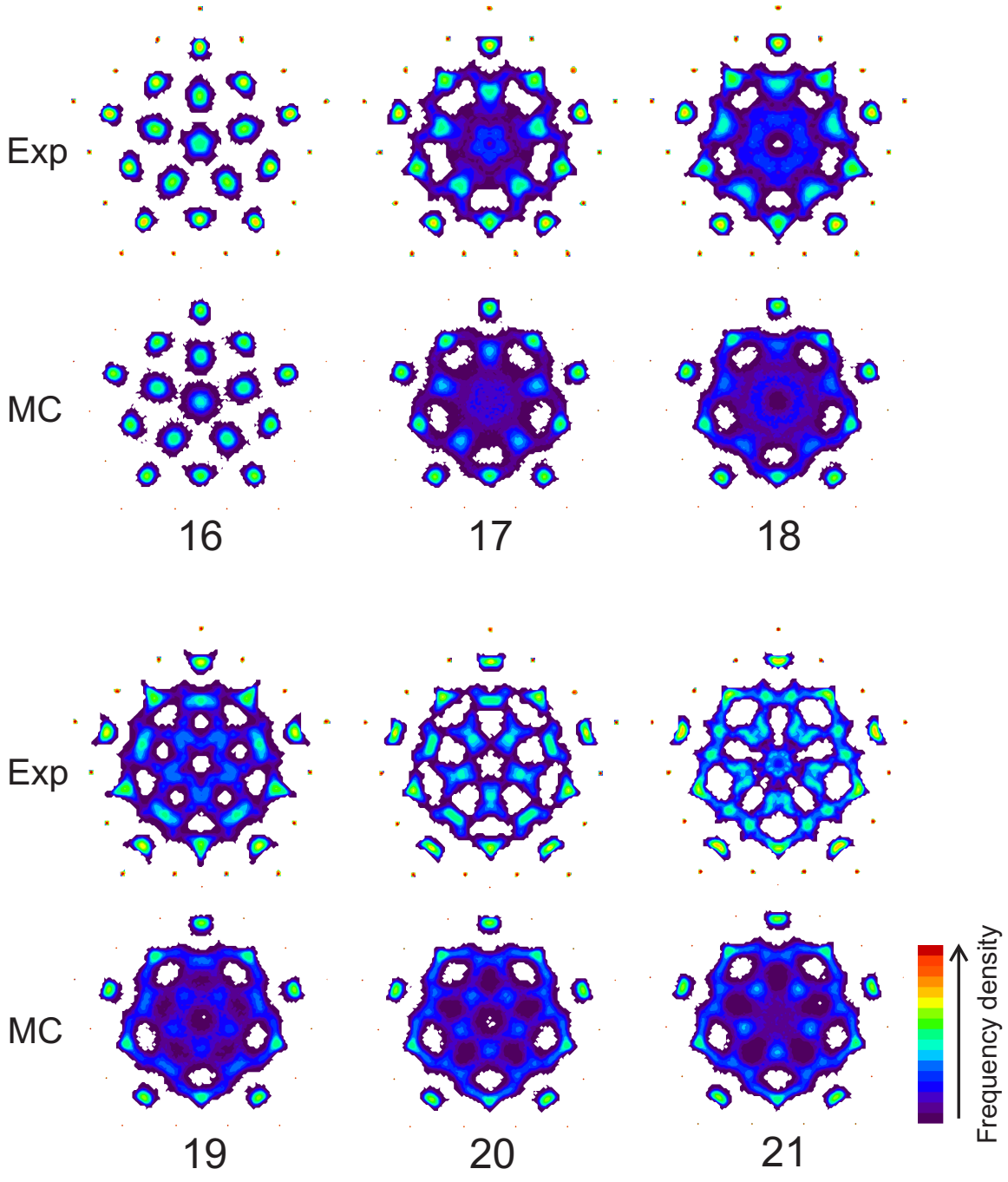

Figure 5.15: Two-dimensional histograms for the Monte Carlo simulations and the experimental data rotated and reflected (5 ×), shown for datasets with 16 to 21 confined particles.

5.5 Conclusions

The structure and dynamics of particles confined in a pentagonal environment have been studied. The state of the system is characterised by Γ which depends on both the magnetic field and the particle number density. Both these pathways were probed to alter Γ and in doing so displayed quite contrasting results. In the field melting section, the behaviour of the commensurate 16 particle system was studied as a function of decreasing interaction parameter, Γ. At the highest Γ, the confined particles were highly localised and the state described as crystal-like owing to the lack of hexagonal symmetry and the central disclination. On lowering Γ, the melting transition started at the central disclination and propagated outwards. The dynamics of the confined particles at low Γ were clearly liquid-like, even for the most localised particles. However, observation of the 1D and 2D histograms illustrated the clear shell behaviour still present in the system. Hence, the structures formed from melting the crystal-like state were referred to as a confined liquid, where the boundary effects prevented a complete loss of environment dependence.

In the second section, Γ was increased via particle density rather than decreased through magnetic field. The dynamic and structural behaviour displayed almost cyclical properties as the number of confined particles was increased from $N = 10$ to $N = 21$. The orientational order parameter, Ψ_6, was seen to increase with particle number up until $N = 15$ particles, in a similar fashion to that seen in the field melting behaviour. However, on increase to 16 particles and beyond, a general decrease in Ψ_6 was observed before a final increase again at 21 particles. This almost periodic re-entrant ordering behaviour is a result of the pentagonal environment where the level of packing frustration and symmetry is highly dependent on the number of particles. Parallel to the orientation effects, the dynamics of the confined particles fluctuated with a pattern incommensurate to the oscillation in Ψ_6. The cross-sectional plot through the dynamic Lindemann parameter, see figure 5.11, displayed this variable particle mobility and therefore serves as a useful 'state diagram' for the mobility as a function of number density. The symmetry and orientational order in the packing arrangements affects in turn the particle dynamics, the system is therefore highly sensitive to the number of confined particles. Notable

effects included a rapid increase in particle mobility at 18 particles due to the system trying to access the different degenerate particle configurations. This dynamic behaviour disappeared at 19 particles despite no change in Ψ_6.

Acknowledgments

This work was done in collaboration with Henry Martin and Dirk Aarts. Roland Roth is thanked for useful discussions.

Chapter 6

Particle dynamics in random confinement

ABSTRACT

The behaviour of a two-dimensional (2D) colloidal fluid confined within a random matrix of obstacles is studied using optical microscopy. A binary mixture of colloidal particles is confined in 2D such that the large particles become fixed whilst the small particles remain mobile. The large static particles form the confining random matrix around which the small particles, the fluid, are able to move. Both the large and small colloidal particle have super-paramagnetic properties, allowing the inter-particle potential and hence the effective area fraction of the fluid and the matrix to be controlled with an external magnetic field. The state diagram of the effective area fraction of the matrix versus that of the fluid particles is mapped out using the Barker-Henderson formalism. Starting from different number densities of the matrix and fluid particles, the external magnetic field is increased to scan across the state diagram. At each state point, the particle dynamics are studied. Good agreement is found with both simulation and theory, with a slowing down of the dynamics of the fluid particles characteristic of the onset of a type B glass transition observed at low matrix density and a localisation-diffusion dominated type A glass transition at high matrix density.

6.1 Introduction

The movement of fluids through porous media is of significance to many fields, including the pharmaceutical, oil and gas industries. Materials containing pores are widely used as filters for molecular sieves [235, 236] and as catalysts [33]. The transport of liquids through soil and rock formations is important for oil and gas extraction and for the removal of pollutants. Improved knowledge of the effects of confinement on the diffusion and absorption of liquids in these porous materials is key to improving performance in these industries. In addition, the phase behaviour of fluids is well known to differ in confinement [188, 189] and is of vital importance to the geological processes of frost heaving and freeze thaw weathering [237]. Liquids confined in porous matrices also have similarities to the percolation networks [238] formed in the jamming transition of granular materials [239]. In particular, the effects on fluid behaviour of both porous and planar confinement have been well documented, with observations of both increases and decreases in the glass transition temperature [154, 240, 241]. These studies are however, performed in porous glasses [242] where systematically controlling and varying the pore size and connectivity is difficult. Hence, for systematic particle level studies over many matrix configurations, simulation and theory provide a useful pathway for characterising these systems.

The simplest model for describing transport in heterogeneous media is the Lorentz model [36, 243]. Here, a single tracer particle (a 'fluid' particle) explores a randomly distributed array of fixed overlapping obstacles (the 'matrix' particles). A theoretical formalism was then put forward by Krakoviack in 2005 [34, 244] who used mode coupling theory to study a Lorentz model-based system, with variable fluid and matrix densities, to describe the dynamics of fluids in random porous matrices. The results of this theoretical framework were then tested by a number of molecular dynamics simulation studies of hard sphere fluids confined in porous matrices by Kurzidim *et al.* [35, 245, 246] and Kim *et al.* [247]. The aim in this chapter is to systematically analyse in experiment, the effect of a confining array of fixed colloidal particles, the 'matrix', on the dynamics of free colloidal particles acting as the 'fluid'. This study provides a direct comparison to the simulation studies, through analysis of the single particle dynamics of the confined fluid.

6.2 Background

6.2.1 Glass transitions in confinement

When a liquid is cooled below its melting temperature without it freezing, it is defined as supercooled. As the liquid is cooled further, the particle dynamics slow down, the viscosity increases, and the structure approaches an arrest scenario [153]. This bypassing of the freezing transition eventually results in an amorphous metastable state known as a glass. The dynamical slowing down is characterised by an increase in the fluid relaxation time, the characteristic timescale over which a system returns to equilibrium after a perturbation. The glass transition temperature is defined in molecular systems by a viscosity of 10^{12} Pa s [154, 248]. This great increase in viscosity and in relaxation times occurs despite only a small change in structure. A characteristic feature of supercooled liquids approaching the glass transition is the formation and growth of dynamical heterogeneities and cooperatively rearranging regions in the liquid [142,156].

Phase changes are well known to differ under confinement, for instance freezing point depression in small pores [188–190], and see chapter 5. The glass transition temperature has also been shown to shift under confinement with reports of a reduction in the glass transition temperature in liquids confined in nanometer size pores [249]. The glass transition is synonymous with increasing time and length scales of particle relaxation. When the length-scales of the porous confinement approaches or becomes smaller than these intrinsic length scales, finite size effects are expected to impact on the glass transition [250, 251]. By reverse argument, observing at what confinement size the glass transition is altered gives an indication of the size of cooperative length scales in the supercooled liquid [252].

The effect of porous confinement on the glass transition is far from clear [154, 240]. The glass transition temperature has been determined experimentally for many different materials within differing porous confinement. However, the transition temperature has been seen to both increase and decrease with respect to the transition in the bulk [241,253–256]. Observations have been made of the same liquid producing differing directions of change in the glass transition, whilst in different material confinement [248]. Furthermore, these experimental studies cannot easily access the single particle dynamics or systematically assess a wide range of pore structures.

These difficulties have therefore provoked further interest in theoretical and simulation studies of the dynamics of fluids in random confinement, starting with the Lorentz model, these are now discussed.

6.2.2 Theoretical and simulation predictions for fluids in random media

The Lorentz model represents a method for describing transport in heterogeneous media where a single tracer particle explores a randomly distributed array of fixed hard-core obstacles [36, 257]. The obstacles are distributed such that they may overlap forming clusters and trap the tracer particle in voids. At low obstacle densities the tracer particle is able to diffuse normally throughout the percolating network of voids. However, as the obstacle density is increased, at a certain threshold, the voids no longer percolate the whole system and a percolation transition occurs [238]. The tracer particle experiences a localisation transition, where at this critical density and above, the tracer particle is always trapped in the disconnected voids between the obstacles. The localisation transition is characterised by a continuous decay in the dynamic correlators and anomalous sub-diffusive behaviour at long times [247, 258], see figure 6.2.

Until recently, there had been less extensive work on any theoretical or simulation studies to investigate systems containing multiple interacting tracer particles. Mode coupling theory (MCT) has been successfully employed to predict many aspects of the slowing down of structural relaxation that occurs on cooling towards the glass transition [259, 260]. An extension to mode coupling theory was made by Krakoviack [34] in 2005 where he applied MCT to study the dynamics of fluids confined in porous matrices, using the quenched-annealed (QA) formalism. As the name suggests, this method of creating the random porous matrix involves first equilibrating the positions of the matrix particles within the system, quenching them to form a static matrix, before finally the fluid particles are inserted and equilibrated.

A schematic of the liquid-glass state diagram of a 3D hard sphere system predicted by this extension to MCT is shown in figure 6.1. Here, the volume fraction of the fluid particles, ϕ_F, is mapped out versus the volume fraction of the matrix particles, ϕ_M. The theory predicts many interesting features including two types of glass transition and a re-entrant glass transition at high ϕ_M. A 'type B glass transition' is expected at low ϕ_M and high ϕ_F and is that seen com-

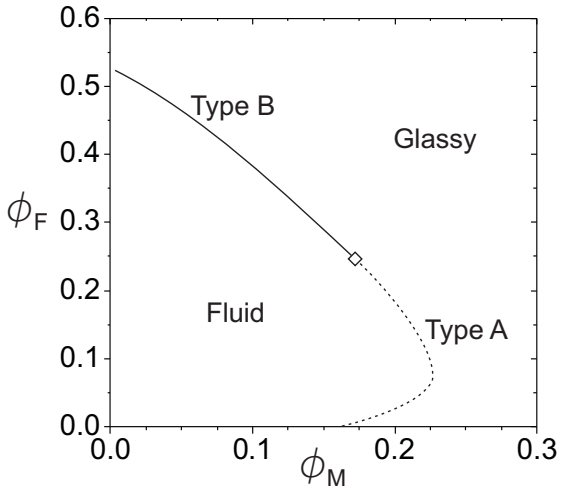

Figure 6.1: A schematic of the hard sphere dynamic state diagram predicted by Krakoviack [34] for the fluid-glass transition in 3D. The volume fraction of the fluid particles, ϕ_F, is mapped out versus the volume fraction of the matrix particles, ϕ_M. Two types of glass transition are predicted, a type B at low ϕ_M and a type A at high ϕ_M.

monly in bulk glass forming systems [259], with a two step relaxation observed in the dynamic correlators (e.g. the mean square displacement or the self intermediate scattering function). Characteristic type B behaviour involves initial diffusive behaviour at short times, at intermediate times a dynamical slowing due to the particles being trapped in cages, and at longer times the appearance of a further diffusive regime as the particles escape their cages [258]. The 'type A glass transition' is predicted at high ϕ_M and low ϕ_F, where there is a high density of matrix obstacles. Here, as the system tends to very low ϕ_F the system resembles a Lorentz model with a localisation transition expected as ϕ_M increases. The localisation transition occurs when the fluid particles get trapped in unconnected pores in the matrix preventing full relaxation at long times and a gradual single step relaxation in the dynamical correlators [36]. The characteristic behaviour expected for a type B glass transition and a localisation transition is illustrated in the schematics of the mean square displacement in figure 6.2.

In recent years, several molecular dynamics simulations [35, 245, 247, 258] have been conducted to investigate the phase behaviour of hard spheres confined in a random matrix and show good agreement with the theory predicted by Krakoviack [34, 244]. Using the QA method both the standard type B glass transition and the diffusion-localisation type A glass transition have been observed. The dynamic arrest of particles has also been studied in MD simulations

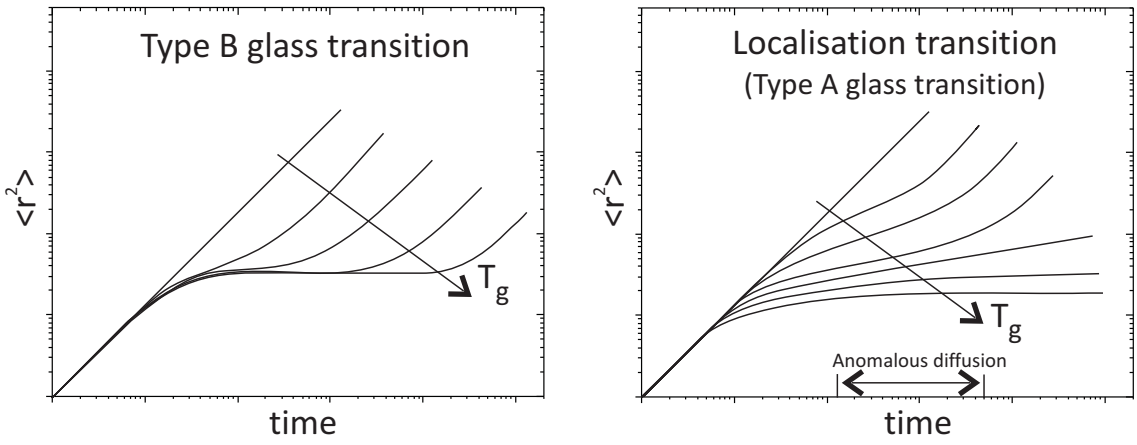

Figure 6.2: A schematic displaying the expected behaviour of the mean square displacement for a type B glass transition (T_g) and a localisation transition (type A glass transition). The type B transition is characterised by a constant plateau height and lack of a clear long time exponent during the upswing before a return to diffusive behaviour at long times. The localisation transition displays a decreasing plateau height and exhibits anomalous sub-diffusive behaviour with a clear constant exponent over significantly long times.

of a binary system of large and small particles [261]. Here, both sets of particles are mobile, but with relaxation times differing by orders of magnitude. Anomalous diffusion behaviour has been reported, indicative of competing mechanisms for dynamic arrest, i.e. both type A and type B particle relaxation pathways. Although these systematic theoretical and simulation studies have been conducted in 3D systems, a large discrepancy in behaviour is not expected between 2D and 3D. Two-dimensional binary systems [262] and 2D Lorentz gases [36] have been shown to exhibit qualitatively similar glass and localisation transition behaviour to their 3D counterparts [263, 264].

In this chapter, the dynamics of the small mobile particles in random confinement are analysed. Firstly, the experimental procedure is outlined, including the manufacture of the 2D sample cells, followed by an overview of the various statistical methods that will be used to characterise the system. The state diagram is presented before the various lines across the phase diagram are analysed. The system is characterised in terms of static correlations and then single particle dynamics and similarities to the effects of random porous confinement in hard sphere simulations [35, 247] are assessed.

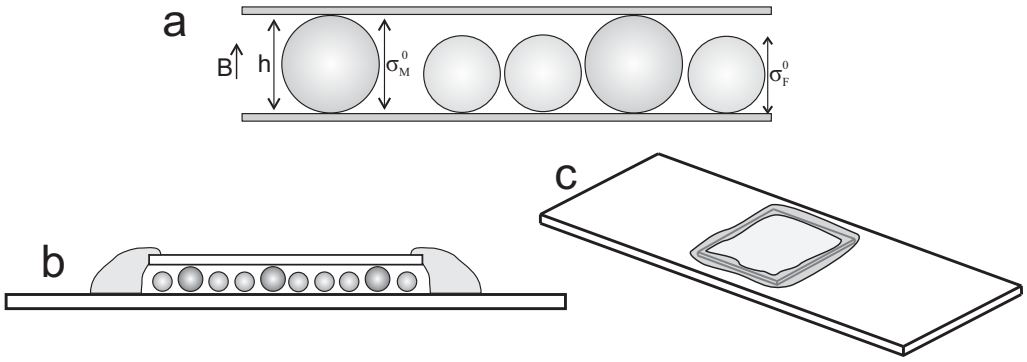

Figure 6.3: a) A schematic of a binary system of small and large particles confined between two glass slides. The large particles support the top slide. B is the magnetic field, h the cell height and σ_F^0 the small particle diameter. b) An illustration showing how the 2D confinement is sealed with UV glue and c) illustration of the whole 2D sample cell, approximately to actual scale.

6.3 Experimental methods and data analysis

6.3.1 Colloidal model system

A binary mixture of 3.9 μm and 4.95 μm diameter super-paramagnetic polystyrene spheres (microParticles), as introduced in chapter 2, section 2.1.5, are dispersed in water. The colloidal particles contain carboxyl surface groups that dissociate in water creating a short-range screened Coulombic repulsion. The colloidal particles have super-paramagnetic properties that stem from the iron oxide nanoparticles distributed throughout their polymer matrix and gain a magnetic dipole parallel to an externally applied magnetic field.

A suspension of colloidal particles is confined between two glass slides to make a 2D sample cell. The large particles act as spacers to support the upper slide, leaving the small particles free to move between them, see figure 6.3a. To ensure that the interaction potential between the colloidal particles is always repulsive, and hence keep the small particles in the plane, the height of the 2D sample cell, h, must be less than $h \approx 1.447\sigma_F^0$, where σ_F^0 is the small particle diameter [265]. The size ratio of the small to large particles used in the binary mixture is therefore selected accordingly and corresponds to a size ratio of 1:1.27. The schematic in figure 6.3a illustrates to scale, the particle size ratio used and the 2D confinement.

6.3.2 2D sample cells

A binary sample with a particular number density and number ratio is confined inside a 2D glass sample cell. The manufacture of which was briefly described in chapter 2, section 2.2.6 and is recapped here in more detail. 2D glass sample cells are created by sandwiching a colloidal sample between a large lower glass slide and small upper glass cover slip. The large particles act as spacers and set the height h between the slides. The edges of the cell are then sealed with UV glue. The volume of colloidal suspension is set to 1.11 μl to create a 15 mm × 15 mm × 4.95 μm internal sample volume. The resulting glass sample cell contains 4.95 μm colloidal particles which are fixed in position between the upper and lower glass plates and amongst them, mobile 3.9 μm colloidal particles. The large glass slides used are Sail 76 × 25 × 1.2 mm and the small glass cover slips Menzel-Glaser 15 × 15 × 0.15 mm.

The procedure of making 2D cells is as follows; the upper and lower glass slides are rinsed in distilled water, twice with absolute ethanol and then dried with an air gun. 1.11 μl of the required concentration of colloidal suspension is placed in the centre of the large glass slide. Working quickly the small glass slide is placed on top of the solution. Using a 10 g weight pressure is applied to aid the liquid spread to the edges of the top slide. UV glue (Norland no. 82) is gently spread around the edges of the top slide and cured under a UV lamp. The cells typically last for 2 days before starting to dry out.

After cell manufacture, the positions of the small colloidal particles are equilibrated for 30 minutes. The external magnetic field is set to the required value and the sample allowed to equilibrate for a further 20 minutes. Using optical video microscopy stacks of 8-bit 1024 × 1280 pixel images are taken at typically 1 Hz for one hour. The colloidal particles are located by standard particle tracking routines [74], see chapter 2, section 2.3. An optical microscopy image of the system is shown in figure 6.4 displaying the distribution of the small and large colloidal particles. The 3.9 μm colloidal particles are referred to as the 'fluid' and the 4.95 μm colloidal particles as the 'matrix'. The 3.9 μm and 4.95 μm diameter colloidal samples that make up the binary system are fairly monodisperse, each with a coefficient of variation of $< 3\%$, but this still leads to particles with sizes between the two. This slight size dispersity is noticeable from observation of the colloidal particles in the microscope image, inset in figure 6.4. Colloidal

particles are reclassified as fluid or matrix according to their mobility where required. This concerns only a very small fraction of the particles. Any drift in the colloidal particle positions due to temperature fluctuations in the microscope are corrected for with respect to the fixed 4.95 μm particles. This leads to the coordinates of both the 3.9 μm (fluid) and the 4.95 μm (matrix) colloidal particles being found for each time frame.

6.3.3 Mapping to packing fractions

The inter-particle interaction potential of the super-paramagnetic colloidal particles is controlled via an external magnetic field. In order to calculate the effective packing fraction for the colloidal particles with these soft repulsions, an effective hard sphere particle diameter is calculated using a Barker-Henderson like approach [169, 266, 267]. The soft $\frac{1}{r^3}$ potential is mapped onto that of an effective hard sphere diameter σ_{eff} as a function of the applied magnetic field according to:

$$\sigma_{eff} = \sigma^0 + \int_{\sigma^0}^{\infty} (1 - e^{-\beta U(r)}) dr \tag{6.1}$$

where σ^0 is the original hard sphere diameter and $\beta = 1/k_B T$. The interaction potential, $U(r)$, is given by $U(r) = \frac{\mu_0 \chi^2 B^2}{4\pi r^3}$ for two parallel magnetic dipoles separated by a distance r and where μ_0 is the permeability of free space and χ the magnetic susceptibility of the colloidal particle, see eq. (2.5) in chapter 2.

In combination, manipulation of both the colloidal particle density and the effective hard sphere diameter allows the state diagram of the area fraction of the large versus the area fraction of the small colloidal particles to be mapped out. This enables one sample cell, which contains a particular particle density and number ratio, to probe higher area fractions by increasing the magnetic field. To improve statistics and minimise the effect of inhomogeneities in number density, each image is divided into quadrants, see figure 6.4. Each quadrant is analysed separately and mapped onto the hard sphere state diagram. These data points are then binned according to their position on the state diagram to create points averaged over several similar matrix configurations and fluid particle densities.

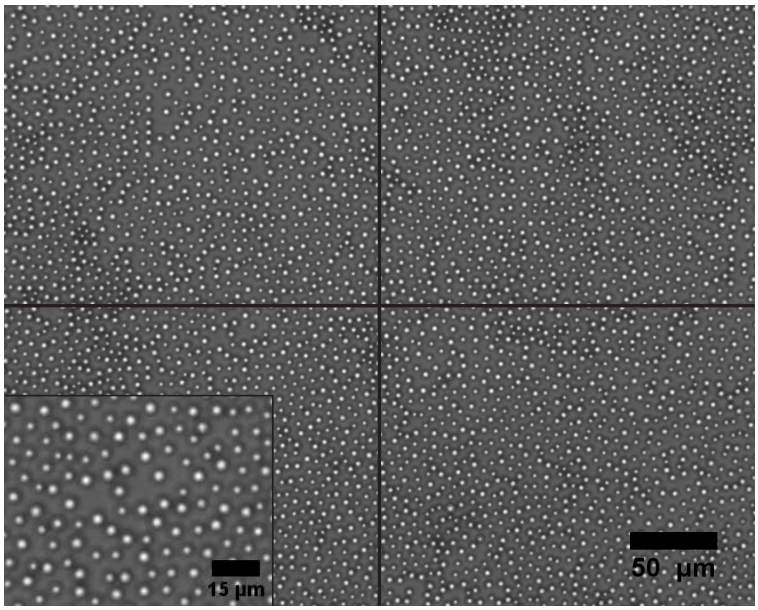

Figure 6.4: A binary mixture of 3.9 μm and 4.95 μm diameter colloidal particles dispersed in water and confined within a 2D sample cell. The four quadrants used to divide the data are shown. Inset: an area of the cell at higher resolution.

6.3.4 Static correlations and single particle dynamics

The analysis techniques that will be applied to the colloidal particle coordinates to characterise their static and dynamic properties are presented here. Firstly, to analyse the static correlations of the colloidal particles the radial distribution function, $g(r)$, is used [169]:

$$g(r) = \frac{1}{\rho} \left\langle \sum_{i}^{N} \sum_{j \neq i}^{N} \delta[\vec{r} - \vec{r_j} + \vec{r_i}] \right\rangle \tag{6.2}$$

where i and j are the indices that run over all N particles and ρ is the average particle number density. The static structure factor, $S(k)$, also quantifies the static correlations in the system and is defined in this isotropic system as:

$$S(k) = \frac{1}{N} \left\langle \sum_{i}^{N} \sum_{j \neq i}^{N} \mathrm{e}^{-i\vec{k}\cdot(\vec{r}_i - \vec{r}_j)} \right\rangle. \tag{6.3}$$

where N is the number of particles, the $\langle\rangle$ represents an ensemble average and $\vec{r_i}$ and $\vec{r_j}$ are the positions of particles i and j. The wavevector $\vec{k}$ is defined as $k = |\vec{k}| = 2\pi/L$ and L is the system size. Note that $g(r)$ and $S(k)$ are computed for all combinations of fluid-fluid, matrix-fluid and matrix-matrix particles.

The single particle dynamics are characterised by calculating the self part of the van Hove correlation function [169], $G_s(x,t)$. This corresponds to the probability distribution that a particle has traveled a distance x in a time interval t:

$$G_s(x,t) = \frac{1}{N}\left\langle \sum_{i=1}^{N} \delta\left(x + x_i(0) - x_i(t)\right)\right\rangle. \tag{6.4}$$

Consequently, the particle mobility is measured in terms of the mean-squared displacement (MSD), $\langle x^2 \rangle$, which is defined as the second moment of $G_s(x,t)$ [169]:

$$\langle x^2(t)\rangle = \frac{1}{N}\sum_{i=1}^{N}[x_i(t) - x_i(0)]^2 = \sum_{i=1}^{N} x^2(t) G_s(x,t) \tag{6.5}$$

The non-Gaussian behaviour of the self part of the correlation function can be quantified by the non-Gaussian parameter, α_2, defined as:

$$\alpha_2(t) = \frac{\langle x^4(t)\rangle}{3\langle x^2(t)\rangle^2} - 1, \tag{6.6}$$

where $\langle x^4 \rangle$ is the fourth moment of $G_s(x,t)$. The level of any heterogeneity in the particle dynamics can therefore be deduced from the time development of α_2, which is zero for a Gaussian distribution, and $\alpha_2 > 0$ for non-Gaussian behaviour. Together, the van Hove correlation function and the non-Gaussian parameter are useful tools for characterising the degree of heterogeneity in particle motion across the sample. The logarithmic derivative is used to aid analysis of the mean square displacement and is defined as:

$$z(t) = \frac{d[\log\langle r^2(t)\rangle]}{d[\log(t)]} \tag{6.7}$$

where $\langle r^2(t)\rangle = \langle x^2(t)\rangle + \langle y^2(t)\rangle$ and z represents the exponent of the mean square displacement where $\langle r^2(t)\rangle \propto t^z$ [245]. The self-part of the intermediate scattering function (ISF) is defined as:

$$F_s(k,t) = \frac{1}{N}\left\langle \sum_{j=1}^{N} e^{i\vec{k}\cdot[\vec{r_j}(t) - \vec{r_j}(0)]}\right\rangle. \tag{6.8}$$

The ISF is probed at wavevectors corresponding to the first peak in the fluid-fluid $S(k)$ averaged over all the state points ($k = 1.4\ \mu\text{m}^{-1}$).

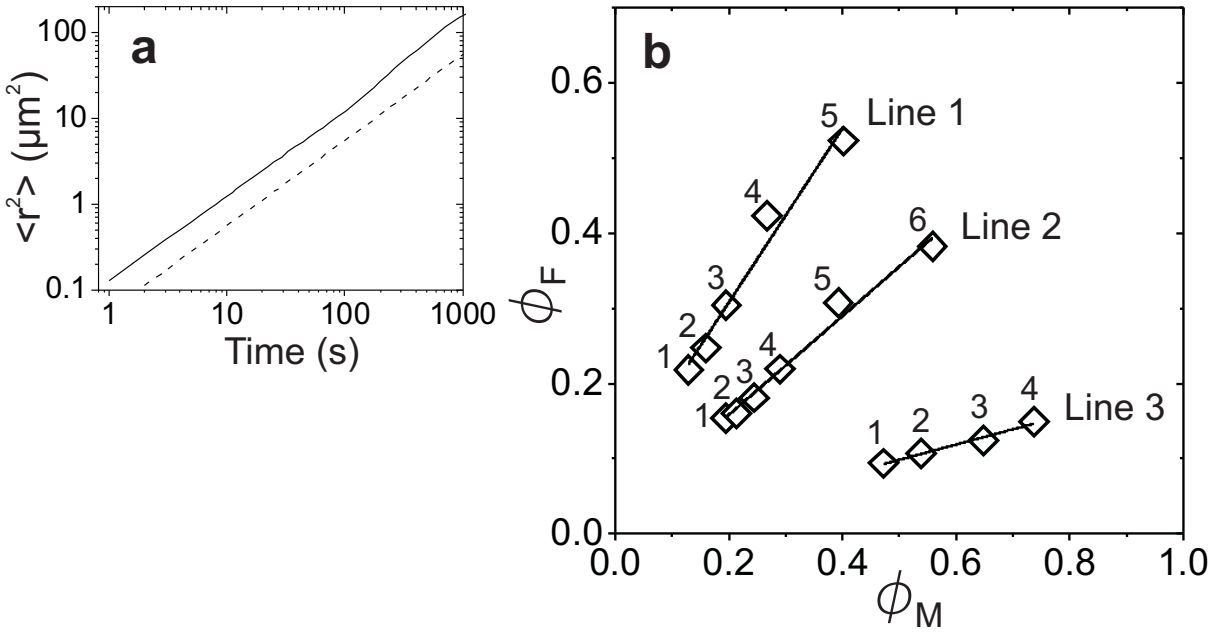

Figure 6.5: a) Mean square displacement for the fluid particles in a very dilute 2D cell. b) State diagram displaying the effective area fraction of the fluid particles (ϕ_F) against that of the matrix particles (ϕ_M). The three lines across the state diagram are designated as lines 1,2 and 3 and each state point is labeled.

6.4 Results and discussion

Firstly, to characterise the fluid behaviour at very low fluid and matrix density and rule out any 'undesired' effect of the confinement, a 2D cell is made with very few large particles, just enough to act as spacers, and containing a very low fluid particle concentration. The MSD in figure 6.5a displays clear diffusive motion and indicates that the fluid particles are free to diffuse within the 2D cells.

The state diagram of the effective area fraction of the fluid particles (ϕ_F) versus that of the matrix particles (ϕ_M) is shown in figure 6.5b. The state diagram displays the state points that constitute three lines, labeled 1, 2, and 3. The state points are numbered along each line starting from that of the lowest effective area fraction. The lowest state point on each line corresponds to a different number density of the fluid and matrix particles. For each line, the higher state points correspond to the same system, a particular particle number density, at an

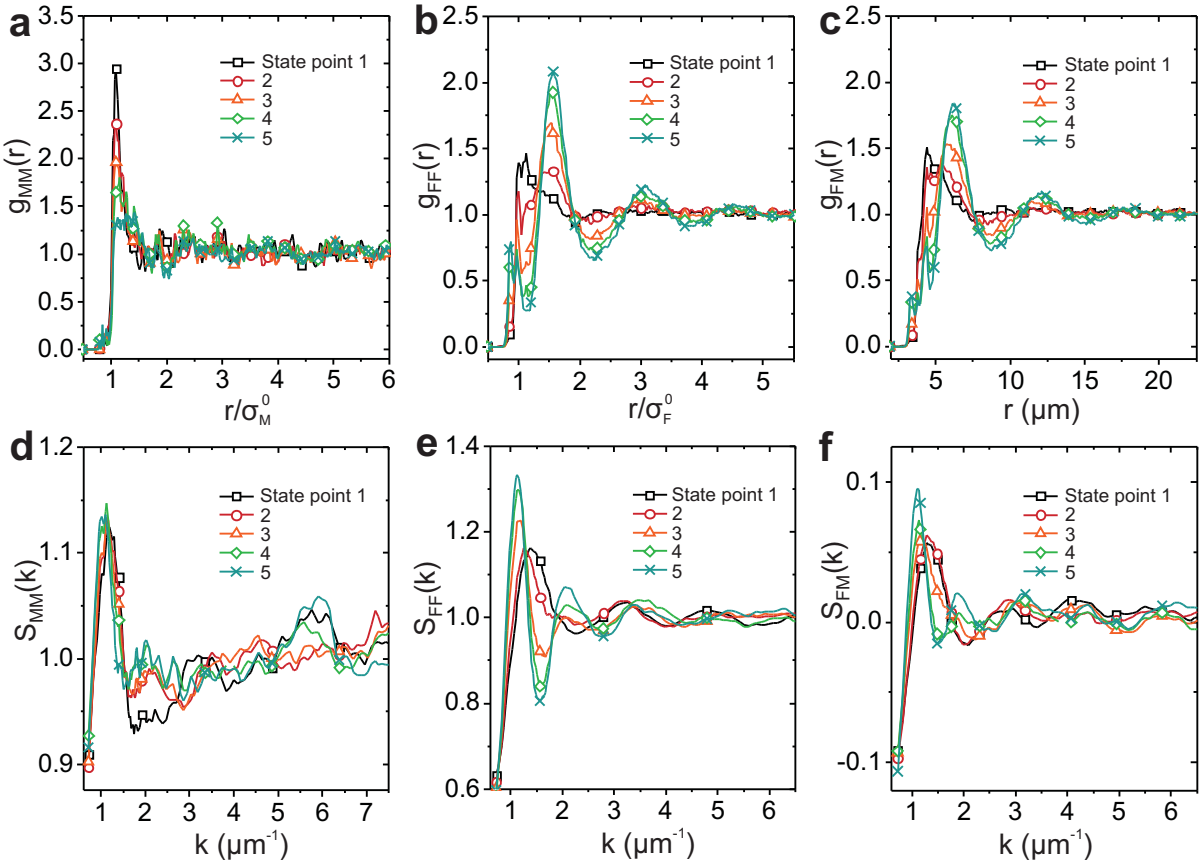

Figure 6.6: a-c) Radial distribution functions, $g(r)$, and d-e), structure factors, $S(k)$, for the fluid-fluid (FF), matrix-matrix (MM) and fluid-matrix (FM) for each state point along line 1.

increasing magnetic field (increasing effective area fraction). The behaviour of the fluid particles at each of the state points along these 3 lines across the state diagram is analysed.

6.4.1 Line 1: low ϕ_M

To characterise the structure of the system, the radial distribution functions, $g(r)$, and the static structure factors, $S(k)$, are shown in figure 6.6 for the 5 state points along line 1. The contributions to the static correlations in the system from the colloidal particles combinations of fluid-fluid (FF), matrix-matrix (MM) and fluid-matrix (FM) are shown for each state point. Importantly, $g_{MM}(r)$ and $S_{MM}(k)$ remain the same as a function of state point along line 1 even though the effective matrix area fraction increases. This clearly shows that the actual structure of the matrix remains fixed. These static correlations display the lack of long range order in the

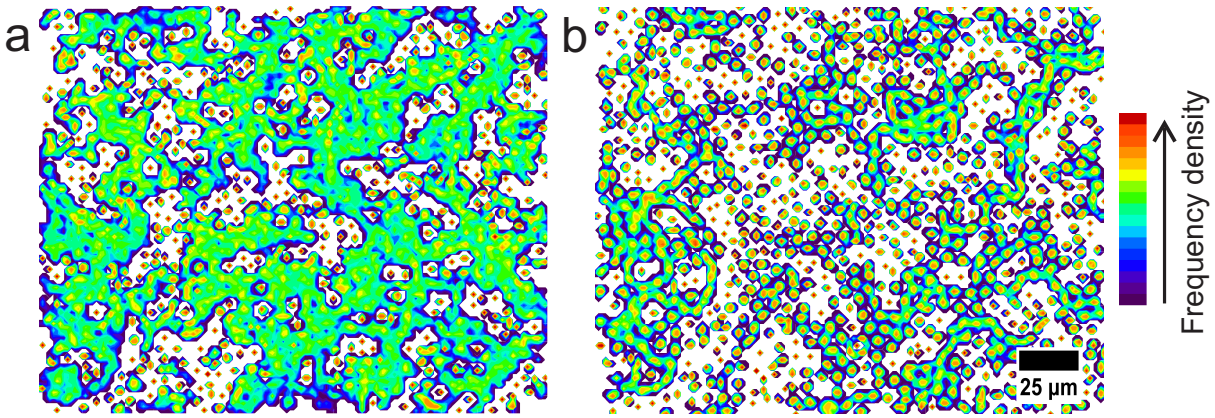

Figure 6.7: 2D histograms of the colloidal particle positions over an hour for a) state point 1 and b) state point 5 along line 1.

matrix and indicate that the matrix configurations have a largely random structure.

As can be seen in $g_{FF}(r)$ and $S_{FF}(k)$ in figure 6.6, the static correlations between the fluid particles changes significantly as a function of state point along line 1. The fluid particles display a gradual change from a random liquid structure at state point 1 to a more ordered liquid-like structure at state point 5. Here, although there is significantly more structure, there is no long range order or crystallinity as the peaks remain smooth and decay after 20 µm. In addition, a pronounced gradual shift of the main first peak to greater distances (smaller k) is observed as a function of state point. The colloidal particles move sequentially further apart as a function of state point, i.e. magnetic field. The peaks in g_{FF} shift from that of the small particle diameter to a greater distance, but importantly a small peak at $g(r) = \sigma_F^0$ remains, indicating that some particles are confined at the highest state point. The changes in $g(r)$ and $S(k)$ are gradual, suggesting that no phase transition occurs. The total contributions to the static correlation function are also shown in figure 6.6 for comparison.

The 2D histograms in figure 6.7 display the distributions of the fluid and matrix colloidal particle positions over 3600 s for a configuration in state point 1 and 5. The level of particle movement observed between the two state points is strongly contrasting. The fluid nature of much of the structure in state point 1, and the more confined dynamics in state point 5, are clearly evident. Note that only one example is shown for each state point in figure 6.7 and all results are averaged over multiple datasets.

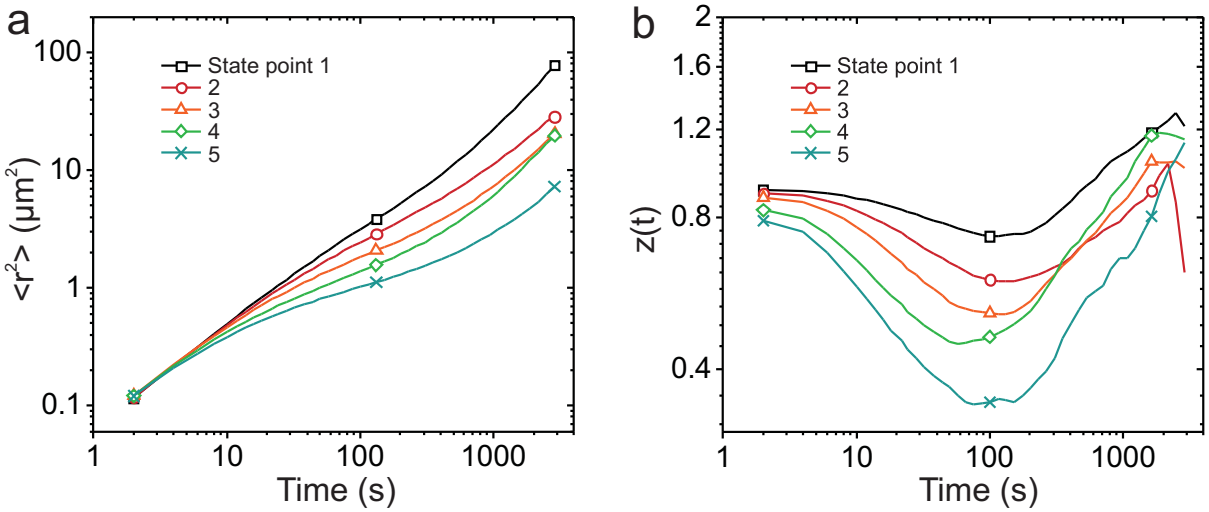

Figure 6.8: a) Mean square displacements and b) logarithmic derivatives for the fluid particles relating to state points 1 to 5 on line 1.

The static correlation functions and the 2D histograms imply that a significant change in the behaviour of the fluid particles occurs along line 1, despite no phase transition being observed. To further characterise the behaviour of the fluid, the single particle dynamics are now analysed. The mean square displacements (MSD) and the logarithmic derivatives for all state points along line 1 are shown in figure 6.8. The dynamics of the fluid at state point 1 are diffusive at short times before becoming slightly sub-diffusive at long times. Increasing the effective area fractions of the matrix and fluid particles via the external magnetic field, i.e. moving the system through state points 1 to 5, is accompanied by a clear slowing down of the fluid dynamics. The behaviour of the particles constituting the fluid at state point 5 is highly sub-diffusive reaching an exponent of 0.35. The minimum in the exponents in figure 6.8b are all around 100 s, before the MSD returns to more diffusive behaviour at long times. This is behaviour typical of a supercooled liquid; after the initial diffusive period, the fluid particles are impeded at intermediate times by the cage of neighbouring particles and show sub-diffusive behaviour, before at long times the MSD returns to diffusive behaviour again. Note that there is no clear exponent over a long time-scale suggesting that the normal type B glass transition scenario dominates and that normal cage breaking is the main mechanism at long times (illustrated by the variability in the exponent $z(t)$ over long times in the logarithmic derivative, figure 6.8b).

To further probe the characteristic time and length scales present along line 1, the self

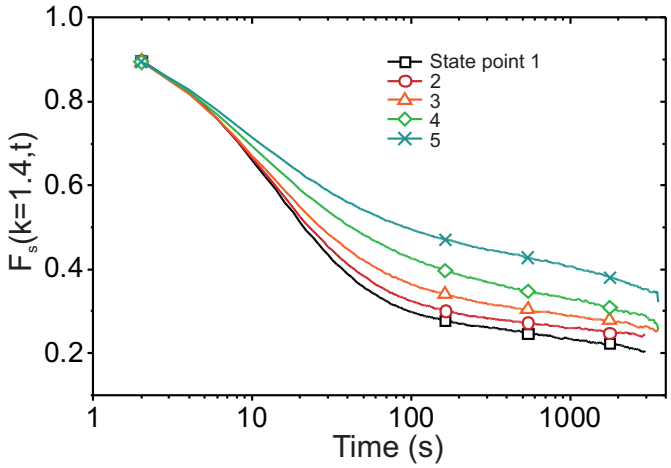

Figure 6.9: Self part of the intermediate scattering function for the fluid particles relating to state points 1 to 5 along line 1. The system is probed at $k = 1.4$ μm^{-1}.

part of the intermediate scattering function (ISF) is computed, see figure 6.9. The ISF and MSD give complimentary information as the ISF is sensitive to the slow particles in the system, unlike the MSD which is more sensitive to the fast particles. The ISF displays how the amount of relaxation reduces, i.e. the plateau height increases, as the state points are traversed from 1 to 5. The increasing effective area fractions of both the fluid and the matrix causes the fluid particles to become more confined, see figure 6.7. A proper plateau is not formed in the ISF as extensive cage trapping does not occur, the particles are instead only slowed by their cages, this is also observed by the lack of a plateau in the MSD, see figure 6.8a. The 2D histograms, figure 6.7, and the ISF suggest that there are some small subsets of particles that do not fully relax and are therefore confined. These confined particles prevent the ISF from decaying fully, for comparison (not shown) the ISF of the 10% most mobile particles from state point 1 decays to zero after 100 s.

6.4.2 Line 2: intermediate ϕ_M

Line 2 through the state diagram, see figure 6.5b, occurs at a higher matrix and a slightly lower fluid particle density to that of line 1. According to the theoretical work by Krakoviack [268], a change away from the standard type B glass transition behaviour seen in line 1, to that which will include more character of a type A transition may be expected. The static correlations present in the system for line 2 as a function of state point are shown in figure 6.10. Likewise

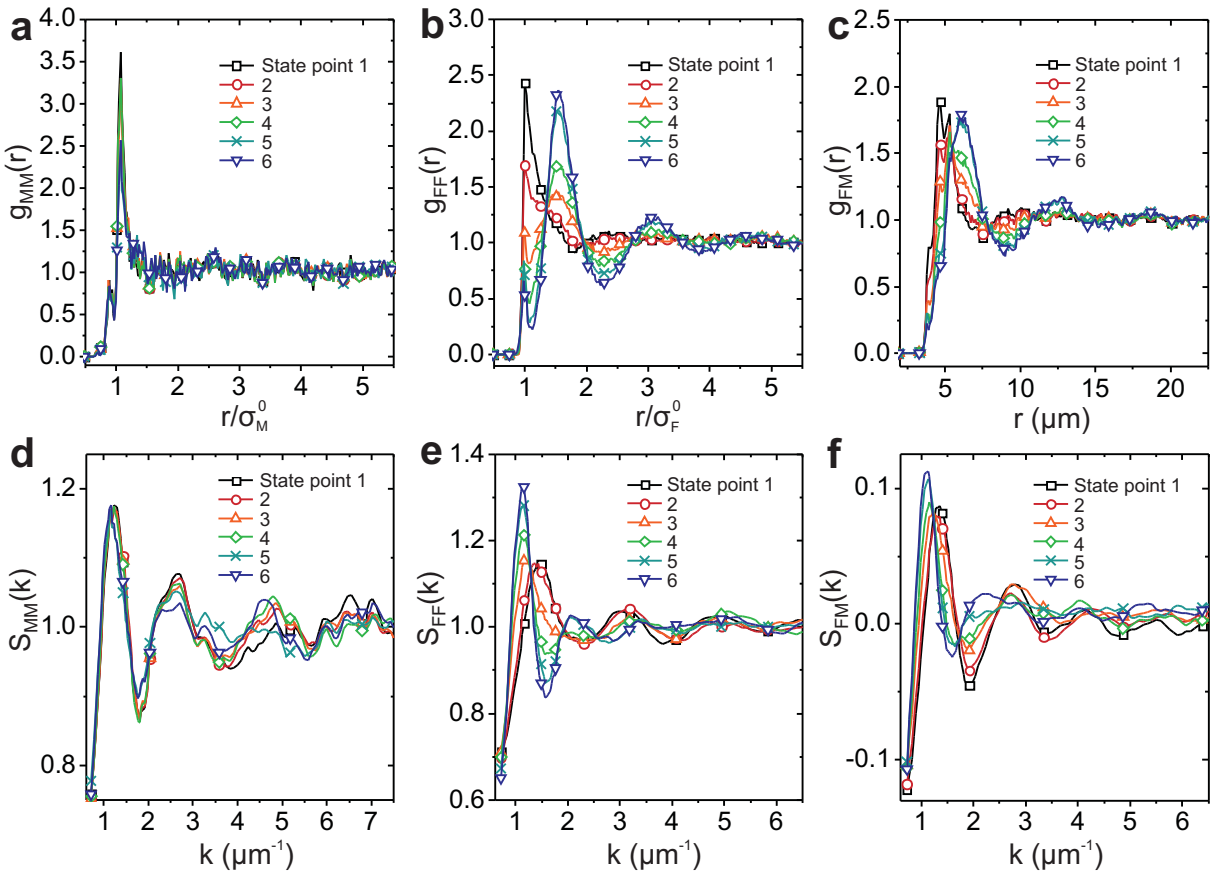

Figure 6.10: a-c) Radial distribution functions, $g(r)$, and d-e), structure factors, $S(k)$, for the fluid-fluid (FF), matrix-matrix (MM) and fluid-matrix (FM) for each state point along line 2.

to the case in line 1, the static correlations between the matrix particles display no long range ordering, consistent with them forming a disordered matrix. The structural trends present in the fluid as shown by $g(r)$ and $S(k)$, are similar to those seen in line 1, except that the long range ordering effects in the fluid particles are somewhat more pronounced. Between state points 1 and 6, a shift in the nearest neighbour peak is observed from close to that of the fluid particle diameter, to a distance of $1.5\sigma_F^0$. This occurs as the fluid particles become more evenly spaced within the voids formed by the matrix due to the increasing repulsive interactions.

The 2D histograms shown in figure 6.11 illustrate the changes in the distributions of the particles along line 2 for state points 1 and 6. The dynamics in state point 1 are clearly more liquid-like in nature with a great deal of movement. In contrast, state point 6 displays reduced particle dynamics with some particles becoming more confined, in a similar way to in line 1.

The mean square displacements of the fluid particles along line 2 are shown in figure 6.12,

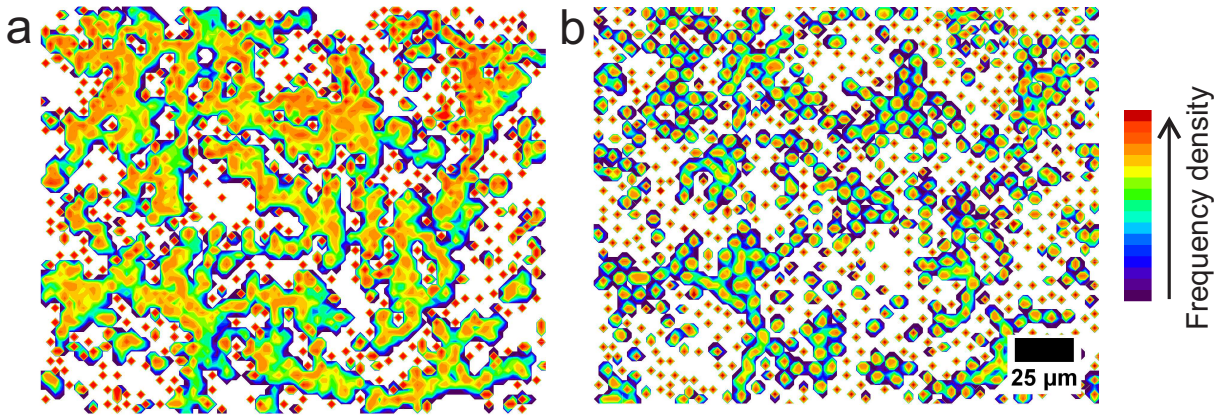

Figure 6.11: 2D histograms of the colloidal particle positions over an hour for a) state point 1 and b) state point 6 along line 2.

along with their respective logarithmic derivatives. A significant slowing down of the fluid particle dynamics is observed as the effective free area fraction decreases. State point 1 is nearly fully diffusive, in contrast, state point 6 displays strongly sub-diffusive behaviour reaching an exponent of $z = 0.25$. The upswing in the MSD at long times does not see a return to full diffusive behaviour, as in line 1. The increased matrix density along line 2 prevents the fluid particles from moving freely, creating the long time sub-diffusive behaviour seen by the lower exponents in figure 6.12b.

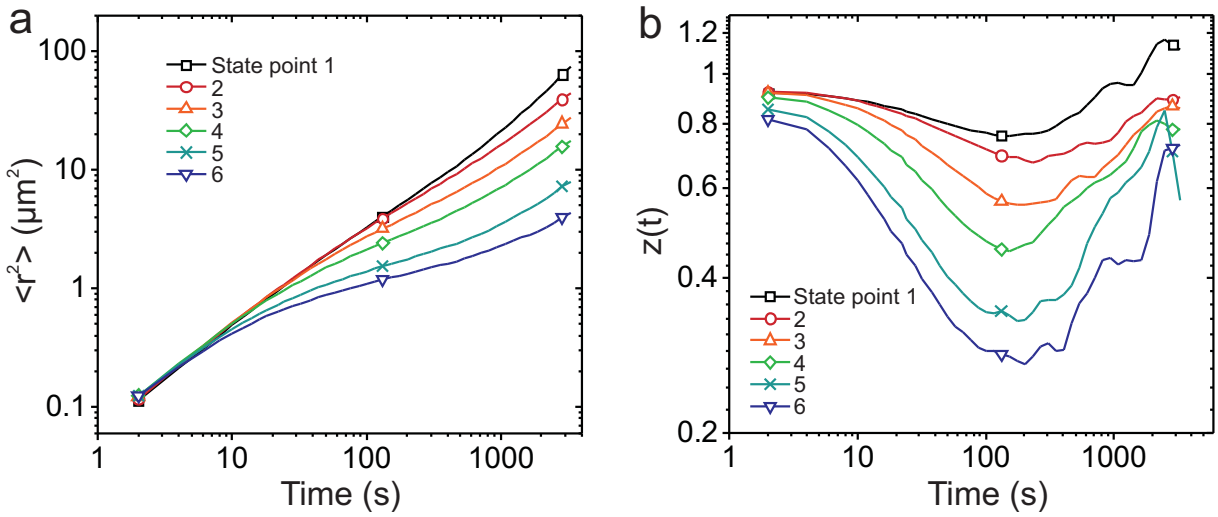

Figure 6.12: a) Mean square displacements and b) logarithmic derivatives for the fluid particles relating to state points 1 to 6 on line 2.

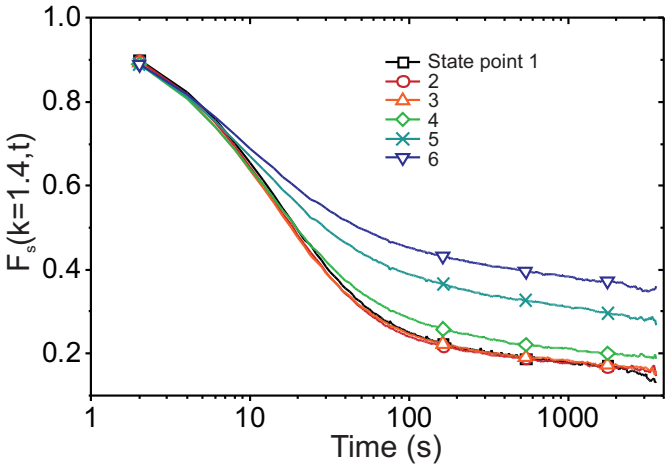

Figure 6.13: Self part of the intermediate scattering function for the fluid particles relating to the state points 1 to 6 on line 2. The system is probed at $k = 1.4$ μm^{-1}.

The ISFs for all state points along line 2 are shown in figure 6.13. These appear very similar to those seen in line 1, in fact the total packing fractions are also very similar, for the corresponding points along lines 1 and 2. The reduced fluid and increased matrix density of state points in line 2 causes the marginally faster initial relaxation before a slightly slower long time relaxation. This indicates that the matrix is having a slightly greater effect on the fluid particle dynamics than it did in line 1. A few more fluid particles become trapped in voids created by the matrix, which then prevent the ISF decaying fully. Despite this, the behaviour of the fluid particles as a function of increasing state point in the MSD and ISF are similar to that characteristic of supercooled liquids. Hence, the normal type B glass transition is still the dominant mechanism along line 2 [35, 247].

6.4.3 Line 3: high ϕ_M

The spatial correlators, $g(r)$ and $S(k)$, are shown for state points along line 3 in figure 6.14. The static correlations in the matrix, $g_{MM}(r)$, display the emergence of a weak 2^{nd} and 3^{rd} peak, which is expected for higher ϕ_M. Despite this, the matrix still appears to be significantly disordered and exhibits a random structure, see figure 6.15. The spatial correlations between the fluid particles display more structure than those observed in lines 1 and 2. The changes in $g_{FF}(r)$ and $S_{FF}(k)$ as a function of state point along line 3 for the fluid particles are minimal. The positions of the peaks do not change, only marginally the relative heights, and there is

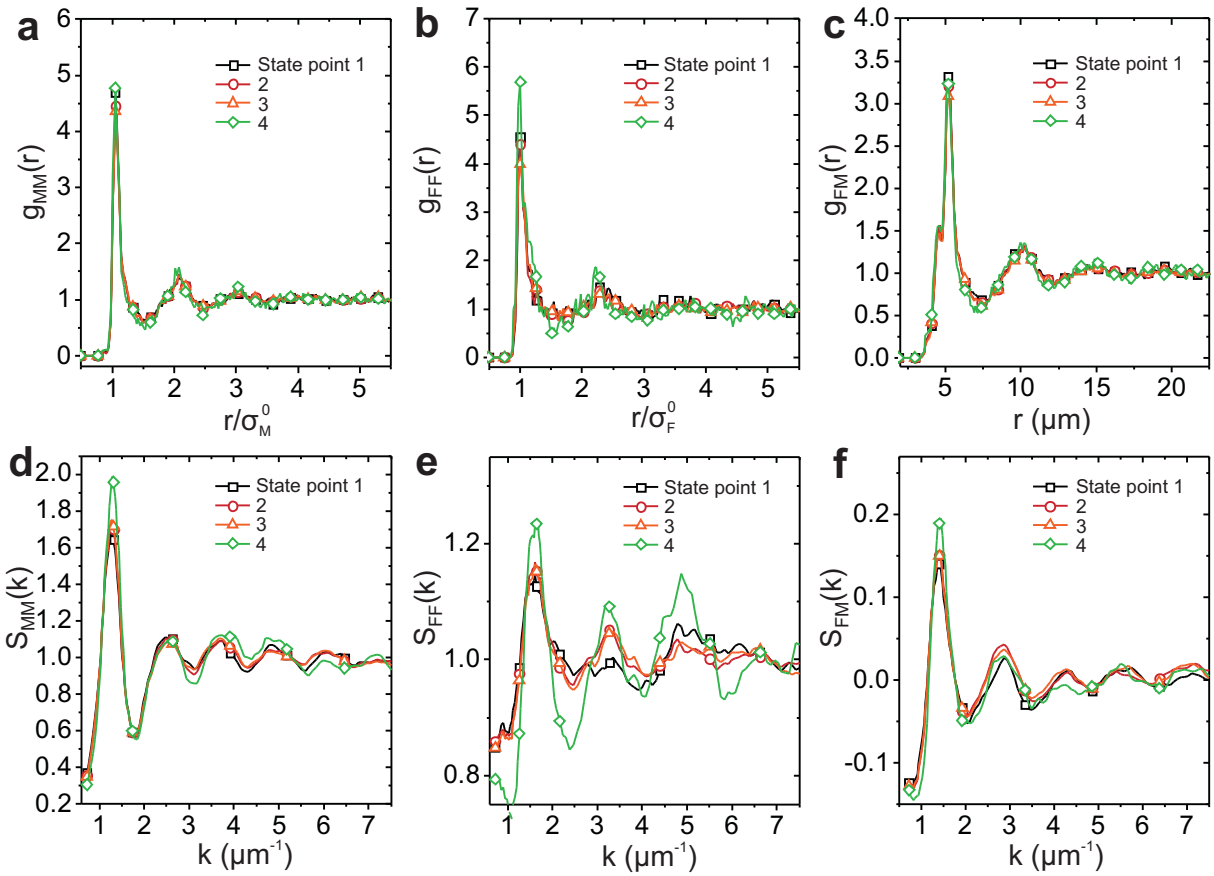

Figure 6.14: a-c) Radial distribution functions, $g(r)$, and d-e), structure factors, $S(k)$, for the fluid-fluid (FF), matrix-matrix (MM) and fluid-matrix (FM) for each state point along line 3.

also a great reduction in the amount of long range order present in the fluid. These structural correlators indicate that the positions of the fluid particles within the matrix are such that increasing the magnetic field has little effect on their structure. This suggests that most of the fluid particles are highly confined and trapped in unconnected pores.

Typical 2D histograms for state point 1 and 4 along line 3 are shown in figure 6.15. Likewise to the static correlation functions, these histograms display completely different behaviour to that observed in lines 1 and 2. At state point 1, the fluid particles display limited motion, which then greatly decreases still more at state point 4. The high ϕ_M appears to be causing many of the fluid particles to become highly confined even at low magnetic field.

The single particle dynamics are analysed in terms of the MSD and the corresponding logarithmic derivatives in figure 6.16. The fluid particle dynamics appear significantly different

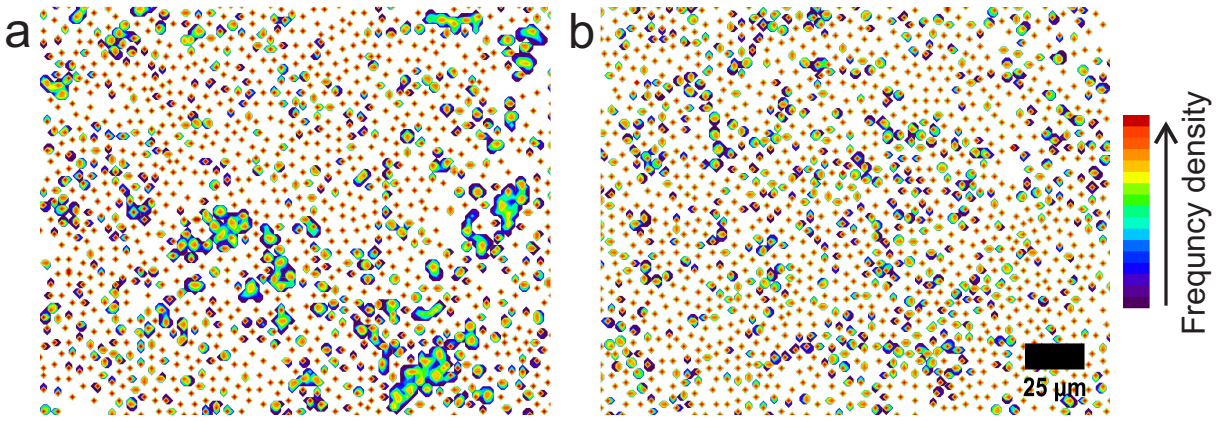

Figure 6.15: 2D histograms of the colloidal particle positions over an hour for a) state point 1 and b) state point 4 along line 3.

to those seen in lines 1 and 2. After the initial diffusive period, the dynamics become sub-diffusive at fairly constant values for significant lengths of time. This long time sub-diffusive behaviour is clearly anomalous and not what is expected in the normal type B glass transition. The localisation effects characteristic in the type A glass transition are more prevalent. Noticeable from the logarithmic derivatives in figure 6.16b is that the exponents at long times are also significantly smaller than those seen in the other lines on the state diagram. In addition, the magnitude of the fluid particle movement is much suppressed compared to that of the other

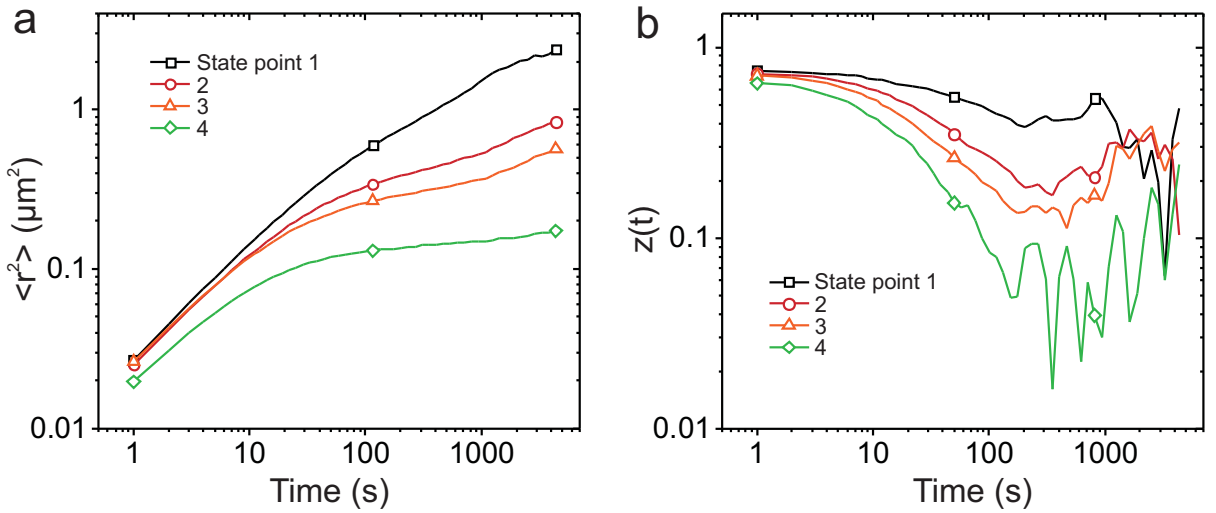

Figure 6.16: a) Mean square displacements and b) logarithmic derivatives for the fluid particles relating to the state points 1 to 4 on line 3.

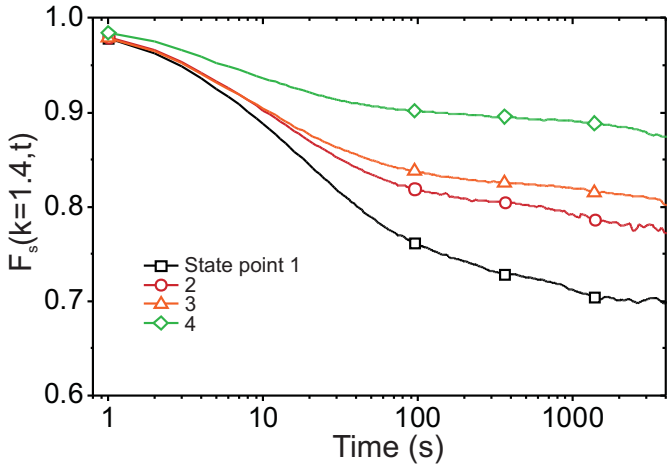

Figure 6.17: Self part of the intermediate scattering function for the fluid particles relating to the state points 1 to 4 on line 3. The system is probed at $k = 1.4$ μm^{-1}.

lines: the average MSD at long times only reaches 1.5 μm^2 (compared to ~ 10 μm^2 in lines 1 and 2). Although the behaviour of the fluid along line 3 is clearly different to the other lines, definite results, i.e. analysing critical long time exponents are not possible due to the statistics.

The ISFs for state points along line 3 are shown in figure 6.17. As the matrix density increases from state point 1 to 4, the amount of relaxation in the ISF greatly decreases. The amount of decay is minimal in comparison to that seen in lines 1 and 2 (figure 6.9 and figure 6.13). This indicates that a greater proportion of the fluid particles have become localised in the matrix, preventing the decay in the dynamics. The fluid particle dynamics are more similar to that expected in a localisation transition where the fluid particles become trapped in unconnected pores of the matrix. In a type B glass former, cage rearrangement is possible, however in this system with a fixed matrix, the obstacles cannot move and the fluid dynamics remain localised, even at long times. This prevents the secondary long time diffusive period and results in a gradual change in the dynamic correlators. These dynamics indicate that the fluid particle dynamics along line 3 are more akin to those seen in a type A localisation glass transition.

6.4.4 Type B versus Type A glass transition

Both the static correlations and the single particle dynamics of the fluid particles for different areas of the state diagram have been analysed. A general shift in behaviour from that more similar to a type B glass forming liquid in lines 1 and 2, to dynamics most similar to type A

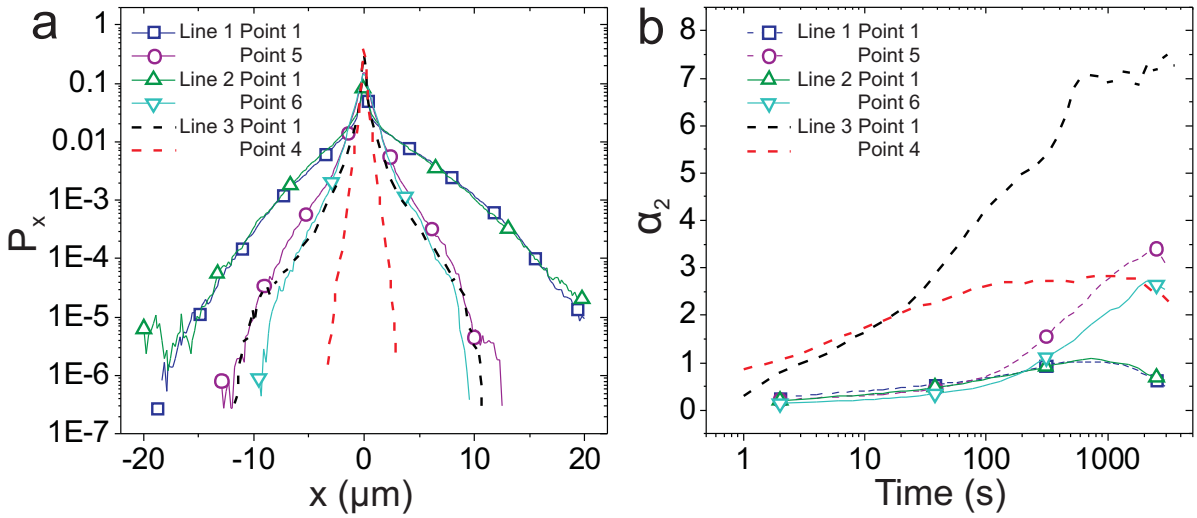

Figure 6.18: a) Self part of the van Hove correlation function at $t = 1000$ s in the x direction for the first and last state point along each line. b) Non-Gaussian parameter, α_2, in the x direction as a function of time for the first and last state point along each line.

in line 3 are observed. The cuts through the state diagram are diagonal so all the behavioural changes seen along the lines 1, 2 and 3 are likely to be a mixture to different extents of both type B and A glass transitions. This is evidenced by the ISF not decaying to zero for any of the lines, even in line 1 which is expected to represent the most type B-like behaviour. The ISF is more sensitive to the slower particles than the MSD, which in lines 1 and 2 returned to diffusive or nearly diffusive behaviour. This suggests that even at the lowest state points along each line there are subsets of particles that are caged and have greatly different mobilities.

So far, the correlators analysed have been averaged over all the fluid particles. Now the level of heterogeneity present in the fluid dynamics is investigated by computing the self part of the van Hove correlation function and the non-Gaussian parameter, see figure 6.18. The trends are shown for correlations in the x direction only, as the behaviour is not direction dependent.

The self part of the van Hove correlation function, $G_s(x,t)$, is shown in figure 6.18a for the first and last state points along each line, 1, 2 and 3, for time, t = 1000 s. The non-Gaussian parameter (α_2) is shown in figure 6.18b for the first and last state points along each line as a function of time. Both $G_s(x,t)$ and α_2 indicate that the dynamics of the fluid particles are generally quite heterogeneous. The trends in $G_s(x,t)$ are as expected: the widths of the distributions in $G_s(x,t)$ are greater for the lowest state points (lower ϕ_M and ϕ_F) than the

highest state points along each line. This is consistent with the MSDs, which observed a slowing down of the fluid dynamics as a function of state point along each line in the state diagram.

Comparing the level of dynamical heterogeneity between the lines, (α_2 in figure 6.18) shows that for line 3, the dynamics are significantly more non-Gaussian than for the other lines. However, observation of the tails of the distributions in $G_s(x,t)$ for line 3 shows that they are reduced in width compared to lines 1 and 2, consistent with the MSD and the $z(t)$ exponent being a lot smaller. This increased non-Gaussian behaviour stems from the large subset of particles which are very highly localised ($\Delta x \approx 0$) and therefore contribute to the very steep central peak in $G_s(x,t)$ for line 3, which then increases α_2, see figure 6.18.

Interestingly, the trends in α_2 are not so clear cut. In lines 1 and 2, as ϕ_M and ϕ_F increase, the fluid particle dynamics become increasingly heterogeneous. At low packing fractions along these lines, few particles are caged and therefore most particles have similar behaviour. At higher packing fractions, many of these particles become caged, the extent of which varies and hence the dynamics become more heterogeneous. This increase in dynamical heterogeneity is that expected as a fluid approaches a normal type B glass transition. In contrast, line 3 displays the opposite trend. In line 3 the particle dynamics become more homogeneous at higher ϕ_M and ϕ_F. At low packing fractions the system is very heterogeneous with most particles highly localised, but with a small mobile subset. On increasing the packing fraction, this mobile subset then becomes localised and the overall fluid particle dynamics become more homogeneous. This behaviour suggests that the type A glass transition is the dominant mechanism along line 3 and all the particle become highly localised in the matrix.

6.5 Conclusions

A 2D system has been created where large particles form a fixed random matrix around which smaller particles, the 'fluid', are able to diffuse. All the colloidal particles in the system are super-paramagnetic, hence, via increasing an external magnetic field, lines across a state diagram of the effective area fraction of the matrix versus that of the fluid particles were scanned. The behaviour of the fluid was mapped along three lines across the state diagram, lines 1, 2 and 3. In line 1, at low matrix density, the dynamic correlators of the MSD and self part of the

ISF indicated behavior similar to the early stages of a type B glass transition. The dynamics of the fluid particles become increasingly non-Gaussian at large times as the total area fraction increased. Line 2 started at a higher matrix and lower fluid density to line 1, and observed very similar type B supercooled behaviour, but with a less pronounced upswing in the MSD. This suggests that the fluid particles here are slightly more confined within the matrix and indicates the weak presence of some dynamics characteristic of a type A localisation glass transition. Line 3 through the state diagram started at an even higher matrix and lower fluid area fraction. A more gradual one step change in the dynamic correlators was observed, indicative of a type A glass transition. The van Hove correlation function displayed that a large set of particles had $\Delta x \approx 0$, and therefore the majority of the particles were highly localised even at long times. Qualitatively, good agreement is observed with both the mode coupling theory [34] and the molecular dynamics simulations [35, 247] of a hard sphere fluid in a 3D hard sphere random matrix. Thus also illustrating the similarities between 2D and 3D systems in terms of both the nature of the transitions and the state diagram.

In order to further characterise the system, the aims are to: a) decompose the system into dynamical subsets and characterise their mobility to get a better insight into the localised particles. b) characterise the matrix further by computing the area fraction of the percolating void and the average pore size.

Acknowledgments

This work is done in collaboration with Jürgen Horbach and Dirk Aarts.

Summary

In this thesis, the behaviour of colloidal particles in two-dimensional (2D) systems is studied, in particular grain boundaries and different types of confinement. The intrinsic softness and the tunable interactions make colloidal systems ideal for manipulation with optical tweezers and external magnetic fields whilst imaging with optical video microscopy.

In chapter 1, colloidal systems were introduced along with their basic characteristics, including Brownian motion, their intrinsic softness and the fact that they can readily be observed using standard optical microscopy, inherent to their timescales being on the order of seconds. In chapter 2, the colloidal model system used in this thesis, the background behind the experimental set-up and the experimental procedures were introduced. The construction of an optical tweezing set-up in combination with an optical microscope was described which allowed manipulation and simultaneous imaging of the single colloidal particles.

In chapter 3 a quasi-1D grain boundary in a 2D colloidal crystal was experimentally analysed. The fluctuations of the grain boundary were described by both spatial and dynamical correlation functions of the interfacial profile. Real space expressions for these correlation functions were derived from capillary wave theory. Good agreement was found for the values of the key parameters that define the interface, the interface stiffness and mobility, from both the real and Fourier space methodologies. In addition, a method of extracting the interfacial mobility from analysis of the 1D random walk of the average interface position, as suggested by recent simulations, was experientially verified providing good agreement with the other methods.

The grain boundary theme was continued in chapter 4, but this time rather than analysing the interfacial fluctuations, the dynamics of the colloidal particles that make up the grain bound-

ary were studied. It has long been hypothesised and also recently suggested in simulation, that particles constituting grain boundaries can exhibit dynamics similar to supercooled liquids. The mean square displacements of the grain boundary particles demonstrated a pronounced plateau at intermediate times followed by a increase at longer times. Furthermore, the grain boundary particle dynamics were found to be highly heterogeneous and chains of cooperatively moving particles were observed. This observed dynamical behaviour, including consistent time evolution of cluster sizes, diffusive particle dynamics and non-Gaussian distributions, is characteristic of the particles in a supercooled liquid.

Chapter 5 addressed the effect of imposing 2D pentagonal confinement on the structure and dynamics of spherical super-paramagnetic colloidal particles. An array of super-paramagnetic colloidal particles were fixed in a pentagon shape by an optical tweezer. The state of the system was characterised by Γ, which is a function of both the particle number density and the magnetic field. In the first section, the behaviour of a 16 particle system, one that is commensurate to the confining geometry was studied as the magnetic field was reduced. The particle dynamics and orientational order displayed a gradual transition from a crystalline to confined liquid like state at low interaction strength. In the second section, rather than varying the magnetic field, the number of confined particles was increased from 10 to 21. Here, in contrast to the first section, almost periodic trends in the orientational order of the system were observed. These were coupled with an incoherent fluctuation in the dynamical behaviour of the confined particles. The symmetry and orientational order in the packing arrangements greatly affected the particle dynamics and the system was highly sensitive to the number of confined particles. Re-entrant orientational ordering and fluctuating levels of dynamical behaviour were observed as the confined number density increased.

In chapter 6 another form of 2D confinement was analysed: small colloidal particles, the 'fluid', were free to diffuse amongst a 2D fixed array of large particles, the 'matrix'. All the colloidal particles in the system were super-paramagnetic, hence, via increasing an external magnetic field, in addition to varying the particle number densities, three lines across a state diagram of the effective area fraction of the matrix versus that of the fluid particles were scanned. In line 1 at low matrix density, the dynamic correlators of the fluid particles, including the mean square displacement, displayed behaviour indicative of the early stages of a 'normal' glass

transition. Across line 2 at intermediate matrix density, the dynamics of the fluid appeared to be a mixture of that associated with both a 'normal' and a localisation glass transitions, though still dominated by the 'normal' mechanism. In line 3 at high matrix density, the fluid particle dynamics became highly localised, trapped within unconnected pores in the matrix. This lead to indications of a localisation transition as expected at high matrix packing fractions. In all lines, the dynamics were found to be very heterogeneous. These experimental results demonstrate good agreement with both recent theory and simulations.

Bibliography

[1] D. Fennell Evans and H. Wennerström. *The Colloidal domain where physics, chemistry, biology and technology meet*. Wiley-VCH, 2nd edition, 1999.

[2] C. A. Murray and D. G. Grier. Video microscopy of monodisperse colloidal systems. *Annu. Rev. Phys. Chem.*, 47:421–462, 1996.

[3] T. Graham. Liquid diffusion applied to analysis. *Phil. Trans. Roy. Soc.*, 151:183–224, 1861.

[4] H. D. Goff. Colloidal aspects of ice cream - A review. *Int. Dairy J.*, 7(6-7):363–373, 1997.

[5] T. F. Tadros. *Colloids in paints*, volume 6 of *Colloids and interface science*. Wiley-VCH, 2010.

[6] J. M. Martin and N. Ohmae. *Colloidal Lubrication: General Principles*, pages 1–13. John Wiley and Sons, Ltd, 2008.

[7] A. G. Olabi and A. Grunwald. Design and application of magneto-rheological fluid. *Mater. and Des.*, 28(10):2658–2664, 2007.

[8] C. Graf and A. van Blaaderen. Metallodielectric colloidal core-shell particles for photonic applications. *Langmuir*, 18(2):524–534, 2002.

[9] A. Einstein. Über die von der molekularkinetischen theorie der wärme geforderte bewegung von in ruhenden flüssigkeiten suspendierten teilchen. *Ann. Phys.*, 17:549–560, 1905.

[10] M. D. Haw. Colloidal suspensions, brownian motion, molecular reality: a short history. *J. Phys.-Condes. Matter*, 14(33):7769–7779, 2002.

[11] P. Habdas and E. R. Weeks. Video microscopy of colloidal suspensions and colloidal crystals. *Curr. Opin. Colloid Interface Sci.*, 7(3-4):196–203, 2002.

[12] P. Holmqvist, J. K. G. Dhont, and P. R. Lang. Anisotropy of Brownian motion caused only by hydrodynamic interaction with a wall. *Phys. Rev. E*, 74(2):021402, 2006.

[13] N. J. Wagner and J. F. Brady. Shear thickening in colloidal dispersions. *Phys. Today*, 62(10):27–32, 2009.

[14] W. C. K. Poon. Colloids as big atoms. *Science*, 304(5672):830–831, 2004.

[15] A. Yethiraj. Tunable colloids: control of colloidal phase transitions with tunable interactions. *Soft Matter*, 3(9):1099–1115, 2007.

[16] P. N. Pusey and W. van Megen. Phase behaviour of concentrated suspensions of nearly hard colloidal spheres. *Nature*, 320(6060):340–342, 1986.

[17] X. Ye, T. Narayanan, P. Tong, J. S. Huang, M. Y. Lin, B. L. Carvalho, and L. J. Fetters. Depletion interactions in colloid-polymer mixtures. *Phys. Rev. E*, 54(6):6500–6510, 1996.

[18] U. Gasser, C. Eisenmann, G. Maret, and P. Keim. Melting of crystals in two dimensions. *Chem. Phys. Chem.*, 11(5):963–970, 2010.

[19] G. Fonnum, C. Johansson, A. Molteberg, S. Morup, and E. Aksnes. Characterisation of Dynabeads by magnetization measurements and Mössbauer spectroscopy. *J. Magn. Magn. Mater.*, 293:41, 2005.

[20] V. Blickle, D. Babic, and C. Bechinger. Evanescent light scattering with magnetic colloids. *Appl. Phys. Lett.*, 87(10):101102, 2005.

[21] M. Ravnik, G. P. Alexander, J. M. Yeomans, and S. Žumer. Three-dimensional colloidal crystals in liquid crystalline blue phases. *Proc. Natl. Acad. Sci. USA*, 108(13):5188–5192, 2011.

[22] J. R. Moffitt, Y. R. Chemla, S. B. Smith, and C. Bustamante. *Recent advances in optical tweezers*, volume 77 of *Annu. Rev. Biochem.*, pages 205–228. Annual Reviews, Palo Alto, 2008.

[23] L. J. Moore, R. D. Dear, M. D. Summers, R. P. A. Dullens, and G. A. D. Ritchie. Direct observation of grain rotation-induced grain coalescence in two-dimensional colloidal crystals. *Nano Lett.*, 10(10):4266–4272, 2010.

[24] C. Jin-Ho, K. Soon-Jae, and P. Gyeong-Su. High-T_c superconductors in the two-dimensional limit: $[(Py{-}C_nH_{2n+1})_2HgI_4]{-}Bi_2Sr_2Ca_{m-1}Cu_mO_y$ (m = 1 and 2). *Science*, 280(5369):1589–15921592, 1998.

[25] H. Gao, L. Zhang, W. D. Nix, C. V. Thompson, and E. Arzt. Crack-like grain-boundary diffusion wedges in thin metal films. *Acta Mater.*, 47(10):2865–2878, 1999.

[26] A. Shah, J. Meier, A. Buechel, U. Kroll, J. Steinhauser, F. Meillaud, H. Schade, and D. Dominè. Towards very low-cost mass production of thin-film silicon photovoltaic (PV) solar modules on glass. *Thin Solid Films*, 502(1-2):292–299, 2006.

[27] T. Aste and D. Weaire. *The persuit of perfect packing.* IoP Publishing, 2000.

[28] U. Gasser. Crystallization in three- and two-dimensional colloidal suspensions. *J. Phys.-Condes. Matter*, 21(20):203101, 2009.

[29] D. G. A. L. Aarts, M. Schmidt, and H. N. W. Lekkerkerker. Direct visual observation of thermal capillary waves. *Science*, 304(5672):847–850, 2004.

[30] J.J. Hoyt, Z.T. Trautt, and M. Upmanyu. Fluctuations in molecular dynamics simulations. *Math. Comput. Simul.*, 80:1382–1392, 2010.

[31] W. Rosenhain and D. Ewen. The intercrystalline cohesion of metals. *J. Inst. Met.*, 10:119, 1913.

[32] H. Zhang, D. J. Srolovitz, J. F. Douglas, and J. A. Warren. Grain boundaries exhibit the dynamics of glass-forming liquids. *Proc. Natl. Acad. Sci. USA*, 106(19):7735–7740, 2009.

[33] G. Laugel, J. Arichi, P. Bernhardt, M. Molière, A. Kiennemann, F. Garin, and B. Louis. Preparation and characterisation of metal oxides supported on SBA-15 as methane combustion catalysts. *C. R. Chimie*, 12(67):731–739, 2009.

[34] V. Krakoviack. Liquid-glass transition of a fluid confined in a disordered porous matrix: A Mode-Coupling theory. *Phys. Rev. Lett.*, 94:065703, 2005.

[35] J. Kurzidim, D. Coslovich, and G. Kahl. Single-particle and collective slow dynamics of colloids in porous confinement. *Phys. Rev. Lett.*, 103(13):138303, 2009.

[36] T. Bauer, F. Höfling, T. Munk, E. Frey, and T. Franosch. The localization transition of the two-dimensional Lorentz model. *Eur. Phys. J.-Spec. Top.*, 189(1):103–118, 2010.

[37] P. W. Bridgman. Change of phase under pressure. i. The phase diagram of eleven substances with especial reference to the melting curve. *Phys. Rev.*, 3(3):153–203, 1914.

[38] W. W. Wood and J. D. Jacobson. Preliminary results from a recalculation of the Monte Carlo equation of state of hard spheres. *J. Chem. Phys.*, 27(5):1207–1208, 1957.

[39] B. J. Alder and T. E. Wainwright. Phase transition for a hard sphere system. *J. of Chem. Phys.*, 27(5):1208–1209, 1957.

[40] W. G. Hoover and F. H. Ree. Melting transition and communal entropy for hard spheres. *J. Chem. Phys.*, 49(8):3609–3617, 1968.

[41] X. Batlle and A. Labarta. Finite-size effects in fine particles: magnetic and transport properties. *J. Phys. D-Appl. Phys.*, 35(6):R15–R42, 2002.

[42] D. J. Griffiths. *Introduction to Electrodynamics*. Prentice-Hall, Upper Saddle River, 3rd edition, 1999.

[43] W. Sutherland. Dynamical theory of diffusion for non-electrolytes and the molecular mass of albumin. *Phil. Mag.*, 9:781–785, 1905.

[44] D. Drung, C. Assmann, J. Beyer, A. Kirste, M. Peters, F. Ruede, and T. Schurig. Highly sensitive and easy-to-use SQUID sensors. *IEEE Trans. Appl. Supercond.*, 17(2):699–704, 2007.

[45] H. C. King. *The history of the telescope*. Courier Dover, 2003.

[46] A. Ashkin. Acceleration and trapping of particles by radiation pressure. *Phys. Rev. Lett.*, 24(4):156–159, 1970.

[47] A. Ashkin and J. M. Dziedzic. Optical levitation by radiation pressure. *Appl. Phys. Lett.*, 19(8):283–285, 1971.

[48] A. Ashkin, J. M. Dziedzic, J. E. Bjorkholm, and S. Chu. Observation of a single-beam gradient force optical trap for dielectric particles. *Optics Lett.*, 11:288, 1986.

[49] A. Ashkin and J. M. Dziedzic. Optical trapping and manipulation of viruses and bacteria. *Science*, 235:1517, 1987.

[50] K. Svoboda and S. M. Block. Biological applications of optical forces. *Annu. Rev. Biophys. Biomolec. Struct.*, 23:247–285, 1994.

[51] K. O. Greulich and G. Pilarczyk. Laser tweezers and optical microsurgery in cellular and molecular biology. working principles and selected applications. *Cell. Mol. Biol.*, 44(5):701–710, 1998.

[52] H. Zhang and K. K. Liu. Optical tweezers for single cells. *J. R. Soc. Interface*, 5(24):671–690, 2008.

[53] R. W. Applegate, J. Squier, T. Vestad, J. Oakey, and D. W. M. Marr. Optical trapping, manipulation, and sorting of cells and colloids in microfluidic systems with diode laser bars. *Opt. Express*, 12(19):4390–4398, 2004.

[54] R. Andrew. Use of optical tweezers for colloid science. *J. Colloid Interface Sci.*, 262(1):55–59, 2003.

[55] D. G. Grier. Optical tweezers in colloid and interface science. *Curr. Opin. Colloid Interface Sci.*, 2(3):264–270, 1997.

[56] G. Dominguez-Espinosa, A. Synytska, A. Drechsler, C. Gutsche, K. Kegler, P. Uhlmann, M. Stamm, and F. Kremer. Optical tweezers to measure the interaction between poly(acrylic acid) brushes. *Polymer*, 49(22):4802–4807, 2008.

[57] M. Harada, M. Ishii, and H. Nakamura. Optically induced melting of colloidal crystals and their recrystallization. *H. Colloids Surf., B*, 56(1-2):220–223, 2007.

[58] D. G. Grier. A revolution in optical manipulation. *Nature*, 424(6950):810–816, 2003.

[59] Y. Harada and T. Asakura. Radiation forces on a dielectric sphere in the Rayleigh scattering regime. *Opt. Commun.*, 124:529, 1996.

[60] P. A. M. Neto and H. M. Nussenzveig. Theory of optical tweezers. *Europhys. Lett.*, 50(5):702–708, 2000.

[61] A. Mazolli, P. A. M. Neto, and H. M. Nussenzveig. Theory of trapping forces in optical tweezers. *Proc. R. Soc. London Ser. A-Math. Phys. Eng. Sci.*, 459(2040):3021–3041, 2003.

[62] A. Ashkin. Forces of a single-beam gradient laser trap on a dielectric sphere in the ray optics regime. *Biophysical Journal*, 61:569, 1992.

[63] K. Sasaki, M. Koshioka, H. Misawa, N. Kitamura, and H. Masuhara. Pattern-formation and flow-control of fine particles by laser-scanning micromanipulation. *Opt. Lett.*, 16:1463, 1991.

[64] C. Mio, T. Gong, A. Terray, and D. W. M. Marr. Design of a scanning laser optical trap for multiparticle manipulation. *Rev. Sci. Instrum.*, 71:2196, 2000.

[65] K. Visscher, S. P. Gross, and S. M. Block. Construction of multiple-beam optical traps with nanometer-resolution position sensing. *IEEE J. Sel. Top. Quant. 2*, page 1066, 1996.

[66] D. L. J. Vossen, A. van der Horst, M. Dogterom, and A. van Blaaderen. Optical tweezers and confocal microscopy for simultaneous three-dimensional manipulation and imaging in concentrated colloidal dispersions. *Rev. Sci. Instrum.*, 75(9):2960–2970, 2004.

[67] J.-M. Fournier, M. M. Burns, and J. A. Golovchenko. Writing diffractive structures by optical trapping. *Proc. SPIE*, 2406:101, 1995.

[68] E. R. Dufresne and D. G. Grier. Optical tweezer arrays and optical substrates created with diffractive optics. *Rev. Sci. Instrum.*, 69(5):1974–1977, 1998.

[69] E. Martin-Badosa, M. Montes-Usategui, A. Carnicer, J. Andilla, E. Pleguezuelos, and I. Juvells. Design strategies for optimizing holographic optical tweezers set-ups. *J. Opt. A-Pure Appl. Opt.*, 9(8):S267–S277, 2007.

[70] M. Dienerowitz, G. Gibson, R. Bowman, and M. Padgett. Holographic tweezers: a platform for plasmonics. *Proc. SPIE*, 8097:80971R, 2011.

[71] C. M. Creely, G. Volpe, G. P. Singh, M. Soler, and D. V. Petrov. Raman imaging of floating cells. *Optics Express*, 13(16):6105–6110, 2005.

[72] T. Haraszti, A. E. M. Clemen, and J. P. Spatz. Biomimetic F-actin cortex models. *Chem. Phys. Chem.*, 10(16):2777–2786, 2009.

[73] K. Dholakia and P. Reece. Optical micromanipulation takes hold. *Nano Today*, 1(1):18–27, 2006.

[74] J. C. Crocker and D. G. Grier. Methods of digital video microscopy for colloidal studies. *J. Colloid Interface Sci.*, 179(1):298–310, 1996.

[75] C. Herring. *The physics of powder metallurgy.* McGraw-Hill Book Co., New York, 1951.

[76] J. P. Hirth and J. Lothe. *Theory of dislocations.* Wiley, New York, 2nd edition, 1982.

[77] J. M. Howe. *Interfaces in Materials.* Wiley, New York, 1997.

[78] S. Graser, P. J. Hirschfeld, T. Kopp, R. Gutser, B. M. Andersen, and J. Mannhart. How grain boundaries limit supercurrents in high-temperature superconductors. *Nat. Phys.*, 6(8):609–614, 2010.

[79] A. Hashibon, P. Schravendijk, C. Elsässer, and P. Gumbsch. Atomistic study of structure and stability of thin Ni films on Fe surfaces. *Philos. Mag.*, 89(34-36):3413–3433, 2009.

[80] P. Y. Huang, C. S. Ruiz-Vargas, A. M. van der Zande, W. S. Whitney, M. P. Levendorf, J. W. Kevek, S. Garg, J. S. Alden, C. J. Hustedt, Y. Zhu, J. Park, P. L. McEuen, and D. A. Muller. Grains and grain boundaries in single-layer graphene atomic patchwork quilts. *Nature*, 469(7330):389–392, 2011.

[81] S. Yip. Nanocrystals: The strongest size. *Nature*, 391:532 – 533, 1998.

[82] H. Van Swygenhoven. Grain boundaries and dislocations. *Science*, 296:66 – 67, 2002.

[83] T. Zykova-Timan, R. E. Rozas, J. Horbach, and K. Binder. Computer simulation studies of finite-size broadening of solid-liquid interfaces: From hard spheres to nickel. *J. Phys.-Condes. Matter*, 21(46), 2009.

[84] Y. Huang and F. J. Humphreys. Measurements of grain boundary mobility during recrystallization of a single-phase aluminium alloy. *Acta Mater.*, 47(7):2259–2268, 1999.

[85] D. L. Medlin, S. M. Foiles, and D. Cohen. A dislocation-based description of grain boundary dissociation: Application to a 90° ¡110¿ tilt boundary in gold. *Acta Mater.*, 49(18):3689–3697, 2001.

[86] S.B. Lee. Correlation between grain boundary faceting-defaceting transition and change of grain boundary properties with temperature. *Mater. Lett.*, 57:3779–3783, 2003.

[87] K. L. Merkle, L. J. Thompson, and F. Phillipp. In-situ HREM studies of grain boundary migration. *Interface Sci.*, 12:277–292, 2004.

[88] M. I. Mendelev and D. J. Srolovitz. Impurity effects on grain boundary migration. *Modell. Simul. Mater. Sci. Eng.*, 10:R79–R109, 2002.

[89] J. J. Hoyt, M. Asta, and A. Karma. Atomistic and continuum modeling of dendritic solidification. *Mater. Sci. Eng. R*, 41(6):121–163, 2003.

[90] Z.T. Trautt and M. Upmanyu. Direct two-dimensional calculations of grain boundary stiffness. *Scr. Mater.*, 52:11751179, 2005.

[91] S. M. Foiles and J.J. Hoyt. Computation of grain boundary stiffness and mobility from boundary fluctuations. *Acta Mater.*, 54(12):3351–3357, 2006.

[92] K. G. F. Janssens, D. Olmstead, E. A. Holm, S. M. Foiles, S. J. Plimpton, and P. M. Derlet. Computing the mobility of grain boundaries. *Nat. Mater.*, 5:124–127, 2006.

[93] D. L. Olmsted, S. M. Foiles, and E. A. Holm. Grain boundary interface roughening transition and its effect on grain boundary mobility for non-faceting boundaries. *Scripta Mater.*, 57(12):1161–1164, 2007.

[94] D. L. Olmsted, E. A. Holm, and S. M. Foiles. Survey of computed grain boundary properties in face-centered cubic metals-II: Grain boundary mobility. *Acta Mater.*, 57(13):3704–3713, 2009.

[95] J. Hernández-Guzmán and E. R. Weeks. The equilibrium intrinsic crystal-liquid interface of colloids. *Proc. Natl. Acad. Sci. USA*, 106(36):15198–15202, 2009.

[96] A. R. Bausch, M. J. Bowick, A. Cacciuto, A. D. Dinsmore, M. F. Hsu, D. R. Nelson, M. G. Nikolaides, A. Travesset, and D. A. Weitz. Grain boundary scars and spherical crystallography. *Science*, 299:1716–1718, 2003.

[97] P. Lipowsky, M. J. Bowick, J. H. Meinke, D. R. Nelson, and A. R. Bausch. Direct visualization of dislocation dynamics in grain-boundary scars. *Nat. Mater.*, 4:407–411, 2005.

[98] A. M. Alsayed, M. F. Islam, J. Zhang, P. J. Collings, and A. G. Yodh. Premelting at defects within bulk colloidal crystals. *Science*, 309:1207–1210, 2005.

[99] V. W. A. de Villeneuve, L. Derendorp, D. Verboekend, E. C. M. Vermolen, W. K. Kegel, H. N. W. Lekkerkerker, and R. P. A. Dullens. Grain boundary pinning in doped hard sphere crystals. *Soft Matter*, 5:2448–2452, 2009.

[100] Z. T. Trautt, M. Upmanyu, and A. Karma. Interface mobility from interface random walk. *Science*, 314:632–635, 2006.

[101] A. P. Young. Melting and the vector coulomb gas in 2 dimensions. *Phys. Rev. B*, 19:1855–1866, 1979.

[102] D. R. Nelson and B. I. Halperin. Dislocation-mediated melting in 2 dimensions. *Phys. Rev. B*, 19:2457–2484, 1979.

[103] J. M. Kosterlitz and D. J Thouless. Ordering, metastability and phase-transitions in 2 dimensional systems. *J. Phys. C*, 6:1181–1203, 1973.

[104] E. O. Hall. The deformation and ageing of mild steel 3. Discussion of results. *Proc. Phys. Soc. B*, 64(381):747–753, 1951.

[105] N. J. Petch. The cleavage strength of polycrystals. *J. Iron Steel Inst.*, 174:25–28, 1953.

[106] N. Hansen. HallPetch relation and boundary strengthening. *Scripta Mater.*, 51(8):801–806, 2004.

[107] H. Suzuki. On the grain boundary migration induced by temperature gradient. *J. Phys. Soc. Jpn.*, 6(6):522–523, 1951.

[108] M. Winning, G. Gottstein, and L. S. Shvindlerman. Stress induced grain boundary motion. *Acta Mater.*, 49(2):211–219, 2001.

[109] L. A. B. Mora. *2D and 3D Grain Growth Modelling and Simulation.* Cuvillier Verlag, Göttingen, 2008.

[110] H. Zhang, D. J. Srolovitz, J. F. Douglas, and J. A. Warren. Characterization of atomic motion governing grain boundary migration. *Phys. Rev. B*, 74(11):115404, 2006.

[111] H. Zhang, D. J. Srolovitz, J. F. Douglas, and J. A. Warren. Atomic motion during the migration of general [001] tilt grain boundaries in Ni. *Acta Mater.*, 55(13):4527–4533, 2007.

[112] I. Toda-Caraballo, P. D. Bristowe, and C. Capdevila. A molecular dynamics study of grain boundary free energies, migration mechanisms and mobilities in a BCC Fe20Cr alloy. *Acta Mater.*, 60(3):1116–1128, 2012.

[113] M. Upmanyu, R. W. Smith, and D. J. Srolovitz. Atomistic simulation of curvature driven grain boundary migration. *Interface Sci.*, 6(1):41–58, 1998.

[114] G. Gottstein, U Czubayko, D. A. Molodov, L. S. Shvindlerman, and W. Wunderlich. In-situ observations of grain boundary migration. *Mater. Sci. Forum*, 204-206:99, 1996.

[115] M. Upmanyu, D. J. Srolovitz, L. S. Shvindlerman, and G. Gottstein. Misorientation dependence of intrinsic grain boundary mobility: Simulation and experiment. *Acta Mater.*, 47(14):3901–3914, 1999.

[116] K. K. Mon, S. Wansleben, D. P. Landau, and K. Binder. Anisotropic surface tension, step free energy, and interfacial roughening in the three-dimensional Ising model. *Phys. Rev. Lett.*, 60(8):708–711, 1988.

[117] C. L. Di Prinzio, B. J. G. Kriegel, and O. B. Nasello. Anisotropic migration of 2-dimensional grain-boundaries. *Acta Metall. Mater.*, 43(6):2269–2273, 1995.

[118] U. Wolf, F. Ernst, T. Muschik, M. W. Finnis, and H. F. Fischmeister. The influence of grain-boundary inclination on the structure and energy of Sigma=3 grain-boundaries in copper. *Phil. Mag. A*, 66(6):991–1016, 1992.

[119] A. P. Sutton and R. W. Balluffi. Overview 61. on geometric criteria for low interfacial energy. *Acta Metallurgica*, 35(9):2177–2201, 1987.

[120] A. E. Lobkovsky, A. Karma, M. I. Mendelev, M. Haataja, and D. J. Srolovitz. Grain shape, grain boundary mobility and the Herring relation. *Acta Mater.*, 52:285–292, 2004.

[121] N. Eustathopoulos. Energetics of solid/liquid interfaces of metals and alloys. *Intl. Met. Rev.*, 28:189, 1983.

[122] H. Mykura and H. Gleiter. Can gravitational torques be used to study grain boundary energy anisotropy? *Scr. Metall. Mater.*, 13(2):137–140, 1979.

[123] M. Upmanyu. Grain boundary stiffness based on a dislocation model. *Scripta Mater.*, 56(6):553–556, 2007.

[124] G. Gottstein, D. A. Molodov, and L. S. Shvindlerman. Grain boundary migration in metals: Recent developments. *Interface Sci.*, 6(1):7–22, 1998.

[125] M. Asta, C. Beckermann, A. Karma, W. Kurz, R. Napolitano, M. Plapp, G. Purdy, M. Rappaz, and R. Trivedi. Solidification microstructures and solid-state parallels: Recent developments, future directions. *Acta Mater.*, 57(4):941–971, 2009.

[126] C. Deng and C. A. Schuh. Atomistic simulation of slow grain boundary motion. *Phys. Rev. Lett.*, 106(4):045503, 2011.

[127] L. Mandelstam. *Ann. Phys*, 41:609, 1913.

[128] M. P. A. Fisher, D. S. Fisher, and J. D. Weeks. Agreement of capillary-wave theory with exact results for the interface profile of the two-dimensional Ising model. *Phys. Rev. Lett.*, 48(5):368–368, 1982.

[129] D. Bedeaux and J. D. Weeks. Correlation functions in the capillary wave model of the liquid-vapor interface. *J. Chem. Phys.*, 82(2):972, 1985.

[130] K. Binder, M. Muller, F. Schmid, and A. Werner. Simulation of interfaces between coexisting phases in materials. *J. Comput.-Aided Mater. Des.*, 4:137, 1997.

[131] A. Werner, F. Schmid, M. Muller, and K. Binder. Anomalous size-dependence of interfacial profiles between coexisting phases of polymer mixtures in thin-film geometry: A Monte Carlo simulation. *J. Chem. Phys.*, 107(19):8175–8188, 1997.

[132] K. L. Merkle. High-resolution electron microscopy of grain boundaries. *Interface Sci.*, 2:311, 1995.

[133] M. Furtkamp, P. Lejcek, and S. Tsurekawa. Grain boundary migration in Fe-3wt%Si alloys. *Interface Sci.*, 6(1-2):59–66, 1998.

[134] T. O. E. Skinner, D. G. A. L. Aarts, and R. P. A. Dullens. Grain-boundary fluctuations in two-dimensional colloidal crystals. *Phys. Rev. Lett.*, 105(16):168301, 2010.

[135] W. T. Read and W. Shockley. Dislocation models of crystal grain boundaries. *Phys. Rev.*, 78(3):275–289, 1950.

[136] E. Zaccarelli, C. Valeriani, E. Sanz, W. C. K. Poon, M. E. Cates, and P. N. Pusey. Crystallization of hard-sphere glasses. *Phys. Rev. Lett.*, 103(13):135704, 2009.

[137] P. Keblinski, S. R. Phillpot, D. Wolf, and H. Gleiter. Thermodynamic criterion for the stability of amorphous intergranular films in covalent materials. *Phys. Rev. Lett.*, 77(14):2965, 1996.

[138] D. Wolf. High-temperature structure and properties of grain boundaries: Long-range vs. short-range structural effects. *Curr. Opin. Solid State Mater. Sci.*, 5(5):435–443, 2001.

[139] H. Zhang and D. J. Srolovitz. Simulation and analysis of the migration mechanism of Sigma 5 tilt grain boundaries in an FCC metal. *Acta Mater.*, 54(3):623–633, 2006.

[140] C. Donati, J. F. Douglas, W. Kob, S. J. Plimpton, P. H. Poole, and S. C. Glotzer. Stringlike cooperative motion in a supercooled liquid. *Phys. Rev. Lett.*, 80(11):2338–2341, 1998.

[141] E. R. Weeks, J. C. Crocker, A. C. Levitt, A. Schofield, and D. A. Weitz. Three-dimensional direct imaging of structural relaxation near the colloidal glass transition. *Science*, 287(5453):627–631, 2000.

[142] P. G. Debenedetti and F. H. Stillinger. Supercooled liquids and the glass transition. *Nature*, 410(6825):259–267, 2001.

[143] W. K. Kegel and A. van Blaaderen. Direct observation of dynamical heterogeneities in colloidal hard-sphere suspensions. *Science*, 287(5451):290–293, 2000.

[144] M. M. Hurley and P. Harrowell. Kinetic structure of a 2-dimensional liquid. *Phys. Rev. E*, 52(2):1694–1698, 1995.

[145] T. O. E. Skinner, D. G. A. L. Aarts, and R. P. A. Dullens. Supercooled dynamics of grain boundary particles in two-dimensional colloidal crystals. *J. Chem. Phys.*, 135(12):124711, 2011.

[146] K. H. Nagamanasa, S. Gokhale, R. Ganapathy, and A. K. Sood. Confined glassy dynamics at grain boundaries in colloidal crystals. *Proc. Natl. Acad. Sci. U. S. A.*, 108(28):11323–11326, 2011.

[147] J. Q. Broughton and G. H. Gilmer. Grain-boundary shearing as a test for interface melting. *Model. Simul. Mater. Sci. Eng.*, 6(1):87–97, 1998.

[148] E. A. Holm and S. M. Foiles. How grain growth stops: A mechanism for grain-growth stagnation in pure materials. *Science*, 328(5982):1138–1141, 2010.

[149] G. Gottstein and L. S. Shvindlerman. *Grain Boundary Migration in Metals*. CRC, Boca Raton, FL, USA, 2nd edition, 2010.

[150] B. Schroder. Thin-film technology based on hydrogenated amorphous-silicon. *Mater. Sci. Eng. A-Struct. Mater. Prop. Microstruct. Process.*, 139:319–333, 1991.

[151] M. M. Trexler and N. N. Thadhani. Mechanical properties of bulk metallic glasses. *Prog. Mater. Sci.*, 55(8):759–839, 2010.

[152] M. D. Ediger. Spatially heterogeneous dynamics in supercooled liquids. *Annu. Rev. Phys. Chem.*, 51:99–128, 2000.

[153] C. A. Angell, K. L. Ngai, G. B. McKenna, P. F. McMillan, and S. W. Martin. Relaxation in glassforming liquids and amorphous solids. *J. Appl. Phys.*, 88(6):3113–3157, 2000.

[154] R. Richert. Dynamics of nanoconfined supercooled liquids. *Annu. Rev. Phys. Chem.*, 62:65–84, 2011.

[155] R. A. Riggleman, K. Yoshimoto, J. F. Douglas, and J. J. de Pablo. Influence of confinement on the fragility of antiplasticized and pure polymer films. *Phys. Rev. Lett.*, 97(4):045502, 2006.

[156] S. Karmakar, C. Dasguptaa, and S. Sastry. Growing length and time scales in glass-forming liquids. *Proc. Natl. Acad. Sci. USA*, 106(10):3675–3679, 2009.

[157] C. R. Berardi, K. Barros, J. F. Douglas, and W. Losert. Direct observation of stringlike collective motion in a two-dimensional driven granular fluid. *Phys. Rev. E*, 81(4):041301, 2010.

[158] F. Hargreaves and R. J. Hills. *J. Inst. Met.*, 41:257, 1929.

[159] C. J. Tweed, B. Ralph, and N. Hansen. The pinning by particles of low and high angle grain boundaries during grain growth. *Acta Metall.*, 32(9):1407–1414, 1984.

[160] M. Winning and A. D. Rollett. Transition between low and high angle grain boundaries. *Acta Mater.*, 53(10):2901–2907, 2005.

[161] G. S. Rohrer. Grain boundary energy anisotropy: A review. *J. Mater. Sci.*, 46(18):5881–5895, 2011.

[162] D. Wolf. A Read-Shockley model for high-angle grain-boundaries. *Scr. Metall.*, 23(10):1713–1718, 1989.

[163] A. P. Sutton and V. Vitek. On the structure of tilt grain-boundaries in cubic metals .1. Symmetrical tilt boundaries. *Philos. Trans. R. Soc. Lond. Ser. A-Math. Phys. Eng. Sci.*, 309(1506):1–68, 1983.

[164] D. Schwartz, V. Vitek, and A. P. Sutton. Atomic structure of (001) twist boundaries in f.c.c. metals - Structural unit model. *Philos. Mag. A-Phys. Condens. Matter Struct. Defect Mech. Prop.*, 51(4):499–520, 1985.

[165] W. Krakow. Atomic-structure of a $\sigma = 21$ grain-boundary. *J. Mater. Res.*, 5(11):2658–2662, 1990.

[166] V. Pontikis. Grain boundary structure and phase transformations : A critical review of computer simulation studies and comparison with experiments. *J Physique Colloques*, 49(C5):C5–327–C5–336, 1988.

[167] P. Keblinski, D. Wolf, S. R. Phillpot, and H. Gleiter. Self-diffusion in high-angle fcc metal grain boundaries by molecular dynamics simulation. *Philos. Mag. A-Phys. Condens. Matter Struct. Defect Mech. Prop.*, 79(11):2735–2761, 1999.

[168] B. Schonfelder, G. Gottstein, and L. S. Shvindlerman. Comparative study of grain-boundary migration and grain-boundary self-diffusion of 001 twist-grain boundaries in copper by atomistic simulations. *Acta Mater.*, 53(6):1597–1609, 2005.

[169] J. P. Hansen and I. R. McDonald. *Theory of simple liquids*. Academic Press, London, 3rd edition, 2006.

[170] M. F. Ashby. Boundary defects, and atomistic aspects of boundary sliding and diffusional creep. *Surf. Sci.*, 31:498–542, 1972.

[171] R. Simon, T. Palberg, and P. Leiderer. Structurally determined Brownian dynamics in ordered colloidal suspensions: Self-diffusion in fluid, supercooled, and crystalline phases. *J. Chem. Phys.*, 99(4):3030–3036, 1993.

[172] P. N. Pusey, E. Zaccarelli, C. Valeriani, E. Sanz, W. C. K. Poon, and M. E. Cates. Hard spheres: Crystallization and glass formation. *Phil.Transactions A*, 367(1909):4993–5011, 2009.

[173] L. S. Shvindlerman, G. Gottstein, V. A. Ivanov, D. A. Molodov, D. Kolesnikov, and W. Lojkowski. Grain boundary excess free volume - direct thermodynamic measurement. *J. Mater. Sci.*, 41(23):7725–7729, 2006.

[174] N. Giovambattista, S. V. Buldyrev, F. W. Starr, and H. E. Stanley. Connection between Adam-Gibbs theory and spatially heterogeneous dynamics. *Phys. Rev. Lett.*, 90(8):085506, 2003.

[175] W. Götze and L. Sjögren. Comments on the mode coupling theory for structural relaxation. *Chem. Phys.*, 212(1):47–59, 1996.

[176] Y. Gebremichael, T. B. Schroder, F. W. Starr, and S. C. Glotzer. Spatially correlated dynamics in a simulated glass-forming polymer melt: Analysis of clustering phenomena. *Phys. Rev. E*, 64(5 Pt 1):051503, 2001.

[177] V. Teboul, A. Monteil, L. C. Fai, A. Kerrache, and S. Maabou. An investigation of string-like cooperative motion in a strong network glass-former. *Eur. Phys. J. B*, 40:49, 2004.

[178] Q. H. Wei, C. Bechinger, and P. Leiderer. Single-file diffusion of colloids in one-dimensional channels. *Science*, 287:625, 2000.

[179] C. R. Nugent, K. V. Edmond, H. N. Patel, and E. R. Weeks. Colloidal glass transition observed in confinement. *Phys. Rev. Lett.*, 99:025702, 2007.

[180] A. L. Boskey. Biomineralization: Conflicts, challenges, and opportunities. *J. Cell. Biochem.*, 30-31:83–91, 1998.

[181] F. Bresme and L. G. Cámara. Computer simulation studies of crystallization under confinement conditions. *Chem. Geo.*, 230(34):197–206, 2006.

[182] J. Schmitt, G. Decher, W. J. Dressick, S. L. Brandow, R. E. Geer, R. Shashidhar, and J. M. Calvert. Metal nanoparticle/polymer superlattice films: Fabrication and control of layer structure. *Adv. Mater.*, 9(1):61–65, 1997.

[183] M. S. Arayne, N. Sultana, and S. Noor Us. Fabrication of solid nanoparticles for drug delivery. *Pak. J. Pharm. Sci.*, 20(3):251–259, 2007.

[184] S. T. Cui, P. T. Cummings, and H. D. Cochran. Molecular dynamics simulation of the rheological and dynamical properties of a model alkane fluid under confinement. *J. Chem. Phys.*, 111(3):1273–1280, 1999.

[185] Y. X. Zhu and S. Granick. Superlubricity: A paradox about confined fluids resolved. *Phys. Rev. Lett.*, 93(9):096101, 2004.

[186] S. Yamada. Nanotribology of symmetric and asymmetric liquid lubricants. *Symmetry*, 2(1):320–345, 2010.

[187] P. S. Dittrich and A. Manz. Lab-on-a-chip: microfluidics in drug discovery. *Nat. Rev. Drug Discov.*, 5(3):210–218, 2006.

[188] K. M. Unruh, T. E. Huber, and C. A. Huber. Melting and freezing behavior of indium metal in porous glasses. *Phys. Rev. B*, 48(12):9021–9027, 1993.

[189] M. Sliwinska-Bartkowiak, J. Gras, R. Sikorski, R. Radhakrishnan, L. Gelb, and K. E. Gubbins. Phase transitions in pores: Experimental and simulation studies of melting and freezing. *Langmuir*, 15(18):6060–6069, 1999.

[190] D. D. Awschalom and J. Warnock. Supercooled liquids and solids in porous-glass. *Phys. Rev. B*, 35(13):6779–6785, 1987.

[191] S. Granick. Motions and relaxations of confined liquids. *Science*, 253(5026):1374–1379, 1991.

[192] M. Heuberger, M. Zäch, and N. D. Spencer. Density fluctuations under confinement: When is a fluid not a fluid? *Science*, 292(5518):905–908, 2001.

[193] R. Haghgooie and P. S. Doyle. Structure and dynamics of repulsive magnetorheological colloids in two-dimensional channels. *Phys. Rev. E*, 72(1):011405, 2005.

[194] C. Alba-Simionesco, B. Coasne, G. Dosseh, G. Dudziak, K. E. Gubbins, R. Radhakrishnan, and M. Sliwinska-Bartkowiak. Effects of confinement on freezing and melting. *J. Phys.-Condes. Matter*, 18(6):R15–R68, 2006.

[195] A. M. Homola, H. V. Nguyen, and G. Hadziioannou. Influence of monomer architecture on the shear properties of molecularly thin polymer melts. *J. Chem. Phys.*, 94(3):2346–2351, 1991.

[196] F. Wang and Y. Zhao. The unique properties of the solid-like confined liquid films: A large scale molecular dynamics simulation approach. *Acta Mech. Solida Sinica*, 24(2):101–116, 2011.

[197] R. Bubeck, C. Bechinger, S. Neser, and P. Leiderer. Melting and reentrant freezing of two-dimensional colloidal crystals in confined geometry. *Phys. Rev. Lett.*, 82(16):3364–3367, 1999.

[198] S. M. Ilett, A. Orrock, W. C. K. Poon, and P. N. Pusey. Phase-behavior of a model colloid-polymer mixture. *Phys. Rev. E*, 51(2):1344–1352, 1995.

[199] A. Yethiraj and A. van Blaaderen. A colloidal model system with an interaction tunable from hard sphere to soft and dipolar. *Nature*, 421(6922):513–517, 2003.

[200] K. Binder, S. Sengupta, and P. Nielaba. The liquid-solid transition of hard discs: first-order transition or Kosterlitz-Thouless-Halperin-Nelson-Young scenario? *J. Phys. Cond. Matt.*, 14(9):2323–2333, 2002.

[201] N. Gribova, A. Arnold, T. Schilling, and C. Holm. How close to two dimensions does a Lennard-Jones system need to be to produce a hexatic phase? *J. Chem. Phys.*, 135(5):054514, 2011.

[202] E. P. Bernard and W. Krauth. Two-step melting in two dimensions: first-order liquid-hexatic transition. *Phys. Rev. Lett.*, 107(15):155704, 2011.

[203] E. Azéma, F. Radjaï, R. Peyroux, and G. Saussine. Force transmission in a packing of pentagonal particles. *Phys. Rev. E*, 76(1):011301, 2007.

[204] K. Zahn and G. Maret. Dynamic criteria for melting in two dimensions. *Phys. Rev. Lett.*, 85(17):3656–3659, 2000.

[205] R. Bubeck, S. Neser, C. Bechinger, and P. Leiderer. *Structure and dynamics of two-dimensional colloidal crystals in confined geometry. Trends in Colloid and Interface Science XII*, volume 110, pages 41–45. Springer Berlin / Heidelberg, 1998.

[206] M. Saint Jean, C. Even, and C. Guthmann. Macroscopic 2D Wigner islands. *Europhys.Lett.*, 55(1):45–51, 2001.

[207] K. Mangold, J. Birk, P. Leiderer, and C. Bechinger. Binary colloidal systems in two-dimensional circular cavities: Structure and dynamics. *Phys. Chem. Chem. Phys.*, 6(7):1623–1626, 2004.

[208] I. Hargittai. *Fivefold symmetry.* World Scientific, Singapore, 1992.

[209] T. Bauert, L. Merz, D. Bandera, M. Parschau, J. S. Siegel, and K.-H. Ernst. Building 2D crystals from 5-fold-symmetric molecules. *J. Am. Chem. Soc.*, 131(10):3460–3461, 2009.

[210] R. Penrose. Pentaplexity a class of non-periodic tilings of the plane. *Math. Intelligencer*, 2(1):32–37, 1979.

[211] R. Lück. Dürer-Kepler-Penrose, the development of pentagon tilings. *Mater. Sci. Eng.: A*, 294296:263–267, 2000.

[212] D. Shechtman, I. Blech, D. Gratias, and J. W. Cahn. Metallic phase with long-range orientational order and no translational symmetry. *Phys. Rev. Lett.*, 53(20):1951, 1984.

[213] D. Levine and P. J. Steinhardt. Quasicrystals - a new class of ordered structures. *Phys. Rev. Lett.*, 53(26):2477–2480, 1984.

[214] D. Clery. Once-ridiculed discovery redefined the term crystal. *Science*, 334(6053):165, 2011.

[215] J. Mikhael, M. Schmiedeberg, S. Rausch, J. Roth, H. Stark, and C. Bechinger. Proliferation of anomalous symmetries in colloidal monolayers subjected to quasiperiodic light fields. *Proc. Natl. Acad. Sci. USA*, 107(16):7214–7218, 2010.

[216] V. G. Gryaznov, J. Heydenreich, A. M. Kaprelov, S. A. Nepijko, A. E. Romanov, and J. Urban. Pentagonal symmetry and disclinations in small particles. *Cryst. Res. Technol.*, 34(9):1091–1119, 1999.

[217] D. V. Talapin, E. V. Shevchenko, M. I. Bodnarchuk, X. Ye, J. Chen, and C. B. Murray. Quasicrystalline order in self-assembled binary nanoparticle superlattices. *Nature*, 461(7266):964–967, 2009.

[218] H. Chen, Y. Gao, H. Yu, H. Zhang, L. Liu, Y. Shi, H. Tian, S. Xie, and J. Li. Structural properties of silver nanorods with fivefold symmetry. *Micron*, 35(6):469–474, 2004.

[219] Y. Gao, L. Song, P. Jiang, L. F. Liu, X. Q. Yan, Z. P. Zhou, D. F. Liu, J. X. Wang, H. J. Yuan, Z. X. Zhang, X. W. Zhao, X. Y. Dou, W. Y. Zhou, G. Wang, S. S. Xie, H. Y. Chen, and J. Q. Li. Silver nanowires with five-fold symmetric cross-section. *J. Cryst. Growth*, 276(34):606–612, 2005.

[220] Y. N. Xia, Y. J. Xiong, B. Lim, and S. E. Skrabalak. Shape-controlled synthesis of metal nanocrystals: Simple chemistry meets complex physics? *Angew. Chem.-Int. Edit.*, 48(1):60–103, 2009.

[221] M. D. Ball and D. J. Lloyd. Particles apparently exhibiting five-fold symmetry in Al-Li-Cu-Mg alloys. *Scr. Metall.*, 19(9):1065–1068, 1985.

[222] A. V. Anikeenko, N. N. Medvedev, A. Bezrukov, and D. Stoyan. Observation of fivefold symmetry structures in computer models of dense packing of hard spheres. *J. Non-Cryst. Solids*, 353(32-40):3545–3549, 2007.

[223] J. Carrasco, A. Michaelides, M. Forster, S. Haq, R. Raval, and A. Hodgson. A one-dimensional ice structure built from pentagons. *Nat. Mater.*, 8(5):427–431, 2009.

[224] N. C. Karayiannis, R. Malshe, J. J. de Pablo, and M. Laso. Fivefold symmetry as an inhibitor to hard-sphere crystallization. *Phys. Rev. E*, 83(6):061505, 2011.

[225] D. T. Lee and B. J. Schachter. Two algorithms for constructing a Delaunay triangulation. *Int. J. Comput. Inf. Sci.*, 9(3):219–242, 1980.

[226] R. P. A. Dullens, D. G. A. L. Aarts, and W. K. Kegel. Colloidal crystal-fluid interfaces. *Philos. Mag. Lett.*, 87(11):893–898, 2007.

[227] F. A. Lindemann. *Phys. Z.*, 11:609, 1910.

[228] X. H. Zheng and J. C. Earnshaw. On the Lindemann criterion in 2D. *Europhys. Lett.*, 41(6):635–640, 1998.

[229] V. M. Bedanov, G. V. Gadiyak, and Y. E. Lozovik. On a modified Lindemann-like criterion for 2D melting. *Phys. Lett. A*, 109(6):289–291, 1985.

[230] D. R. Nelson. *Defects and geometry in condensed matter physics*. Cambridge University Press, 2002.

[231] D. Frenkel and B Smit. *Understanding Molecular Simulation. From Algorithms to Applications,*. Academic Press, London, 2nd ed. edition, 2002.

[232] A. Vikarchuk, M. Dorogov, A. Volkov, and N. Gryzunova. Disclination defects in substrates as the sites of whisker growth. *Russian Metallurgy (Metally)*, 2011(4):290–295, 2011.

[233] W. L. Miller and A. Cacciuto. Two-dimensional packing of soft particles and the soft generalized Thomson problem. *Soft Matter*, 7(16):7552–7559, 2011.

[234] J. P. Hoogenboom, A. Yethiraj, A. K. van Langen-Suurling, J. Romijn, and A. van Blaaderen. Epitaxial crystal growth of charged colloids. *Phys. Rev. Lett.*, 89(25):256104, 2002.

[235] C. T. Kresge, M. E. Leonowicz, W. J. Roth, J. C. Vartuli, and J. S. Beck. Ordered mesoporous molecular-sieves synthesized by a liquid-crystal template mechanism. *Nature*, 359(6397):710–712, 1992.

[236] A. A. Lucas, I. Derycke, Ph Lambin, J. P. Vigneron, L. Leherte, M. Elanany, J. M. Andr, A. V. Larin, and D. P. Vercauteren. Confinement in molecular sieves: The pioneering physical concepts. *J. Mol. Catal. A: Chem.*, 305(12):16–23, 2009.

[237] N. Matsuoka and J. Murton. Frost weathering: Recent advances and future directions. *Permafrost Periglacial Process.*, 19(2):195–210, 2008.

[238] C. Toninelli, G. Biroli, and D. S. Fisher. Jamming percolation and glass transitions in lattice models. *Phys. Rev. Lett.*, 96(3):035702, 2006.

[239] A. J. Liu and S. R. Nagel. The jamming transition and the marginally jammed solid. *Annu. Rev. Condens. Matter Phys.*, 1:347–369, 2010.

[240] G. B. McKenna. Confit iii. Summary and perspectives on dynamics in confinement. *Eur. Phys. J.-Spec. Top.*, 141:291–301, 2007.

[241] M. Alcoutlabi and G. B. McKenna. Effects of confinement on material behaviour at the nanometre size scale. *J. Phys.-Condes. Matter*, 17(15):R461–R524, 2005.

[242] M. C. Bellissent-funel, J. Lal, and L. Bosio. Structural study of water confined in porous-glass by neutron-scattering. *J. Chem. Phys.*, 98(5):4246–4252, 1993.

[243] J. R. Dorfman and H. van Beijeren. Dynamical systems theory and transport coefficients: A survey with applications to Lorentz gases. *Physica A*, 240(12):12–42, 1997.

[244] V. Krakoviack. Mode-coupling theory predictions for the dynamical transitions of partly pinned fluid systems. *Phys. Rev. E*, 84(5):050501, 2011.

[245] J. Kurzidim, D. Coslovich, and G. Kahl. Impact of random obstacles on the dynamics of a dense colloidal fluid. *Phys. Rev. E*, 82(4):041505, 2010.

[246] J. Kurzidim, D. Coslovich, and G. Kahl. Dynamic arrest of colloids in porous environments: disentangling crowding and confinement. *J. Phys.-Condes. Matter*, 23(23):234122, 2011.

[247] K. Kim, K. Miyazaki, and S. Saito. Slow dynamics in random media: Crossover from glass to localization transition. *Europhys. Lett.*, 88(3):36002, 2009.

[248] F. He, L. M. Wang, and R. Richert. Dynamics of supercooled liquids in the vicinity of soft and hard interfaces. *Phys. Rev. B*, 71:144205, 2005.

[249] C. L. Jackson and G. B. McKenna. The glass-transition of organic liquids confined to small pores. *J. Non-Cryst. Solids*, 131:221–224, 1991.

[250] D. Sappelt and J. Jackle. The cooperativity length in models for the glass-transition. *J. Phys. A-Math. Gen.*, 26(24):7325–7341, 1993.

[251] G. Barut, P. Pissis, R. Pelster, and G. Nimtz. Glass transition in liquids: Two versus three-dimensional confinement. *Phys. Rev. Lett.*, 80(16):3543–3546, 1998.

[252] G. Biroli, J. P. Bouchaud, A. Cavagna, T. S. Grigera, and P. Verrocchio. Thermodynamic signature of growing amorphous order in glass-forming liquids. *Nat. Phys.*, 4(10):771–775, 2008.

[253] P. Pissis, A. Kyritsis, G. Barut, R. Pelster, and G. Nimtz. Glass transition in 2- and 3-dimensionally confined liquids. *J. Non-Cryst. Solids*, 235:444–449, 1998.

[254] L. D. Gelb and K. E. Gubbins. Pore size distributions in porous glasses: A computer simulation study. *Langmuir*, 15(2):305–308, 1999.

[255] G. B. McKenna. Size and confinement effects in glass forming liquids: Perspectives on bulk and nano-scale behaviours. *J. Phys. IV*, 10(P7):53–57, 2000.

[256] G. B. McKenna. Status of our understanding of dynamics in confinement: Perspectives from Confit 2003. *Eur. Phys. J. E*, 12(1):191–194, 2003.

[257] F. Höfling, T. Franosch, and E. Frey. Localization transition of the three-dimensional Lorentz model and continuum percolation. *Phys. Rev. Lett.*, 96(16):165901, 2006.

[258] K. Kim, K. Miyazaki, and S. Saito. Molecular dynamics studies of slow dynamics in random media: Type A-B and reentrant transitions. *Eur. Phys. J.-Spec. Top.*, 189(1):135–139, 2010.

[259] W. Götze and L. Sjögren. Relaxation processes in supercooled liquids. *Rep. Prog. Phys.*, 55(3):241–376, 1992.

[260] W. Kob. The mode-coupling theory of the glass transition. *ACS Symp. Ser.*, 676:28, 1997.

[261] A. J. Moreno and J. Colmenero. Anomalous dynamic arrest in a mixture of large and small particles. *Phys. Rev. E*, 74(2):021409, 2006.

[262] H. König, R. Hund, K. Zahn, and G. Maret. Experimental realization of a model glass former in 2D. *J. Eur. Phys. E*, 18(3):287–293, 2005.

[263] R. Brüning, D. A. St-Onge, S. Patterson, and W. Kob. Glass transitions in one-, two-, three-, and four-dimensional binary lennard-jones systems. *J. Phys.-Condes. Matter*, 21(3):035117, 2009.

[264] D. Hajnal, J. M. Brader, and R. Schilling. Effect of mixing and spatial dimension on the glass transition. *Phys. Rev. E*, 80(2):021503, 2009.

[265] N. Osterman, D. Babic, I. Poberaj, J. Dobnikar, and P. Ziherl. Observation of condensed phases of quasiplanar core-softened colloids. *Phys. Rev. Lett.*, 99(24):248301, 2007.

[266] J. A. Barker and D. Henderson. Perturbation theory and equation of state for fluids .2. A successful theory of liquids. *J. Chem. Phys.*, 47(11):4714–4721, 1967.

[267] A. A. Louis and R. Roth. Generalized depletion potentials. *J. Phys. Condens. Matter*, 13(33):L777–L784, 2001.

[268] V. Krakoviack. Tagged-particle dynamics in a fluid adsorbed in a disordered porous solid: Interplay between the diffusion-localization and liquid-glass transitions. *Phys. Rev. E*, 79(6):061501, 2009.

List of publications

To date the following publications based upon work in this thesis have been submitted or are in preparation:

Thomas O. E. Skinner, Dirk G. A. L. Aarts and Roel P. A. Dullens, (2010), *Grain-boundary fluctuations in two-dimensional colloidal crystals*, Phys. Rev. Lett. 105, 168301, Editors Suggestion, http://link.aps.org/doi/10.1103/PhysRevLett.105.168301, (Chapter 3)

Thomas O. E. Skinner, Dirk G. A. L. Aarts and Roel P. A. Dullens, (2011), *Supercooled dynamics of grain-boundary particles in colloidal crystals*, J. Chem. Phys. 135, 124711, http://dx.doi.org/10.1063/1.3640417, (Chapter 4)

Thomas O. E. Skinner, Henry Martin, Dirk G. A. L. Aarts and Roel P. A. Dullens, (2012), *Frustrated crystallisation and melting in two-dimensional pentagonal confinement*, In preparation, (Chapter 5)

Thomas O. E. Skinner, Jürgen Horbach and Roel P. A. Dullens, (2012), *Dynamics of a colloidal fluid confined in a 2D random matrix*, In preparation, (Chapter 6)

Acknowledgments

I would like to thank Roel for all his help, ideas and enthusiasm over the last 3.5 years and to Dirk for his additional input. I would like to thank Liz who showed me the ropes back at the very beginning, to Harry and Oli for making the first 2 years never dull, to Mike and Sam for making the latter two years highly enjoyable, to Alice, Paola and Julia for making the Dullens office good fun and to Tara and my family for their support.